Purdue University
Purdue e-Pubs

Open Access Theses | Theses and Dissertations

January 2016

MODELING THE LUBRICATING INTERFACES OF ULTRA-HIGH PRESSURE RADIAL PISTON MACHINES

Gautham Ramchandran
Purdue University

Follow this and additional works at: https://docs.lib.purdue.edu/open_access_theses

Recommended Citation
Ramchandran, Gautham, "MODELING THE LUBRICATING INTERFACES OF ULTRA-HIGH PRESSURE RADIAL PISTON MACHINES" (2016). *Open Access Theses*. 1133.
https://docs.lib.purdue.edu/open_access_theses/1133

This document has been made available through Purdue e-Pubs, a service of the Purdue University Libraries. Please contact epubs@purdue.edu for additional information.

PURDUE UNIVERSITY
GRADUATE SCHOOL
Thesis/Dissertation Acceptance

This is to certify that the thesis/dissertation prepared

By GAUTHAM RAMCHANDRAN

Entitled

MODELING THE LUBRICATING INTERFACES OF ULTRA-HIGH PRESSURE RADIAL PISTON MACHINES

For the degree of Master of Science in Mechanical Engineering

Is approved by the final examining committee:

ANDREA VACCA
Chair

MONIKA IVANTYSYNOVA

FARSHID SADEGHI

To the best of my knowledge and as understood by the student in the Thesis/Dissertation Agreement, Publication Delay, and Certification Disclaimer (Graduate School Form 32), this thesis/dissertation adheres to the provisions of Purdue University's "Policy of Integrity in Research" and the use of copyright material.

Approved by Major Professor(s): ANDREA VACCA

Approved by: JAY P. GORE 7/20/2016

Head of the Departmental Graduate Program Date

MODELING THE LUBRICATING INTERFACES OF ULTRA-HIGH PRESSURE RADIAL PISTON MACHINES

A Thesis

Submitted to the Faculty

of

Purdue University

by

Gautham Ramchandran

In Partial Fulfillment of the

Requirements for the Degree

of

Master of Science in Mechanical Engineering

August 2016

Purdue University

West Lafayette, Indiana

For my family

ACKNOWLEDGEMENTS

Firstly, I would like to extend my gratitude to Prof. Andrea Vacca for giving me the wonderful opportunity to work in his research group, and for being one of the best possible mentors anyone can hope for. It is only through his constant guidance, enthusiasm and support that I have grown as a researcher. Not only did I have the opportunity to work with radial piston machines, I also gained tremendous exposure to modeling external gear machines and conducting experiments within the short span of a year and a half. I am grateful to Prof. Monika Ivantysynova for her valuable comments and suggestions throughout my time at Maha, and for giving me a wonderful introduction to the modeling of fluid power systems. I thank Prof. Farshid Sadeghi for his guidance and for introducing me to tribology and lubrication modeling through his class at Purdue.

I have been fortunate to have had many mentors at Maha. I thank Pulkit for helping me get familiar with his work and many fruitful discussions that helped me shape this thesis. I am grateful to Tim for his constructive ideas that enabled me to develop my test rig. I would also like to thank Divya for her many thoughtful suggestions, especially related to developing the mixed lubrication model. I thank Matteo for being the character that he is, and for being a supportive guide while I learned the nuances of OpenFOAM.

I would also like to thank my wonderful lab mates – Ram, Sid, Guido, Riccardo, Andrew, Xinran, Addison, Fabio, Rituraj, Srinath, Yash, Jeremy, Meike, Colleen, Mrudula, Hiral, Dan, Lizhi, Paul, Rene, Damiano, and many others who made Maha a fun and wonderful place to learn and grow. I especially thank Susan for being the wonderfully optimistic and helpful person that she is, Anthony for his dedication to all of our projects, and Connie for making life in graduate school just a little bit easier.

I dedicate this thesis to my parents, my little sister Apoorva, and my grandparents, for their love and affection and for supporting me throughout my life.

TABLE OF CONTENTS

Page

Page

LIST OF TABLES

LIST OF FIGURES

Figure Page

Figure Page

Figure Page

Figure Page

Figure Page

Figure Page

Appendix Figure

NOMENCLATURE

Symbol	Description	Units
P_{HP}	pressure in HP channel	bar
P_{LP}	pressure in LP channel	bar
V_{HP}	volume of HP channel	m^3
V_{LP}	volume of LP channel	m^3
ρ	density of hydraulic oil	kg/m^3
η	viscosity of hydraulic oil	Pa.s
h	Lubricating gap height / film thickness between solid surfaces	m
$Q_{rHP,i}$	flow rate from i^{th} displacement chamber to HP channel	m^3/s
$Q_{rHP,i}$	flow rate from LP channel to i^{th} displacement chamber	m^3/s
$Q_{pist,i}$	piston-cylinder leakage flow rate in i^{th} displacement chamber	m^3/s
$A_{DC,i}$	cross-sectional area of i^{th} displacement chamber	m^2
w_{gap}	width of lubricating gap region	m
$e1, e2$	piston eccentricities with respect to cylinder axis	m
l_{gap}	gap length of lubricating film region	m
x_A	Distance of cylinder face from origin	m
h_g	Piston/Cylinder geometrical compliance	m
ϕ	Angle along the cylinder circumference	°
r_p	Piston radius	m
p	Pressure generated in the lubricating gap domain	bar
$\mathbf{V}$	Velocity vector	m/s
β_p	Pressure coefficient for density	Pa-m^3/kg
E	Young's modulus	Pa
μ	Friction coefficient	-
τ	Shear stress	Pa
P_{visc}	Power loss due to viscous friction	W
Q_{leak}	Leakage flow rate	m^3/s
θ	Shaft angle	°

Symbol	Description	Units
u_e	Entrainment velocity of the lubricant	m/s
E'	Effective modulus of elasticity	Pa
R_x	Radius of cylindrical surface in x direction	m
ω_{gs}, ω_{H0}	Under-relaxation parameters	-
τ_L	Limiting shear stress	Pa
b	Half Hertzian width	m
P	Dimensionless pressure	-
H	Dimensionless gap height	-
r_o	Radius of the outer race	m
e	Eccentricity in the rotating shaft	m
R_q	Standard deviation of the composite roughness	m
$\bar{P}_c$	Non-dimensional contact pressure	m
P_c	Contact pressure	Pa
H_Y	Non-dimensional material hardness	-
λ_y^*	Auto-correlation length	m
σ	Yield strength of the material	Pa
ν	Poisson's ratio	-
W_{asp}	Load supported by asperities	N
W_f	Load supported by the fluid	N

Subscripts	Description
t	Top surface
b	Bottom surface
g	Geometrical
0	Ambient
visc	Viscous friction
ref	Reference
cp	Contact point
a	Surface a
b	Surface b
p	Piston

Acronyms	Description
LP	Low pressure
HP	High pressure
FSI	Fluid Structure Interaction
EHL	Elastohydrodynamic Lubrication
EHD	Elastohydrodynamic
BDC	Bottom Dead Center
IDC	Inner Dead Center
ODC	Outer Dead Center
CFD	Computational Fluid Dynamics
IM	Influence Matrix

ABSTRACT

Ramchandran, Gautham. M.S.M.E., Purdue University, August 2016. Modeling the Lubricating Interfaces of Ultra-High Pressure Radial Piston Machines. Major Professor: Andrea Vacca, School of Mechanical Engineering.

A novel approach to modeling the lubricating interfaces of radial piston machines – operating at ultra-high pressures of 700 bar or higher – is presented in this study. The two types of lubricating interfaces present in rotating cam type radial piston machines are the Piston/Cylinder and Cam/Piston interfaces. Together, these two interfaces accounts for the power losses arising from shear stresses and leakages across the gaps. By formulating modeling approaches that accurately portray the physical behavior and characteristics of the two interfaces, a methodology for the virtual designing and prototyping of these machines can be established that allows for the exploration of new design features that can result in reduced power losses and larger lifetimes.

The modeling of the cam/piston interface is complicated by the fact that the reference pump geometry to be modeled has rolling element bearings present around the eccentric shaft and a free-to-rotate outer race resting on these bearings that are in contact with all the pistons. In order to evaluate the friction at the cam/piston interface, an experiment is undertaken to characterize the motion of the outer race in the first stage of this analysis. The instantaneous angular velocity of the outer race as a function of the rotation of the eccentric shaft is found through the use of a camera. Once the kinematics of the outer race is captured, the instantaneous variation of the friction coefficient at the interface is evaluated through a previously developed friction model for the cam/piston contact interface at various operating conditions. This undertaking allows for an accurate prediction of the piston tilt within the lubricating gap as the magnitude and direction of the friction force at the cam/piston interface heavily influences the micro-motion of the

piston. The use of the now accurate friction model also allows for the evaluation of the power losses due to viscous friction at the cam/piston interface.

The second part of this study involves the exploration of circumferential grooved piston designs as a possibility of reducing the losses occurring at the piston/cylinder interface. Grooves located close to the displacement chamber ends (high pressure) of the pistons aid in the better balance and tilt of the pistons within the cylinder. It is observed that the full film assumption in the modeling of the piston/cylinder interface predicts regions of solid-solid contact during certain intervals of the pump cycle. In order to evaluate the effect of the surface roughness features and asperity loading at low gap heights observed in this interface, a Mixed Fluid Structure Interaction – Elastohydrodynamic (FSI-EHD) model is developed. It is seen that the full film assumption underestimates the losses due to leakages present in this gap at extreme operating conditions. The evaluation of the performance parameters to a greater degree of accuracy is now possible through the development of this model. An additional benefit is that it can predict the load supported by the fluid film as well as the asperities, and thus, allows for the evaluation of new designs where regions of mixed lubrication may be avoided.

CHAPTER 1. INTRODUCTION

1.1 Introduction to Radial Piston Machines

Radial piston machines are positive displacement machines that are predominantly used in high pressure hydraulic applications. Among piston pumps, radial piston pumps usually have higher efficiencies due to the fact that they only have two lubricating interfaces. Their design is compact and they can withstand high pressures, even at low shaft speeds. These features make these designs very successful in applications such as motors in hydraulic transmissions, pump units in wind energy, stationary system applications such as hydraulic presses, bolt tensioners and rock splitters, etc. Owing to their great demand in these applications, it is important that these machines highly efficient in their functioning as well as durable in operation.

There are, in general, two types of radial piston machines: the rotating cam type and rotating cylinder type. While the pistons rest on an inner eccentric cam whose rotation describes their motion in a rotating cam type machine, in the rotating cylinder type design, the pistons rest on an outer stationary ring while the cylinder housing in the center rotates. Figure 1 shows the conceptual schematics of both these types of machines.

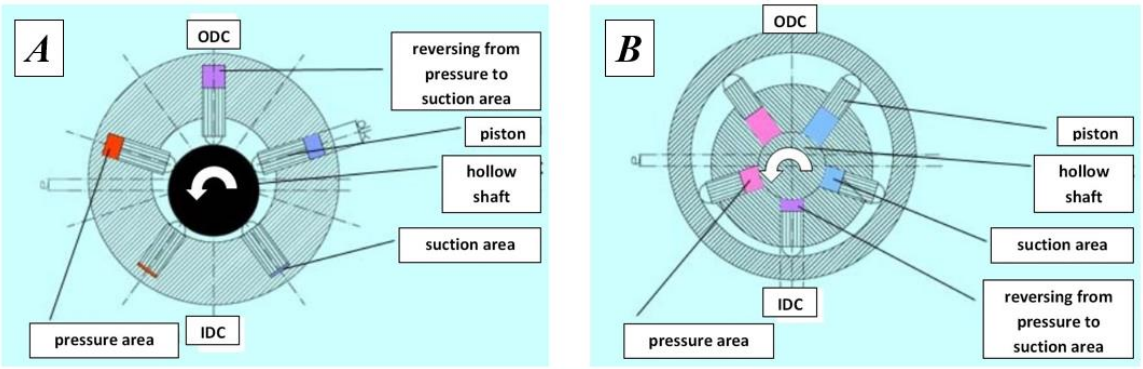

Figure 1: (A) Rotating cam type unit, (B) Rotating cylinder type unit.

1.2 Main Tribological Interfaces

Figure 2 depicts a typical rotating cam type radial piston pump unit which is the focus of this study. There are two main tribological interfaces present in these machines: the piston/cylinder interface (Figure 3) and the cam/piston interface (Figure 4). The primary functions of these lubricating gaps are those of load bearing and sealing. The lubricant film present in these gaps must be able to support the external load so that wear due to metal-metal contact and ultimately, the failure of the unit, are prevented. However, the presence of this load bearing fluid film implies that these machines are subjected to energy losses due to leakages (in the piston/cylinder interface) and viscous friction due to the fluid shearing (in both interfaces).

Designing the piston/cylinder interface to ensure low power losses poses a challenging issue. The two sources of losses – leakage-related losses and viscous friction power losses – are opposing in nature. While the losses due to viscous shearing tend to increase with lower gap heights in the interface, the leakages increase with increasing lubricating film thicknesses between the pistons and cylinders.

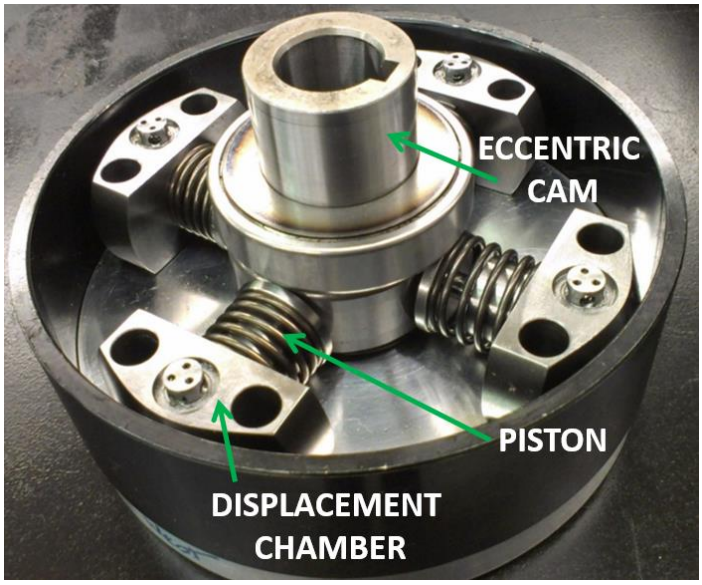

Figure 2: Rotating cam type radial piston pump unit.

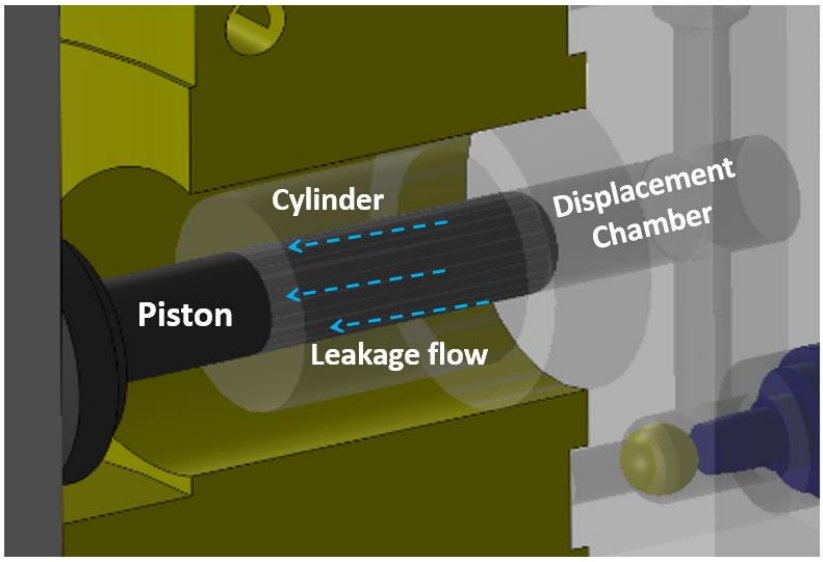

Figure 3: Illustration of the piston/cylinder interface of a radial piston pump unit and the leakage across this interface.

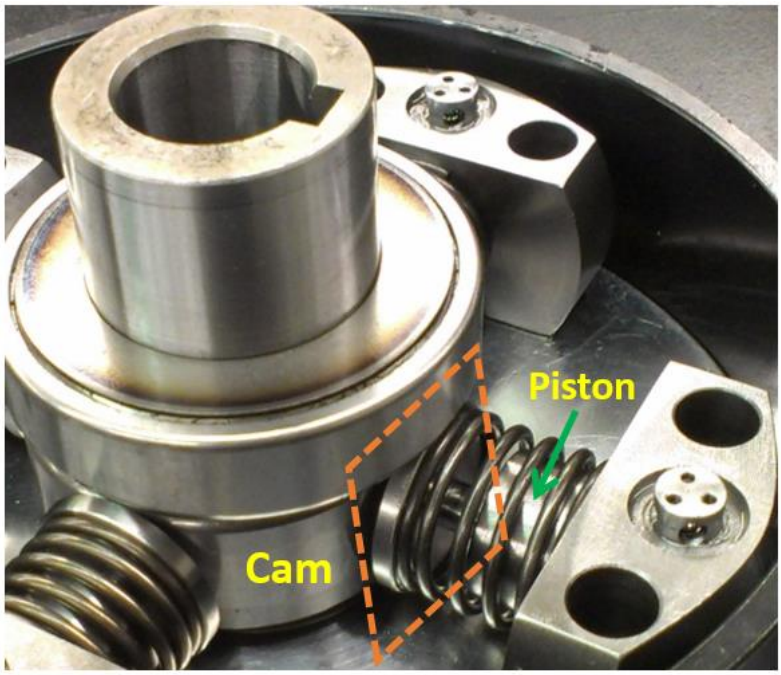

Figure 4: Illustration of the cam/piston contact interface in a typical radial piston pump.

For the cam/piston interface in radial piston machines, the sole factor is ensuring that the gap heights at the cam/piston contact is sufficient to reduce viscous friction losses at the

interface. However, due to large, dynamically varying loads acting at the contact, as well as relatively low operating speeds, this task is easier said than done. Therefore, an in-depth study of these interfaces is warranted in order to develop efficiently functioning units through virtual prototyping, which is one of the goals of the present research.

1.3 Reference Pump Design

While radial piston machines can function as both hydrostatic pumps and motors, a rotating cam type pump configuration will be used for reference in the present work. Figures 2 and 4 represent the interfaces of the reference pump considered in this study. The different components present in the design being studied are highlighted in the top view of the pump shown in Figure 5. The unit considered for this research has a rated operating pressure of 700 bar and a displacement of 1.0 cc/rev.

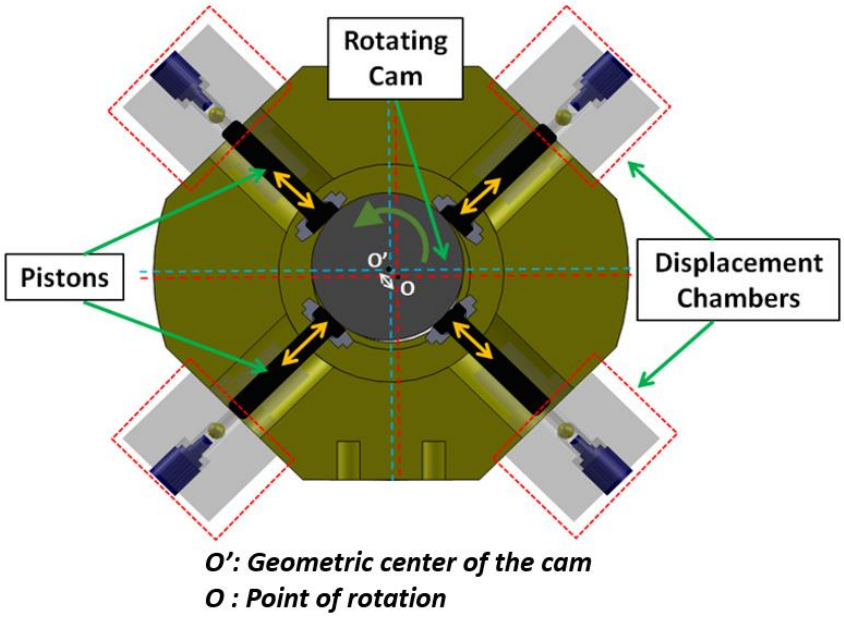

Figure 5: Top view of the reference radial piston pump unit along with the important components.

The principle of operation for this particular unit is straightforward – the low pressure (LP) channel receives fluid from the suction port and sends it to the four displacement chambers present. The LP channel is pressurized – the pump is not a typical open circuit

design that takes fluid from atmospheric pressure, but requires a boost pump (not shown here). Further details of this configuration can be found in [6]. Two sets of inlet and outlet ball check valves control the entry and exit of the fluid within each displacement chamber. The rotation of an eccentric cam results in the reciprocating motion of each of the four pistons within their respective displacement chamber, thus providing the pumping action for this pump. The fluid is sent at high pressure through the high pressure (HP) channel and finally, to the delivery port of the pump. This delivery port is connected to the hydraulic tool to be operated, and a pressure relief valve is used to maintain the fluid at the required pressure setting. This principle is illustrated through Figure 6.

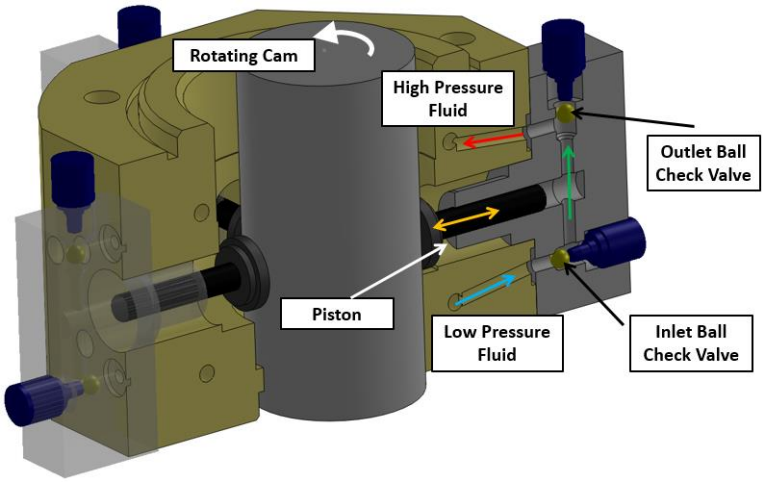

Figure 6: Detailed view of a displacement chamber depicting the principle of operation of the radial piston pump unit.

Rotating cam type radial piston units are predisposed to the possibility of high wear occurring at the cam/piston interface due to surface shearing from large contact loads. To prevent/reduce this, the present unit consists of the eccentric cam being supported by rolling element bearings that rest on a free-to-rotate outer race which are in contact with the pistons (Figure 7).

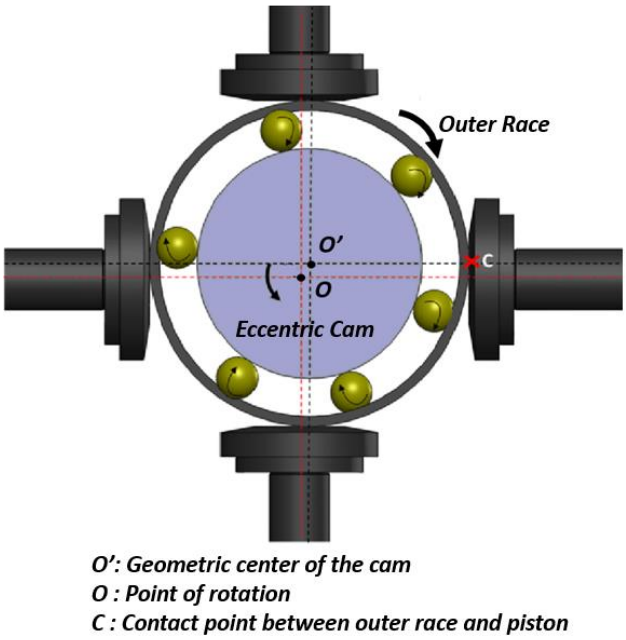

Figure 7: Depiction of the eccentric cam of a radial piston pump along with rolling element bearings and an outer race resting on all the pistons.

1.4 Research Objectives

The primary objective of the present research was to further the goal of enabling the design of efficient and durable radial piston machines through virtual prototyping. To this end, experimental and numerical strategies were devised to study the lubricating interfaces in a given reference machine and to propose design modifications that would allow such machines to function more efficiently and ensure that they operated in the regimes of full film lubrication.

In order to achieve this aim, a novel Mixed Fluid Structure Interaction (FSI) based Elastohydrodynamic (EHD) model for flow through the piston/cylinder interface was proposed considering several coupled phenomena such as:

- Pressures generated and the velocities of the piston/cylinder lubricating gap flow
- Micro-motion of the pistons within the stationary cylinders
- Load shared between the elasto-plastically deformed asperities present on the surface of the solid components (i.e. piston and cylinder) and the lubricating fluid in the gap.

- Elastic deformation of the solid components due to the pressure generated within the fluid in the gap as well as the asperity contact pressures in order to propose solutions leading the lubrication shifting from the mixed-EHD regime to the full EHD regime.

This mixed lubrication model was developed primarily to analyze the effect of surface profile modifications, such as designing circumferential piston grooves in enabling improved balance for the piston tilt within the cylinder, in order to ensure full film lubrication during pump operation. The model was also used to test the effect of these grooves in improving the lubricating performance of the pump by analyzing the losses in the piston/cylinder lubricating gap.

Another original contribution of this work involved devising an experimental methodology to analyze the motion of the free-to-rotate outer race due to the dynamic loading conditions of all four pistons during the pump operating cycle. The results of study were coupled with a pre-existing numerical model for the analysis of the friction coefficient at the cam/piston interface. This allowed for a better prediction of the friction forces acting on the piston due to the outer race, ultimately influencing the micro-motion of the piston during pump operation.

The procedures developed in this research have tremendous potential in the virtual designing of efficient and durable high pressure radial piston machines by considering important physical effects in both the lubricating interfaces present. Also, this tool developed can be used to explore surface features and analyze new designs of radial piston machines.

1.5 Work Structure: A Summary

At the outset, it is perhaps helpful to the reader to have an understanding of the information structure presented within this work due to the use of various models developed both in this work, and in the past, for the various results of the research presented in this study. The following points will clarify the order in which the work has been presented.

- Chapter 2 presents a description of the state of the art in the modeling of radial piston machines, lubricating gap models for the different tribological interfaces in positive displacement machines, an overview on mixed lubrication models developed for different applications in the past, and a literature review of the various analyses performed on surface modifications (such as the inclusion of grooves) in positive displacement machines with the primary goal of enhancing lubrication performance.
- Chapter 3 describes the various models used in the present research.
  - The geometric model and the global fluid dynamic model, both first developed in [6] are described in order to demonstrate the need for certain parameters generated that are used for the gap models as inputs and boundary conditions.
  - The FSI model for the piston/cylinder interface [6, 52] is next discussed since it is used to obtain results under the full film EHD assumption for the fluid in the piston/cylinder interface. An accurate estimation of the variation of the friction coefficient at the cam/piston interface is used in the force balance of the piston while implementing this model. Also, the results obtained using this model are used in the comparison against the mixed FSI-EHD model to demonstrate the differences between the two models.
  - Next, the novel mixed FSI-EHD model developed in this work is described in order to demonstrate the necessity of incorporating the effects of surface roughness, asperity deformations, and load sharing between the fluid film and asperities in the regions of low film thicknesses.
  - Finally, the line EHL friction model for the evaluation of the variation of the friction coefficient at the cam/piston interface [6] is described for use in conjunction with the experimental results of the cam kinematics.
- Chapter 4 delves into the experimental evaluation of the variation of the angular velocity of the free-to-rotate outer race. This experimental methodology was conceived as a product of the work done in research.
  - The results obtained from this experiment are used in the evaluation of the friction coefficient using the cam/piston friction model described in the previous chapter.

  - The resulting piston tilt, gap heights and pressure profile in the piston/cylinder interface (assuming full film lubrication) using the friction results are also described.
  - A comparison of the piston tilt and performance parameters is also made between the results obtained using the friction model and the results obtained while assuming a constant friction coefficient between the piston and cam over one pumping cycle.

- Chapter 5 demonstrates the role that surface modifications such as circumferential piston grooves have on the piston's hydrodynamic balance and lubrication performance parameters over a pumping cycle. The results shown make use of the FSI-EHD full film model and the friction model for the cam/piston interface, both described in Chapter 3.

- Chapter 6 discusses the importance of incorporating the effects of mixed lubrication in the regions of low film thicknesses. Comparisons are made between the full film FSI-EHD model and the mixed FSI-EHD model for the piston tilt and performance. The impact of grooves on the tilt and performance assuming mixed lubrication effects are also discussed. The results from the cam/piston friction model are used to make the comparisons presented in this chapter.

- Chapter 7 provides a summary of the work done in this research as well as discusses directions for future research that could be conducted to further the understanding of the development of a robust virtual prototyping tool for radial piston machines.

CHAPTER 2. LITERATURE OVERVIEW

In this chapter, the literature related to the different aspects of the present research have been categorized into several sections. In particular, various modeling techniques adopted for characterizing the design of positive displacement machines – with special emphasis on modeling lubricating interfaces – have been highlighted.

2.1 Modeling of Radial Piston Machines

At present, radial piston machines are – by and large – designed through performing a series of testing which involves large costs and time consumption. Due to this fact, there has been little reported work on the modeling of these positive displacement machines. Chapple [1] developed an analytical model of a radial piston motor for the evaluation of factors affecting motor performance, including friction in ball joints. While this work focused on analyzing the different forces acting on the components and the motion parameters involved, the flow features in the motor were not studied. Ivantysyn and Ivantysynova [2] proposed kinematic relations and force analyses for the characterizing the flow in rotating cam type and rotating cylinder type radial piston machines. Kleist [3, 4] developed an isothermal model to describe the gaps flow through radial piston machines. However, this was based on the assumption that the moving parts behaved as rigid bodies. Mortenson [5] analyzed the efficiency of a radial piston pump used in a wind transmission system. While the flow features were studied in detail, a simplified assumption was used for modeling the lubricating gaps.

More recently, Agarwal et al. (2014) [51, 52] developed a comprehensive multi-domain simulation tool to analyze the flow features in a radial piston pump coupled with FSI-EHD model for the piston/cylinder lubricating interface.

To the best of the author's knowledge, the work by Agarwal (2014) that analyzed the friction at the cam/piston interface in radial piston machines was the only work on this topic [6]. This work is an extension of the work done in [6].

2.2 EHD Models for Tribological Interfaces

In the last few years, the analysis of the lubricating interfaces in positive displacement machines has been a subject of active research. The importance of including the effects of micro-motion of the moving surfaces that comprise these interfaces have been presented in multiple studies. Fang and Shirakashi (1995) first proposed a methodology to predict the location of the piston considering a force balance and contact forces in the piston/cylinder interface of axial piston machines [7]. Olems (2002) further developed this study by incorporating a non-isothermal model in this analysis [8]. Wieczorek (2002) implemented Olem's approach into CASPAR which is a simulation tool that analyses all three lubricating gaps present in a swash plate type axial piston machine [9]. This phenomenon was also incorporated in external gear machines (EGMs) [10] to analyze the tilt of the gears and lateral plates in the lateral lubricating interfaces of EGMs.

Detailed models involving elastic and thermal surface deformation effects have been presented for the different lubricating interfaces of axial piston machines – the piston/cylinder interface [9, 11-16], the slipper/swashplate interface [17, 18] and the cylinder block/valve plate interface [19-21]. Similar analyses [10, 22] have been performed in EGMs in the analysis of the lateral lubricating interface between the gears and the lateral plates. All of these models have been validated with excellent agreements with experimental measurements, thereby underlining the importance of including EHD and thermal effects in positive displacement machines.

Apart from positive displacement machines, there have been significant contributions in developing fully coupled EHD models to study the lubricating interfaces of conformal surfaces such as journal bearings [23-26], connecting rod bearings [27] and finally, in the interfaces of non-conformal contacts such as the mating of spur gears [28].

2.3 Mixed Elastohydrodynamic Lubrication

Lubricating flow in the mixed lubrication regime is typically modeled using the Average Reynolds equation [29] developed by Patir and Cheng (1978). The pressure distribution is solved by considering the flow through a rough bearing as compared to that of a flow through a smooth one. Chengwei and Linqing (1989) presented characteristic expressions for the Gaussian distribution of surfaces using the average flow Reynolds equation [32]. Lee and Ren (1996) presented a comprehensive asperity contact model by considering elastic-plastic deformation of the surface asperities [30]. Harp and Salant (2000) included an inter-asperity cavitation sub-model to model the interaction of the surface features with the flow [33]. Meng et al. (2010) proposed a contact factor to be taken into consideration while modeling the average flow Reynolds equation for any measured surface [31].

There has been great strides in modeling mixed lubrication in conformal contacts. Shi and Wang (1998) presented for the first time, a comprehensive mixed-thermoelastohydrodynamic (TEHD) model for the lubricating interfaces in journal bearings [34]. However, the load support due to asperities was evaluated using simplified approaches. Wang et al. (2002) added an advanced surface asperity contact to the previous work by considering elastic-plastic deformations of the surface asperities [23, 35]. Kraker et al. (2007) used a mixed-TEHD model with a simplified asperity contact model to generate Stribeck curves for water lubricated journal bearings [36].

In the area of hydraulics, there have been a few noteworthy contributions in the field of mixed lubrication modeling. Yamaguchi and Matsuoka (1992) proposed a mixed lubrication model applicable to bearing and seal parts of hydraulic equipment [37]. Kazama and Yamaguchi (1993) applied a mixed lubrication model for hydrostatic thrust bearings of hydraulic equipment [38]. Kazama (2005) developed a numerical simulation model for the slipper in water hydraulic pumps and motors operating under mixed lubrication [39]. Fang and Shirakashi (1995) examined the mixed lubrication characteristics between the piston and cylinder in axial piston swash plate type piston pump-motor [7]. Wegner et al. (2016) experimentally validated a model incorporating the

effects of surface roughness, solid contact, surface deformation and micro-motion for the cylinder block/valve plate interface of axial piston machines [40].

2.4 Effects of Surface Modifications on Lubrication Performance

Micro-surface shaping in axial piston machines has been a topic of study for many years. There has been considerable work done in terms of analyzing different piston surface features such as the barrel shape, a sine waved barrel, a half barrel shape and a sine wave [41, 42]. Ivantysynova and Garrett (2009) have even filed a patent for a sine wave shaped piston, in which a maximum of 60% decrease in power losses were achieved in simulation [43]. Although the type of modification analyzed in this study pertains to grooves, which fall into the category of surface modifications where the scale length assessed is more of the order of mm, it is relevant to point out that similar types of advantages are to be gained as those from micro-surface shaping.

There have been many studies related to the introduction of grooves. Park (2008) studied the effect of piston grooves on pressure build-up in the piston/cylinder interface of oil-lubricated axial piston machines [44]. Berthold (1999) filed a patent for the use of pressurized circumferential grooves in the cylinder bore of axial piston machines, where the grooves are connected to the unit's high pressure side and serve to hydrostatically balance the piston [45]. Majumdar et al. (2004) studied the effect of varying the widths of axial grooves in water-lubricated journal bearings on the stability of the journal as well as the load-carrying ability of the interface [46]. Basu (1992) simulated radial grooves in face seals [47]. Razzaque et al. (1999) analyzed the effect of groove orientation on the hydrodynamic behavior of wet clutch coolant films [48]. Kumar et al. (2009) performed an analysis of a grooved slipper in an axial piston pump [49]. More recently, Kumar and Bergada (2013) studied the effect of piston grooves on axial piston pump performance via a CFD analysis [50].

CHAPTER 3. NUMERICAL MODELS FOR LUBRICATION PERFORMANCE ANALYSIS

3.1 The Multi-Domain Simulation Tool

In this chapter, an overview of the multi-domain simulation tool developed at the Maha Fluid Power Research Center [51, 52] is presented. This tool comprises the various modules necessary to analyze the lubricating performance of rotating cam type radial piston pump designs. The overall framework of the simulation tool consisting of the various submodels developed and the exchange of information between each of these submodels is shown in Figure 8. The capabilities of the simulation tool include modeling the various aspects of radial piston pump – the motion of the cam and each piston, flow parameters such as the flow rate and pressure ripple at the pump outlet, the instantaneous pressure variation within each of the displacement chambers, and the flow features in the two lubricating interfaces present – the piston/cylinder interface and cam/piston interface.

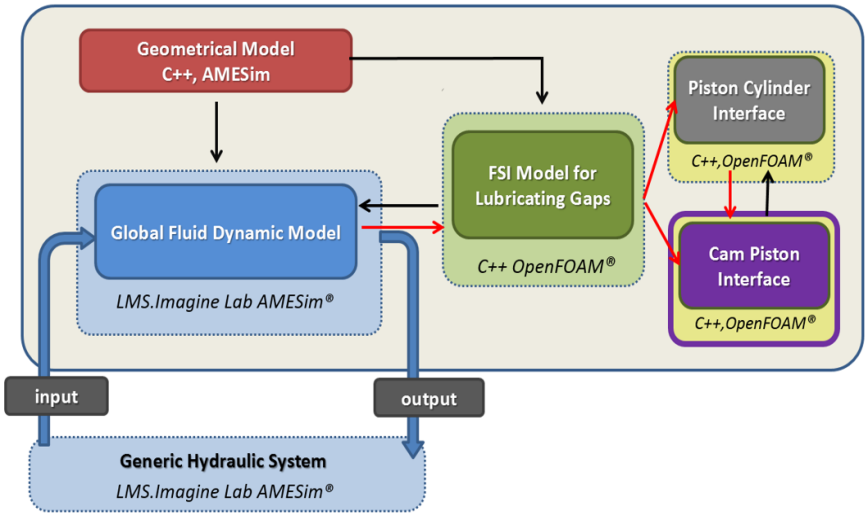

Figure 8: Schematic of the multi-domain simulation tool for radial piston machines.

In the following sections, each of the submodels used to evaluate the different parameters necessary to model radial piston pumps are briefly explained.

3.1.1 Geometric Model

The geometric model is responsible for the calculation of the kinematic parameters of the cam and each piston. The parameters generated here are used as inputs for the other modules that evaluate the flow features of the pump. This model is a standalone application developed using C++ and is able to evaluate the kinematic parameters for cam and piston surfaces of arbitrary shapes. The various parameters evaluated for use in different modules are listed as follows:

Global Fluid Dynamic Model: Instantaneous values of piston displacement, displacement chamber volumes and the velocity of the translating pistons are generated for use here.

Piston/Cylinder Gap Model: Instantaneous length of the lubricating oil film between the piston and cylinder is generated, along with the coordinates of the contact point between the cam and piston since the contact force at the cam/piston interface acts at this point.

Cam/Piston Gap Model: Cam/Piston contact coordinates are used here to calculate the surface velocity parameters in the EHL line contact model.

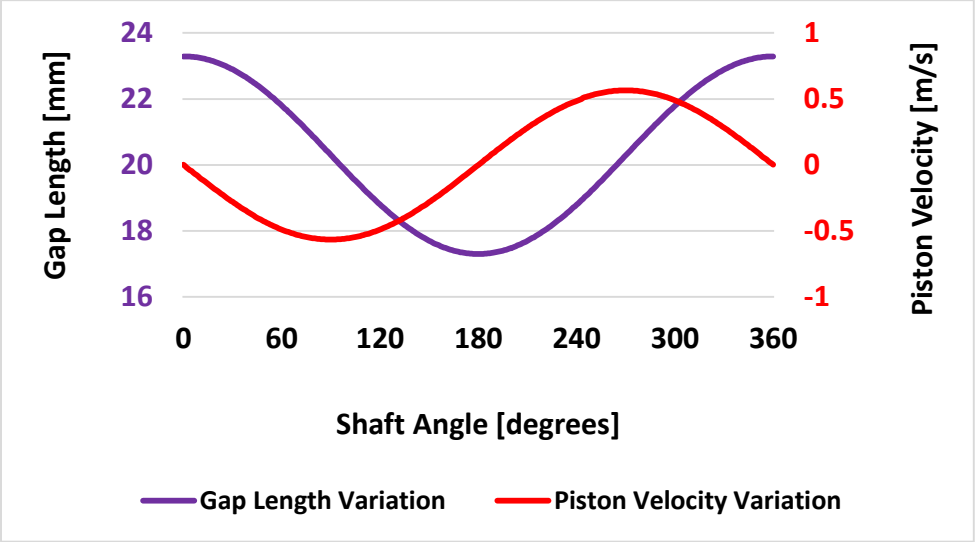

Figure 9: Variation of the piston/cylinder gap length and piston velocity with shaft angle for a single pumping cycle. Shaft speed = 1800 rpm.

Figure 9 illustrates an example of some significant geometrical parameters evaluated by this model along with their variations as a function of the shaft angle. Here, a shaft angle of 0^o corresponds to piston 1 positioned at the bottom dead center (BDC). The graphs shown are the instantaneous values of each parameter over one revolution of the shaft.

3.1.2 Global Fluid Dynamic Model

The global fluid dynamic model works in co-simulation with the piston/cylinder lubricating gap model to set the pressure boundary conditions needed for the latter. The goal of this model is to characterize the flow throughout the entire radial piston pump unit. This is accomplished through a lumped parameter modeling approach. This methodology has been implemented with great success for other positive displacement machines in the past such as axial piston machines and EGMs [9, 53], and has also been validated for use in radial piston machines [51]. The primary output of this module includes the evaluation of the main flow parameters in the pump namely the flow rate, pressure at the pump outlet, as well as within each displacement chamber.

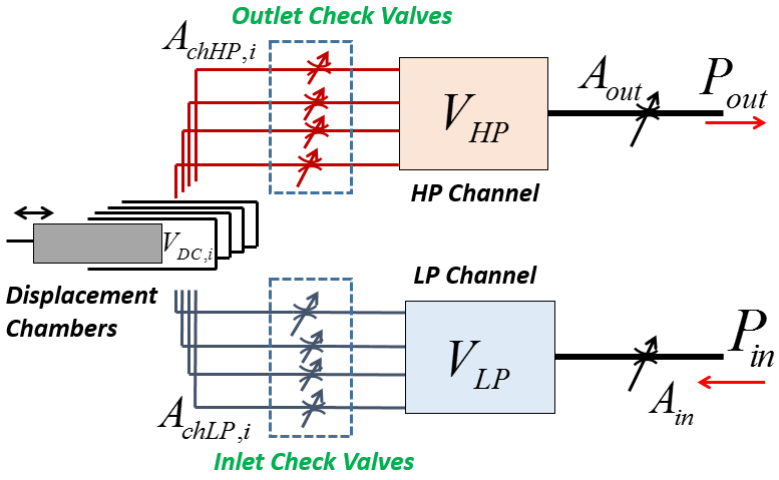

Figure 10: Schematic of the lumped parameter model for the reference radial piston pump.

The fluid dynamic model was created using the LMS.Imagine Lab AMESim® environment using custom built libraries combined with the standard libraries of the code in C language. The radial piston machine is divided into separate control volumes corresponding to each displacement chamber and LP/HP channels. Figure 10 represents

the schematic of the lumped parameter modeling approach used to analyze the reference design of the radial piston pump.

In order to calculate the various flow parameters across the entire pump system, flow equations are solved for each of the control volumes and are coupled together. Here, the equations for a single displacement chamber control volume (Figure 11) are shown. Similar equations are solved for the HP and LP channels.

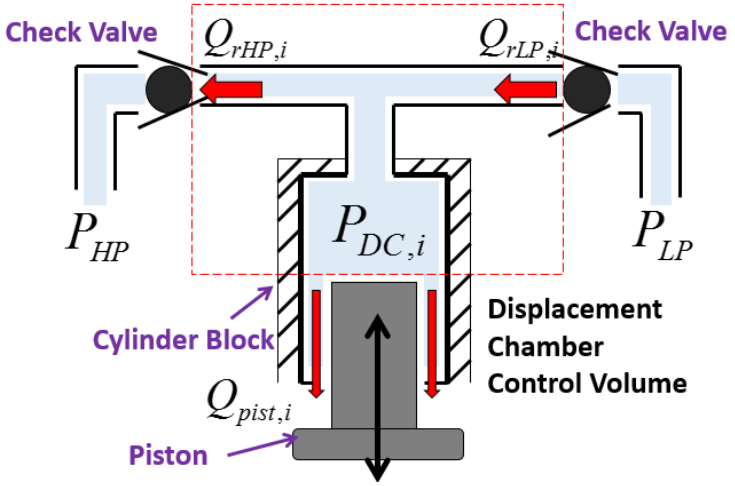

Figure 11: Schematic of a single displacement chamber control volume

The rate of change of pressure in each displacement chamber control volume is modeled using the pressure build-up equation:

$$\frac{dP_{DC,i}}{dt} = \frac{K}{V_{DC,i}}\left[-\frac{dV_{DC,i}}{dt} - \left(Q_{rHP,i} + Q_{rLP,i} + Q_{pist,i}\right)\right] \tag{3.1}$$

The terms represented in Equation (3.1) are illustrated in Figure 11. $\frac{dV_{DC,i}}{dt}$ represents the rate of change of displacement chamber volume and can be represented by the following equation:

$$\frac{dV_{DC,i}}{dt} = A_{DC,i}\frac{ds_P}{dt} + \frac{dV_{HPv,i}}{dt} + \frac{dV_{LPv,i}}{dt} \tag{3.2}$$

Here, $\frac{ds_P}{dt}$ is the instantaneous piston velocity that is generated using the geometric model.

In order to solve for the pressure distribution in Equation (3.1), the flow rate terms across each of the check valves present near the displacement chamber ($Q_{rHP,i}$, $Q_{rLP,i}$) are required. These are found by solving orifice flow equations for turbulent flow:

$$Q_{rHP,i} = \alpha A_{HPv,i}\sqrt{\frac{2\left|P_{DC,i} - P_{HP}\right|}{\rho}}\, sgn(P_{DC,i} - P_{HP}) \tag{3.2}$$

$$Q_{rLP,i} = \alpha A_{LPv,i}\sqrt{\frac{2\left|P_{DC,i} - P_{LP}\right|}{\rho}}\, sgn(P_{DC,i} - P_{LP}) \tag{3.3}$$

$A_{HPv,i}$ represents the orifice area of connection between the HP channel and displacement chamber which is determined by the opening of the outlet ball check valve (depicted in Figure 11). Similarly, $A_{LPv,i}$represents opening area of inlet ball check valve. The valve opening areas in orifice flow equations were evaluated by a careful selection of AMESim libraries in which the effects of geometry are included in detail. The $\frac{dV_{val}}{dt}$ terms in Equation (3.2) take into account the volume change due to movement of the ball in the check valve and are incorporated in the valve models.

A laminar flow equation for fully developed laminar flow which takes into consideration the relative motion between surfaces is used to model the leakage through each displacement chamber ($Q_{pist,i}$):

$$Q_{pist,i} = w_{gap}\left[\left[-\frac{h^3}{12\eta}\left(\frac{\Delta P}{L}\right) + \frac{hu}{2}\right]\right. \tag{3.5}$$

where, u is the velocity of the wall, L is the gap length, h is the gap height and w_{gap} is the gap width.

Further details of the global fluid dynamic model and its outputs can be found in [51].

The fluid dynamic model, by itself, does not take into consideration important features such as piston micro-motion and hydrodynamic effects. These physical effects greatly influence the accuracy of the leakages being calculated, which in turn influence the accuracy of the shear and volumetric losses that occur that characterize the durability of the unit. Equation (3.5) is adopted only as an initial guess for the leakages in order to find

the displacement chamber pressures (shown in Figure 12) which are then used as boundary conditions for more complex lubricating gap models that do consider the aforementioned effects. The leakages obtained using the gap models are then used to refine the displacement chamber pressures, thereby forming a coupled system. The next sections describe the lubricating gap models for the two interfaces present in the reference design considered – the piston/cylinder interface and the cam/piston interface.

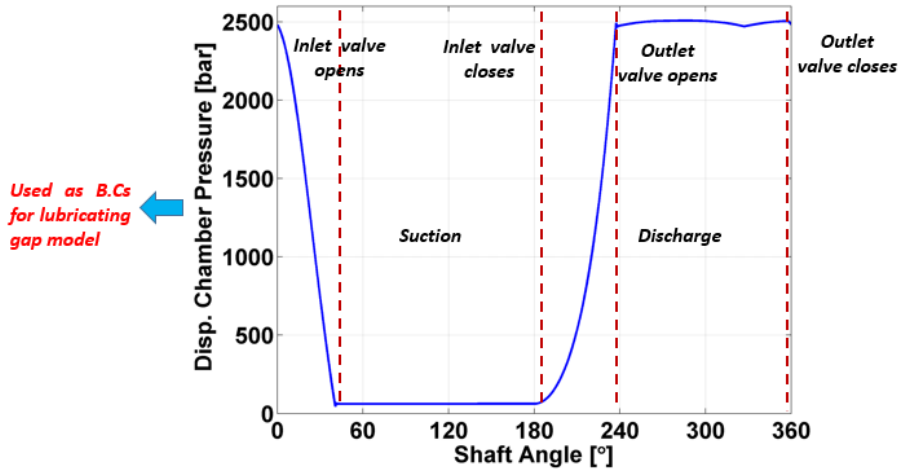

Figure 12: Variation of the instantaneous pressures within a single displacement chamber used as boundary conditions for the gap model, along with the timing of the valves.

3.2 Fluid Structure Interaction Model of the Piston/Cylinder Interface

The FSI model for the piston/cylinder interface developed in [6, 52] forms one of the core components for the study of this lubricating gap in radial piston machines. The fundamental assumption made while developing this gap model is that the load is completely supported by the fluid film that is present between each piston and cylinder during pump operation at every operating condition.

In this section, an overview of the FSI model for the piston/cylinder interface is presented. This model has been developed by taking into account various physical phenomena that occur within a radial piston pump, including structural elastic deformation of the solid surfaces (piston and cylinder) due to high pressures developed within the gap, and the micro-motion of the piston due to the different forces acting on it, thereby causing a

squeezing of the fluid film. These effects are characterized by the different submodels present within this tool along with the flux of information passing between each other. The submodels can be classified into two broad categories, namely Pre-processors and Solvers. A brief description of the pre-processors are provided as follows:

Dynamic Fluid Mesh Generator/ Solid Mesh Generation: Finite volume meshing of the fluid film geometry (as the piston dynamically translates within the cylinder during every shaft revolution) and the solid components (piston and cylinder).

Boundary conditions setup: Pressure boundary conditions on the faces of the fluid mesh.

The solvers available within the FSI model are listed below:

Gap Flow Model: Finite volume solver for the Reynolds equation for the fluid.

Structural Model: Finite volume solver for the elasticity equations for the solids, i.e. the piston and the cylinder.

Force Balance Model: Accounts for the balance of the forces acting on the pistons.

The FSI model was created as an independent application using the C++ programming language and was linked with open source libraries such as OpenFOAM [54] for FV discretization of the PDEs involved along with linear system solving, GSL [55] for multidimensional root-finding and interpolation.

Before elaborating on the various submodels listed, it is important to analyze the variation of the fluid film geometry and the control variables that drive the simulation.

3.2.1 Piston/Cylinder Fluid Film Geometry

The piston/cylinder geometry is modeled assuming that the piston moves axially within the stationary cylinder (sleeve). The varying eccentric motion of the piston with respect to the cylinder axis dictates the squeezing of the gap film, thus generating a dynamic gap height profile at every position of the piston.

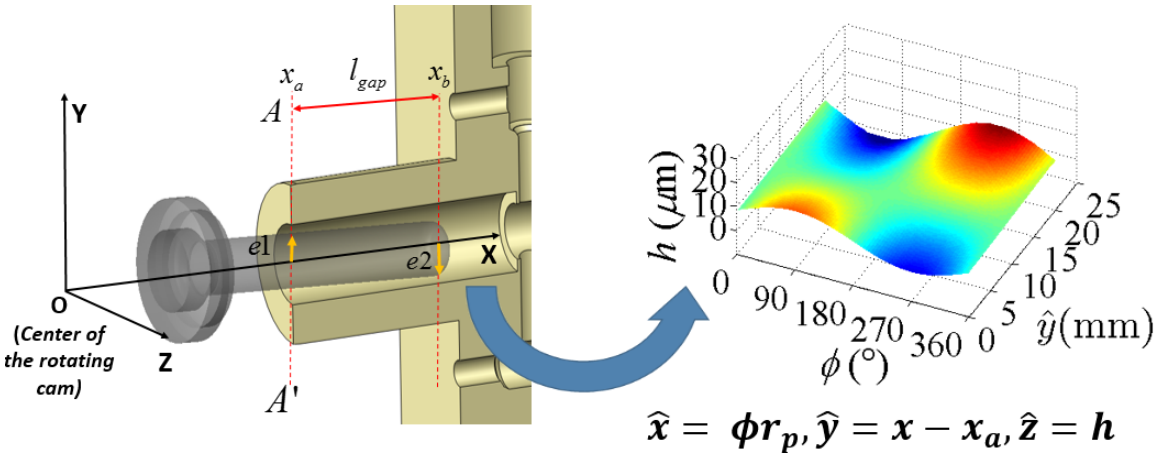

Figure 13: Piston tilt parameters and unwrapped film thickness configuration.

In Figure 13, the main geometric parameters used to define the piston/cylinder interface characteristic geometry are depicted. The local film thickness h is defined at each point within the fluid domain by a precise value of the piston eccentricity vector, $\{e_1, e_2\}$ as developed in [6, 52].

Since all the forces acting on the piston (discussed in detail later) in the present pump geometry are in the x-y plane (defined in Figure 13) with no force component acting on the piston along the z-axis, 2 degrees of freedom e_1 and e_2 are sufficient to describe the piston position in any arbitrary configuration when considering micro-motion.

The film thickness value h_g at any arbitrary point in the fluid domain can be expressed as a function of the circumferential angle ϕ and distance along the piston axis x as follows [6]:

$$h_g(x,\phi) = \sqrt{(\,(r_c sin\phi - y_m(x))^2 + {r_c}^2 cos^2\phi)} - r_p \tag{3.6}$$

where:

$$y_m(x) = \frac{e_2 - e_1}{l_{gap}}(x - x_A) + e_1 \tag{3.7}$$

Here, x_A is the distance of the cylinder face from a reference origin and l_{gap} is the instantaneous length of the lubricating film region.

Equation (3.6) considers the piston and cylinder to be rigid bodies. While the fluid film is present in a circular configuration in the actual pump, in order to solve for the fluid pressure generation, the curvature of the film geometry is neglected as the clearance between the piston and cylinder is very small as compared to the piston diameter. Thus, a Cartesian coordinate system can introduced, wherein the film shape can be unwrapped and viewed as a periodic stationary profile with length $2\pi r_p$. The unwrapped Cartesian coordinate system presents the following coordinates:

$$\hat{x} = \phi r_p, \quad \hat{y} = x - x_a, \quad \hat{z} = h_g \tag{3.8}$$

Figure 13 also shows a typical view of the piston/cylinder interface fluid film thickness on the unwrapped Cartesian coordinate system for the depicted piston position.

The next section deals with the mesh generation of the fluid and solid domains.

3.2.2 Mesh Generation and Boundary Conditions

3.2.2.1 Dynamic Fluid Mesh Generation

A mesh generation module for creating the mesh for the fluid domain was developed in C++ as part of the preprocessing for the FSI model. From the unwrapped configuration of the fluid film as seen in the previous section, it is observed that the computational fluid domain is now a rectangular Cartesian grid with the gap height varying with both $\hat{x}$ and $\hat{y}$ coordinates. Since the lubricating gap domains are characterized by film thicknesses of the order of microns, the variation of fluid pressure in the $\hat{z}$ direction can be neglected and pressure is considered a function of $\hat{x}$ and $\hat{y}$ only.

A typical computational grid used for this problem is shown in Figure 14. Since the gap length varies as the shaft rotates over one revolution, a dynamic mesh generator is used to create meshes for each time step over one revolution of the shaft.

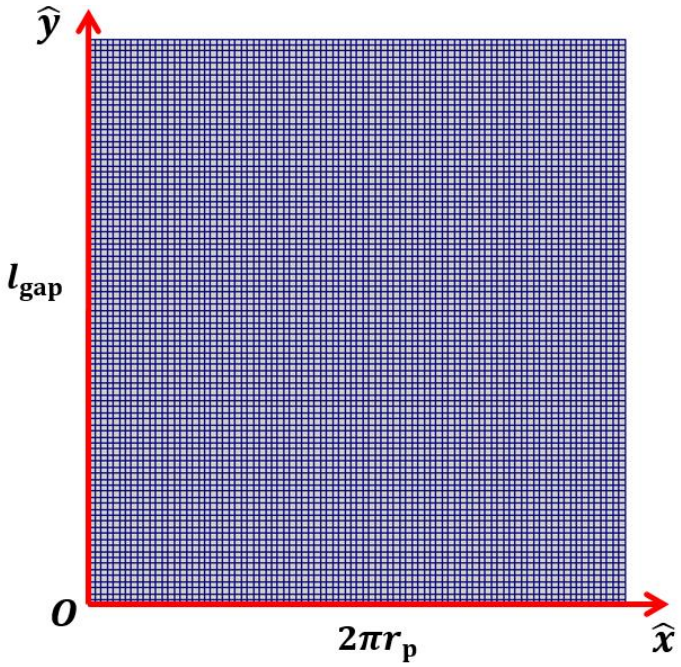

Figure 14: Typical computational grid in the unwrapped configuration used for the fluid domain in the gap.

The boundary conditions employed to numerically solve for the pressure within the grid are also depicted in Figure 15 (A). The mesh boundary that is in contact with the displacement chamber end is assigned the value of the displacement chamber pressure at that particular instant of time during the shaft's revolution. The dynamic variation of the displacement chamber pressure with the rotation of the shaft that was found from the global fluid dynamic model (as seen in Figure 12) is used to specify the instantaneous displacement chamber pressure at each grid created for one revolution of the shaft. At the lower boundary of the mesh shown, the pressure is set to a constant ambient pressure (0 bar) as it is exposed to the drain. At the boundaries on the left and right of the grid, a cyclic boundary condition is specified, since they both represent the same set of points in the actual wrapped configuration.

The grid shown in Figure 15 (A) proves to be sufficient for analyzing the gap features when the pistons do not possess any out of the ordinary surface features. However, when there are circumferential grooves machined along the lengths of each piston, the assumption which allows for the use of a 2D grid for this analysis fails. This is because

the gap clearance will now be of the order of mm at the location of the grooves, which cannot be considered negligible compared to the piston length and circumference. For this reason, a control volume approach such as the one used in the lumped parameter model is adopted to estimate the fluid pressure at each groove location.

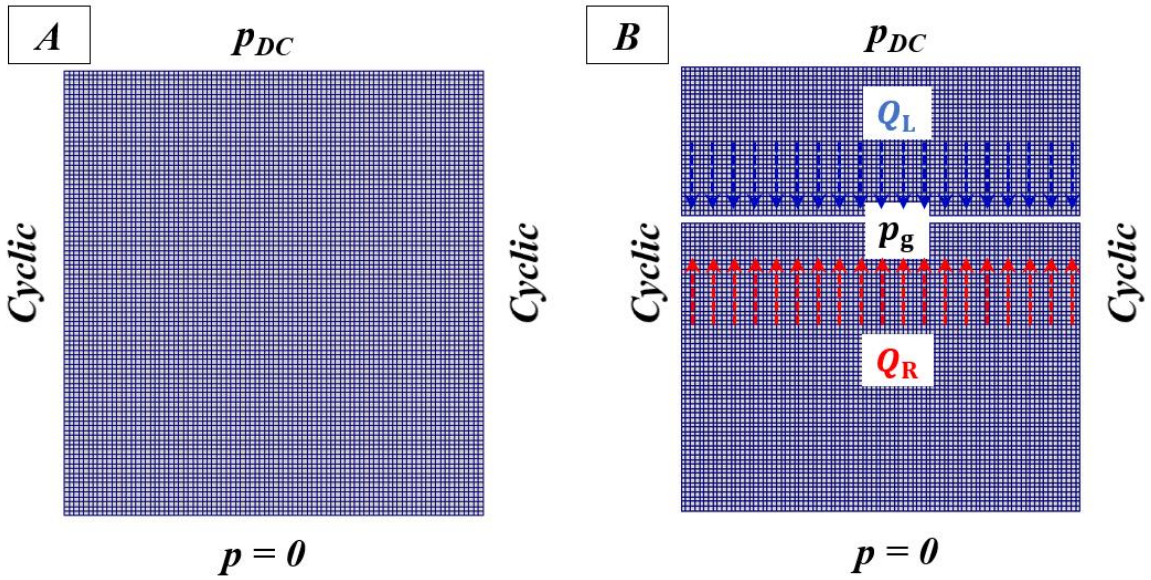

Figure 15: (A) Pressure boundary conditions specified at all the boundaries of the grid, (B) Pressure boundary conditions specified to include the boundary pressures at the location of a groove.

For the case of a grooved piston, a 2D grid can be used to solve for the pressures within the gap everywhere except at the locations of the grooves. Therefore, the computational mesh can be split into different parts where the location of each separation signifies the presence of a groove, as shown in Figure 15 (B). The same boundary conditions used in Figure 15 (A) hold true for this case as well. However, new boundaries are created due to the presence of the grooves. Therefore, there is a need to determine the pressure of the fluid within the grooves in order to evaluate the pressures at all of the other points on the grid. For this reason, the pressure built-up equation is used to evaluate the groove pressures which may then be used as the boundary conditions at the new "groove" boundaries on the computational grid. The equation solved is shown as follows:

$$K\frac{Q_L + Q_R}{V_g} = \frac{dp_g}{dt} \tag{3.9}$$

where, Q_L and Q_R are the flow rates of the fluid entering a groove from both of its sides, K is the hydraulic oil's bulk modulus, p_g denotes the pressure within the groove at a given time instant and V_g is the volume of the groove found from its geometry.

3.2.2.2 Generation of Solid Meshes

The 3D FV meshes (shown in Figure 16) for the solid bodies (piston and cylinder) were generated using the commercial code ANSYS [56]. Tetrahedral, unstructured meshes were chosen for the solid components since this allowed for a high conformity to their actual geometries.

The dynamic linking of the solid and fluid domains is one of the key aspects of the FSI model and this requires information to be transferred between the fluid mesh to the two solid meshes, and vice-versa. To accomplish this, the number of fluid cells was kept much greater than the number of solid meshes, and the nearest-neighbor searching algorithm was used to link each solid face to a group of fluid cells.

The next sections discuss the evaluation of the fluid pressures within the gap domain as well as the evaluation of the structural deformation due to this pressure generation.

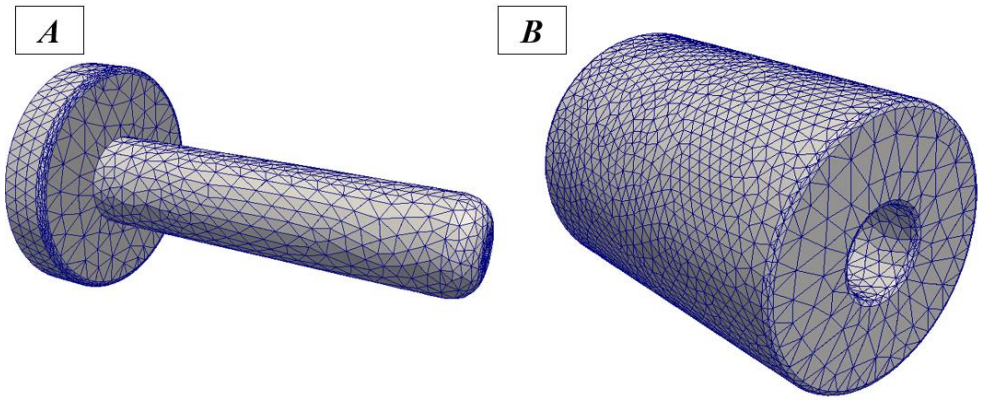

Figure 16: 3D meshes for the solid domains: piston (A) with 27,000 nodes and cylinder (B) with 29,000 nodes.

3.2.3 Gap Flow Model

The pressure distribution within the piston/cylinder interface is solved with the help of the Reynolds equation, which is derived from the well-known Navier-Stokes equations by taking into consideration certain simplified assumptions suitable for this case [57]. However, in order to account for the fact that both the piston and cylinder surfaces are expected to deform, an appropriate form of the Reynolds equation was derived for the geometry of the piston/cylinder interface in radial piston machines. The detailed derivation of this form of the Reynolds equation can be found in [6].

$$\nabla.\left(\frac{\rho h^3}{12\eta}\nabla p\right) - \left(\frac{\rho \boldsymbol{V}_b}{2}\right).\nabla h - \rho \boldsymbol{V}_b.\nabla h_b - \rho\frac{\partial h}{\partial t} = 0 \tag{3.10}$$

where, $h = h_t - h_b$ as shown in Figure 17. It can be seen that the velocity of the top surface $\boldsymbol{V}_t = 0$ since the cylinder is stationary, while the velocity of the lower surface is equal to the translational velocity of the piston $\boldsymbol{V_b} = \boldsymbol{V_p}$.

The dependence of fluid properties that are involved in Equation (3.10), namely density and viscosity, are modeled using the relations found in [2].

$$\rho = \rho_0(1 + \beta_p(p - p_0)) \tag{3.11}$$

$$\eta = \eta_0 e^{\alpha_p p} \tag{3.12}$$

A finite volume solver for the Reynolds equation was implemented through an application developed in C++. The pressure is solved for using a Preconditioned Conjugate Gradient algorithm with a Diagonalized Incomplete Cholesky preconditioner [54].

Isothermal conditions are assumed throughout this research. It has been observed in previous studies of lubricating gaps [11] that thermal effects are less pronounced in the piston/cylinder interface of piston machines compared to the impact of elastic deformation on the overall results. Since these effects were observed to be negligible in [11], it was decided not to implement them at this stage. However, they will be a subject

of future investigation, where improvements to the current FSI model can be made by including the effects of heat generation and thermal deformation.

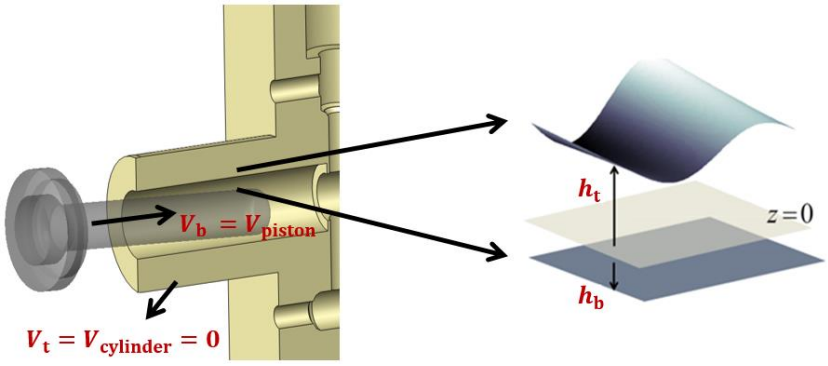

Figure 17: Terms present in Equation (3.10): top surface (h_t) and bottom surface (h_b) from a reference plane; fixed cylinder ($\boldsymbol{V}_t = 0$) and moving piston ($\boldsymbol{V}_b = \boldsymbol{V}_{piston}$).

3.2.4 Structural Deformation Model

The structural components of the lubricating interface, namely the piston and the cylinder, experience high pressure loads and tend to elastically deform. The solid deformation is modeled using a steady state finite volume stress/deformation formulation described in [58], which has been used in the modeling of EGMs [10, 22] and radial piston machines [6, 52] in the past.

$$\frac{\partial^2(\rho \boldsymbol{u})}{\partial t^2} - \nabla[2\vartheta + \lambda]\nabla \boldsymbol{u}] - \nabla[\vartheta(\nabla \boldsymbol{u})^T + \lambda \boldsymbol{I} tr(\nabla \boldsymbol{u}) - [(\vartheta + \lambda)\nabla \boldsymbol{u}] = \rho \boldsymbol{f} \tag{3.13}$$

Detailed discussion of the different criteria behind developing and formulating this FV deformation solver have been described in [6]. An offline scheme called the influence method was used to obtain the material deformation matrices for all the solid cells for both the piston and cylinder corresponding to a reference load applied to each individual boundary cell. Once the influence matrices (IM) are evaluated, the deformation of solid boundaries for actual pressure loads can be calculated using:

$$\Delta h = \sum_{j}^{N} IM_j \frac{p_j}{p_{ref}} + IM_{DC} \frac{p_{DC}}{p_{ref}} \tag{3.14}$$

where, Δh is the array containing the elastic deflection of each of the surface nodes of the solid domain and p_j is the external fluid pressure loading on these each of the N faces of the loaded surface. The influence coefficient IM_j represents the elastic deformation on the all the surface nodes due to a reference pressure load p_{ref} acting on j^{th} face. IM_{DC} is the influence matrix containing the elastic deformation of all the surface nodes from the displacement pressure load of the subjected surfaces.

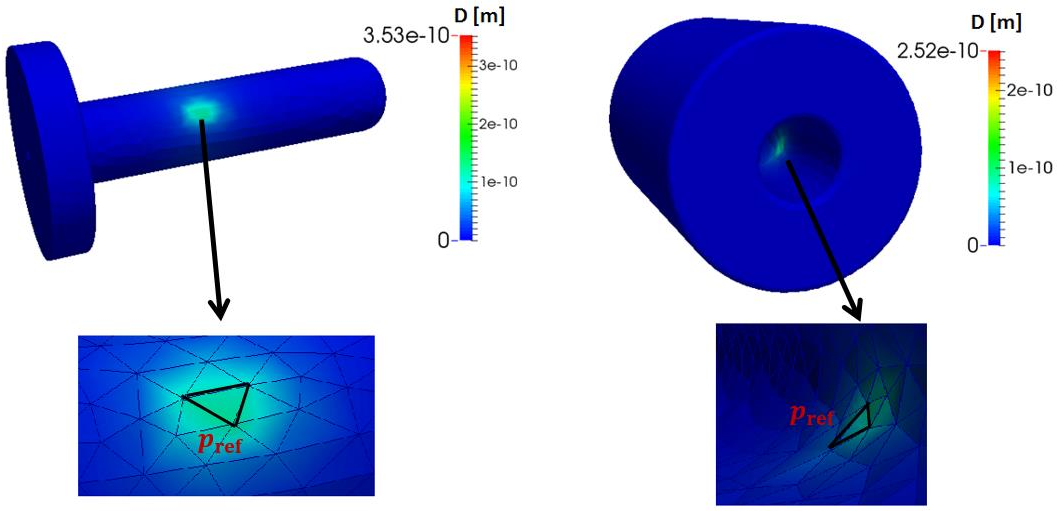

Figure 18: Deformations on the surfaces of the piston and cylinder due to a unit pressure applied at a single node. Ideal support constraint has been used for both geometries.

Figure 18 represents the deformation fields in the cylinder and piston on application of a reference pressure on a single cell. An ideal support constraint is implemented, which involves constraining the axes of both geometries. Further details related to the structural model are available in [6].

3.2.5 Dynamic Load Balance of the Piston

A balance of the various forces and moments acting on the piston is deemed necessary at each instant of the shaft's rotation in order to achieve an accurate prediction of the lubricating gap film thickness, since the hydrodynamic pressure generated by the fluid must be able to balance out all the external forces during the steady state operation of a

radial piston machine. The key assumptions made here include full film lubrication at every instant and the absence of metal to metal contact during pump operation.

The various external forces (structural) acting on the piston at any instant during pump operation are highlighted in Figure 19. One noteworthy feature of the radial piston machine that all the forces and moments act only along the $x - y$ plane.

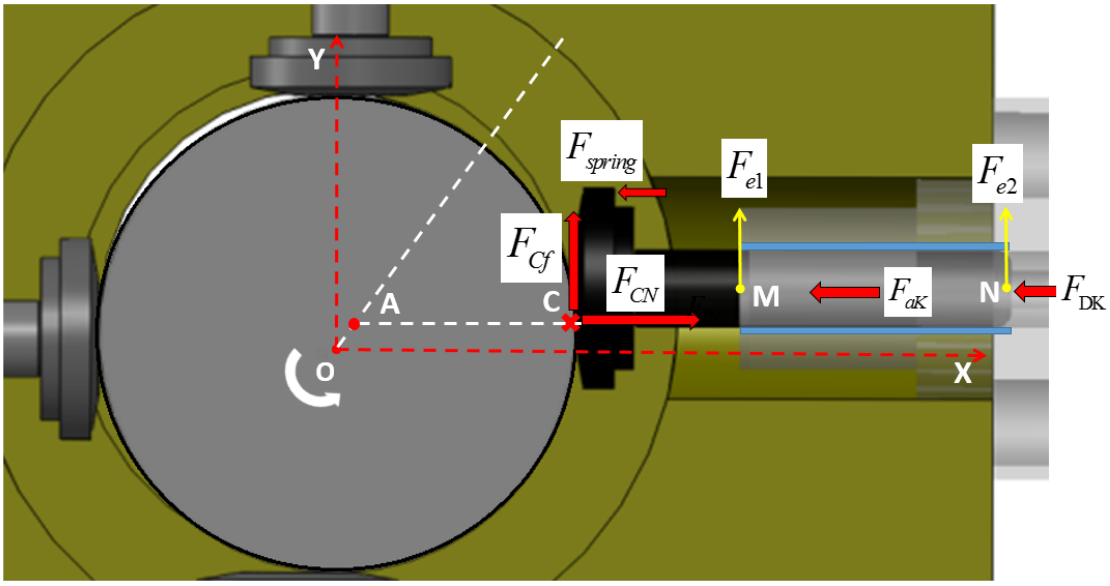

Figure 19: External forces (structural) acting on the piston at any given time.

The largest force acting on the piston is the pressure force F_{DK} from the displacement chamber pressure end. During the suction stroke, when these forces are lower in magnitude, the spring force F_{spring} ensures that the piston remains in contact with the shaft. The spring has not been depicted in the illustration, although they are present in the reference pump as shown in Chapter 1. The inertial forces acting on the piston were found to be small in magnitude as compared to the displacement chamber pressure forces, and hence neglected in this study. Another important force is the viscous friction generated by the shearing of the fluid film in the lubricating gap, F_{Tf}.The reaction force from the cam F_{CN} balances these forces along the x direction.

$$F_{CN} + F_{Tf} + F_{spring} + F_{DK} = 0 \tag{3.15}$$

In the y direction, the only side load present is the friction force exerted by the cam on the piston F_{Cf}. This is found from an offline analysis of the cam/piston interface as described in detail in the next chapter. This side force is balanced by the normal force exerted by the fluid film on the piston surface F_{TN}. However, due to the changing point of contact between the piston and the cam over one shaft revolution, a moment is created by the friction force F_{Cf} and the normal force from the cam F_{CN}.

All of these forces and moments can be condensed as described in the following balancing equations:

Force balance in the y direction:

$$F_{e1} + F_{e2} + F_{Cf} = 0 \tag{3.16}$$

Moment balance about point M (shown in Figure 19):

$$F_{e2}.\, l_{gap} - [F_{CN}.\, y_{cp} + F_{Cf}.\, (x_A - x_{cp})] = 0 \tag{3.17}$$

where, x_{cp}, y_{cp} are the coordinates of the contact point between cam and the piston.

To simplify the calculation process, all external forces and moments acting on the piston are resolved into an equivalent set of two forces F_{e1}, F_{e2} acting on either end of the lubricating gap as shown in Figure 19. The values of F_{e1} F_{e2} can be obtained by solving the Equations (3.15) – (3.17).

In order for the piston to remain in static equilibrium, the external forces and moments acting on the piston have to be balanced by the fluid pressure generated in the gap domain. A similar process is adopted for resolving the net effect of the fluid forces into two forces F_{s1} F_{s2} (as shown in Figure 20) by equating forces acting in y direction and balancing the moment about point A.

$$F_{s1} + F_{s2} = \iint_{x_A\ 0}^{x_A + l_{gap}\ 2\pi r_p} -(p + p_c) sin\phi dx dy \ ; y = r_p sin\phi \tag{3.18}$$

$$F_{s2}.l_{gap} - \int_{x_A}^{x_A+l_{gap}} \int_{0}^{2\pi r_p} -(p+p_c)x\sin\phi dxdy - \iint r_p \sin\phi dF_{visc} = 0 \qquad (3.19)$$

where, dF_{visc} represents the viscous force acting on the boundary element of piston.

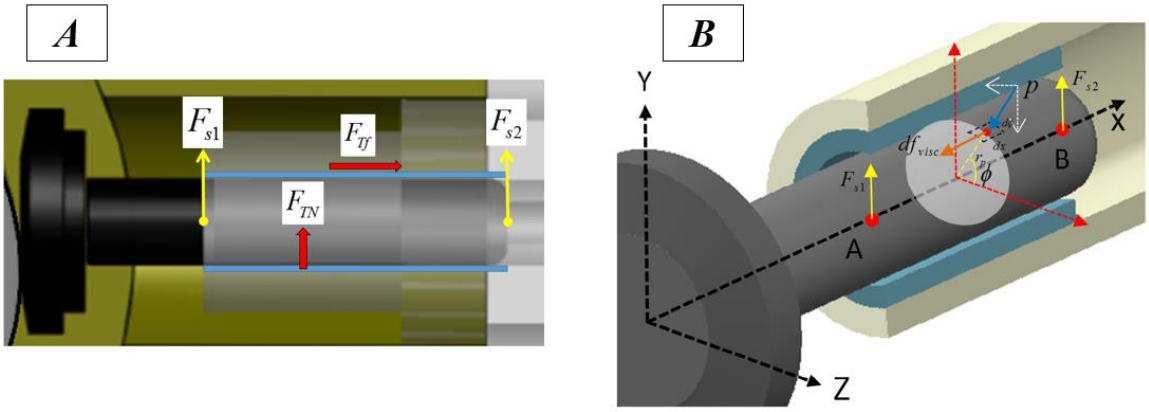

Figure 20: (A) Resolved fluid forces acting on the piston, (B) Resolution of the viscous friction forces and the reaction force normal to the piston surface all around its circumference throughout the gap length.

In order to ensure the stability of the computational procedure, when the gap heights go below a minimum point ($h_{min} = 0.2\,\mu m$), a virtual contact pressure p_c is applied to ensure that the fluid is able to support the loads occurring at these minimum fluid film locations. The presence of this contact pressure under steady state equilibrium conditions tells of a mixed lubrication regime occurring at certain locations in the piston/cylinder interface during pump operation. To evaluate this contact load, the strain due to elastic deformation caused by solid contact is defined as:

$$\epsilon_{el} = \begin{cases} 0 & when\ h > h_{min} \\ \dfrac{h_{min} - h}{2r_p} & when\ h < h_{min} \end{cases} \qquad (3.20)$$

When the gap heights go below h_{min}, the virtual contact pressure p_c is applied to simulate the effect of a possible solid contact between the piston and cylinder surface. The contact pressure is evaluated as:

$$p_c = \epsilon_{el} E_p \tag{3.21}$$

where, E_p is the Young's modulus of the piston.

Once the external and fluid forces have been resolved, the equation of force balance of piston in y direction can be written as:

$$F_{e1} + F_{e2} + F_{s1} + F_{s2} = 0 \tag{3.22}$$

Equation (3.22) is used for ensuring the force-balance condition is satisfied once the pressure field in the gap domain has been computed. The solution algorithm for the overall computational procedure for the FSI model is explained in detail in the next section.

3.2.6 Coupled Fluid Structure Interaction – Force Balance Solution Algorithm

The numerical scheme implemented for the piston/cylinder interface FSI model is shown in Figure 21.

Starting with an initial guess for the piston eccentricity (tilt, the fluid pressure in the gap domain is solved using the Reynolds equation and is then used to calculate deformation in the piston and cylinder faces. This deformation changes the film thicknesses present in the gap and this loop continues until the pressure distribution in the gap achieve convergence. The force balance condition for the piston is evaluated until equilibrium is reached. Subsequently, the squeeze velocities of the piston are integrated to obtain the new instantaneous gap film thickness values. This procedure is carried out for different time steps in the mesh until an overall convergence in film thickness is observed. Further details of the FSI algorithm for the piston-cylinder interface can be found in [6].

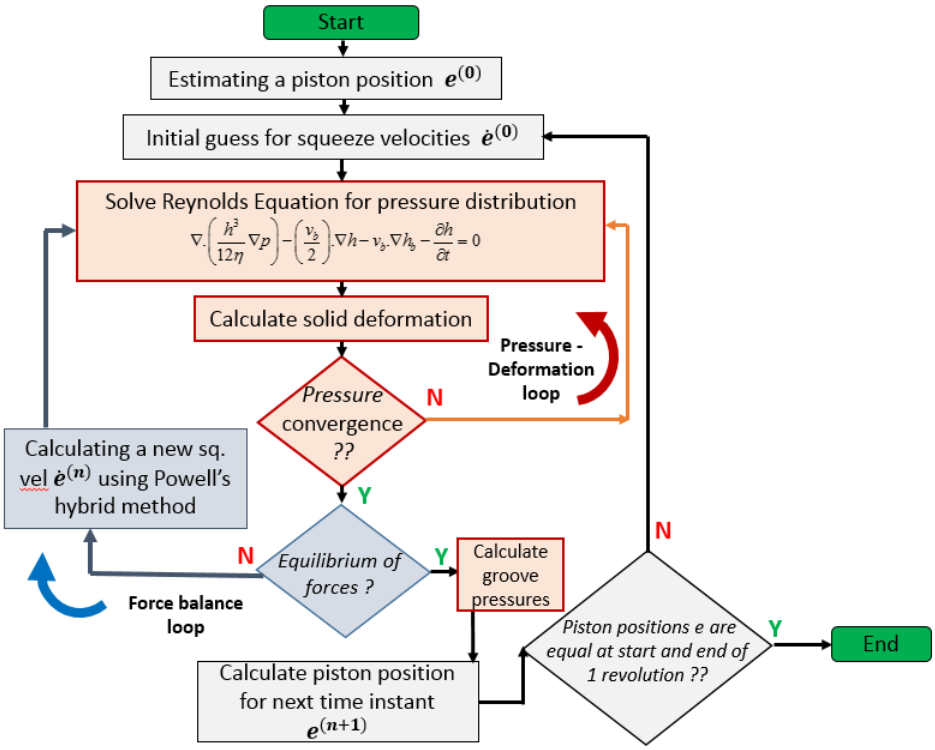

Figure 21: Numerical scheme implemented for the piston/cylinder FSI-EHD full film model.

3.2.7 Motivation for Studying Mixed Lubrication in Piston/Cylinder Interface

The piston/cylinder lubricating interface for the reference pump considered in this analysis has been studied in the past [6, 52]. As mentioned before, the key assumption made in the development of the FSI model is that the load would be entirely supported by the fluid film present in the piston/cylinder gap during pump operation.

In the CAD drawings of the reference pump considered, the nominal average clearance between the piston and cylinder is found to be 8 μm. Due to the extremely high pressures ($700 - 2500$ bar) generated within the displacement chambers, it can be seen from the force balance of the piston that the reaction force from the cam is also of this high order of magnitude. Since the contact point of application for this reaction force varies during the shaft's rotation, a considerably large moment is generated on the piston, thus causing a micro-motion. This is further enhanced by the side force (friction) acting between the cam and each piston (in Figure 19). Therefore, a breakdown of the fluid film can be

expected in regions of extremely low film thickness ($< 2\ \mu m$) that may occur due to the micro-motion of the piston (Figure 22). In such regions, the lubricant is unable to fully support the load in the y direction, leading to the possibility of the loads being shared by the fluid film as well as surface asperities.

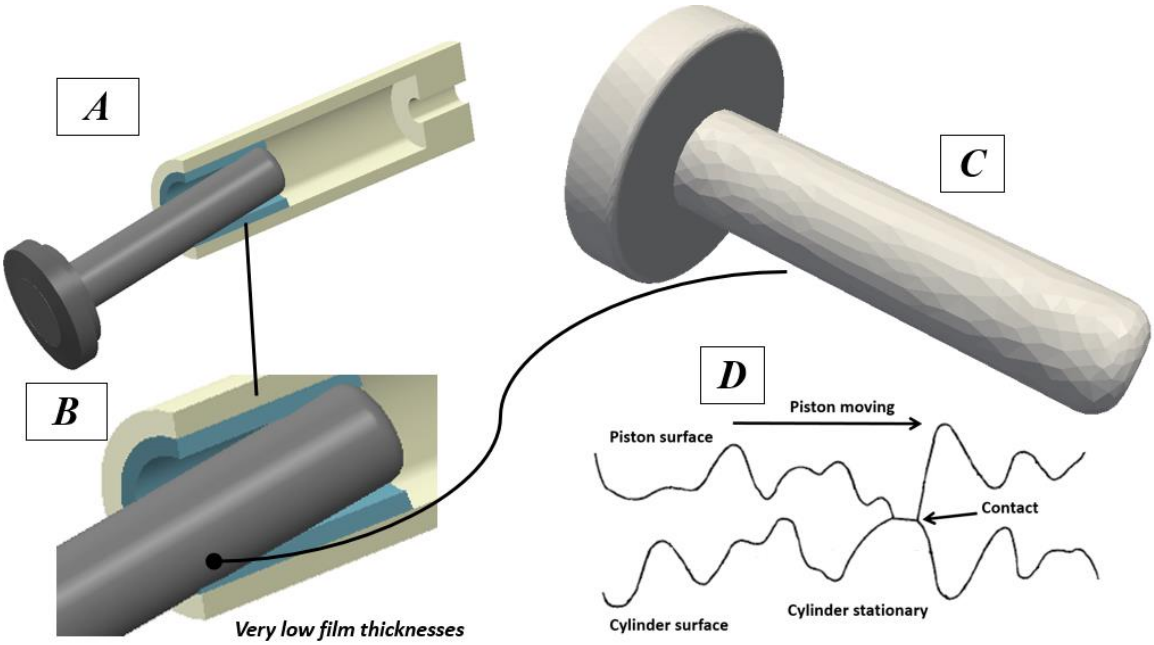

Figure 22: (A) Tilting of piston leading to (B) (zoomed in) region of possible contact where (C) surface roughness characteristics become important to consider as seen in (D) where there is asperity contact when the gap heights are of the order of the roughness.

Another motivation for exploring the aspect of mixed lubrication at this interface is the effect that the positioning of circumferential piston grooves has on the piston tilt and load balance. The aspect of mixed lubrication aiding in achieving a better balance for the piston as well as an analysis of the lubricating performance of the pump will be explored in greater detail in Chapter 6.

The following section describes the novel Mixed FSI-EHD (Fluid Structure Interaction – Elastohydrodynamic) model developed to analyze the effect of surface roughness and mixed lubrication in radial piston machines.

3.3 Mixed FSI-EHD Model for the Piston/Cylinder Interface

In addition to the submodels present in the FSI model described in Section 3.2, there are a few additional features that have to be incorporated in order to assess the effect of mixed lubrication in the piston/cylinder gap. A brief description of the solvers used in this model is provided below:

Fluid Flow Solver: Solves the Average Flow Reynolds equation for the fluid pressure.

Elastic Deformation Solver: Solves the elasticity equations for the solids, i.e. the piston and the cylinder, to determine the elastic deformation of the surfaces due to a build-up of fluid pressure within the gap. This remains the same as before and has not been detailed in the upcoming sections.

Asperity Contact Solver: Solves for the load supported by the elasto-plastically deformed surface asperities in regions of low film thicknesses.

Force Balance Solver: Ensures the balance of the forces and moments acting on the piston by including the forces from asperity contact.

These solvers and the exchange of information flow between them are highlighted in Figure 23.

The various submodels developed to accurately model the effect of mixed lubrication are described in detail in the following sections.

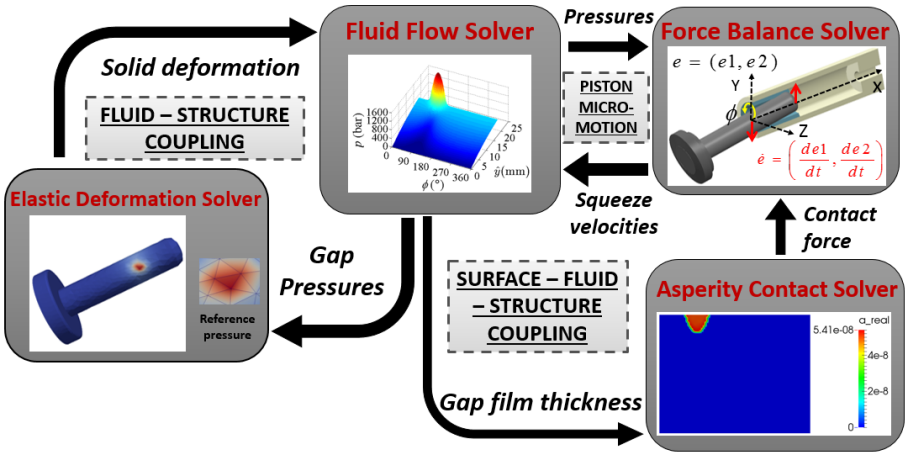

Figure 23: Schematic of the Mixed FSI-EHD solver for the piston/cylinder interface.

3.3.1 Assumptions for Considering Surface Roughness Effects

Modeling the effect of mixed lubrication in lubricated machine components can be approached in different ways. The most notable feature in mixed lubrication models developed in the vast literature available on this topic, is addressing the effect of surface roughness. For the present purposes of modeling the surface roughness on the piston and cylinder surfaces in a generalized manner, a stochastic modeling approach is assumed. There are many advantages to adopting this type of modeling technique which are detailed as follows:

- It provides a statistical representation of surface features (such as roughness) for the piston and cylinder which can be extended to newer designs formulated through simulation without the need for physical measurements.
- This technique allows to continue following the assumption made in unwrapping of the 3D gap film to be analyzed as a 2D mesh.
- It is a relatively simplified approach which can easily be integrated with the present FSI gap model for the piston-cylinder interface.
- This approach has been implemented successfully in conformal contact interfaces in the past [23, 34, 35].

By adopting this strategy to model the surface features, the following assumptions are made before proceeding to the details of the submodels:

- A Gaussian distribution of the surface asperity heights is assumed. This is a valid consideration since most surface finishing processes ultimately create Gaussian distributions (59).
- The surface is isotropic in nature, i.e. the properties of the surface along both the directions of the plane are identical.
- A combined surface roughness parameter R_q is used to characterize the surfaces. This can be found as follows:

$$R_q = \sqrt{{R_{q1}}^2 + {R_{q2}}^2} \tag{3.23}$$

where, R_q is the standard deviation of the composite roughness of the two surfaces considered whose individual roughness standard deviations are R_{q1} and R_{q2} respectively.

3.3.2 Fluid Flow Solver

The flow is a mixed lubrication regime is characterized by the Average Flow Reynolds Equation given by Patir and Cheng (1978). This is a simplified approach to model the effects of surface roughness on partially lubricated contacts. The equation describes the dependence of the pressure generated by the lubricant on the film thickness present when the two bounded surfaces are rough. The effect of surface roughness on the flow comes into view when the film thickness regimes occur in the same order of magnitude as the roughness. When this happens, the average pressure between the surface and the lubricant is predicted by the average flow Reynolds equation [29] shown in Equation (3.24).

$$\nabla.\left(\phi_x \frac{\rho h^3}{12\eta}\nabla p\right) - \phi_c\left(\frac{\rho \boldsymbol{V}_b}{2}\right).\nabla h - \phi_c \rho \boldsymbol{V}_b.\nabla h_b - \phi_c \rho \frac{\partial h}{\partial t} + R_q \frac{\boldsymbol{V}_b}{2}\frac{\partial \phi_s}{\partial x} = 0 \tag{3.24}$$

Here, ϕ_x is the pressure flow factor in the x direction, ϕ_c is the contact factor and ϕ_s is the shear flow factor. The pressure flow factors in x and y directions are found by examining the ratio of flow in between two rough surfaces to that of two smooth surfaces. The surfaces are assumed to be isotropic, i.e. $\phi_x = \phi_y$. The last term in the equation represents the additional flow transport due to sliding when rough surfaces are considered. Also, p here represents the average or mean pressure as mentioned earlier.

The fluid film thickness is defined as the average gap h, expressed as the sum of the geometrical compliance h_g (as found in Section 3.2.1), the average asperity heights present on the piston and cylinder surfaces, and the deformations caused by the elastohydrodynamic and asperity contact pressures.

By considering an “average flow”, the expressions for leakages and shear stresses generated at the piston/cylinder interface are now also modified.

The expression for the leakages is modeled using Equation (3.25). New factors (shown in Appendix B) are included in order to account for the roughness of the surfaces.

$$Q_{leak} = \int_0^{2\pi r_p} \int_{h_b}^{h_t} \left[\frac{-h^3}{12\eta} \phi_x \frac{\partial p}{\partial x} + \phi_c \frac{h v_b}{2} + \frac{R_q v_b}{2} \phi_s \right] . dx \tag{3.25}$$

The shear stress acting on the surface of the piston is evaluated for each cell using Equation (3.26) and summed across the piston surface. The power loss due to viscous friction is evaluated in the same manner as done for full film lubrication. Additional correctional shear stress factors are introduced in the same manner as done previously.

$$(\tau_{zy})_{z=h_b} = -\phi_{fp} . \frac{h}{2} . \frac{\partial p}{\partial x} - \frac{\eta(\phi_f - \phi_{fs}) v_b}{h} \tag{3.26}$$

Equations (3.24) – (3.26) are developed using the same methodology as that of the modified Reynolds equation in order to account for the ability of the piston and cylinder surfaces to deform. A complete derivation can be found in Appendix A.

The next step is to evaluate each of these new flow factors introduced by virtue of considering mixed lubrication. Considering the assumptions of isotropic surfaces with a Gaussian distribution of surface roughness, Appendix B shows the analytical expressions for these factors found in literature, including the ones to be used to estimate the viscous friction power loss and the leakage terms.

3.3.3 Asperity Contact Solver

The presence of surface asperity contact is the major feature of any mixed lubrication model. Surface roughness influences lubricant flows when the gap heights reach the order of asperities. The contact pressures generated contribute towards load support in the gap and deform the surfaces in addition to elastic deformations due to fluid pressure loading. Asperity contact and sliding also generate heat.

The roughness effect is characterized in two stages in this model:

- The local event of an asperity contact is modeled based on a contact model, yielding a contact pressure distribution as a function of the local surface separation.

- The effect of this asperity contact on the hydrodynamic pressure, deformations and heat transfer can be studied.

Since isothermal conditions are being assumed throughout this analysis, the effect of heat generation and transfer due to asperities is neglected. This is acceptable considering the fact that full film lubrication is presumed to exist for the majority of the pumping cycle, as the alternative would imply a short life for the pump due to extensive wearing of the surfaces.

The rough surface contact model developed by Lee and Ren (1996) is based on a Boussinesq formulation which takes into account the effects of elastic and plastic deformations of asperities, as well as the influence of contact of one asperity on its neighboring asperities. It is this contact model that has been incorporated in this analysis. The model [30] has been widely employed in analyzing the asperity contact effects in mixed lubrication for conformal surfaces [23, 34, 35].

Before describing the asperity contact model, it is important to define certain non-dimensional parameters employed in the equations to follow.

$$\overline{P_c} = \frac{p_{asp}}{C_P}, \qquad C_p = \frac{\pi E^* R_q}{2\lambda_y^*}, \qquad H_Y = \frac{2H\lambda_y^*}{\pi E^* \sigma}, \qquad E' = \frac{2}{\left(\frac{1-{\nu_a}^2}{E_a} + \frac{1-{\nu_b}^2}{E_b}\right)} \tag{3.27}$$

where $\overline{P_c}$ is the non-dimensional contact pressure, P_c is the contact pressure at each cell, H_Y is the non-dimensional material hardness, H is the material hardness, λ_y^* is the auto-correlation length, σ is the yield strength of the material, E^* is the effective Young's modulus, and ν_a and ν_b are the Poisson's ratios of the two surfaces in contact.

The contact calculation shown here assumes a dependence only on the surface topography (isotropic surface considered here) as well as the material properties (such as material hardness, Young's modulus, etc.). Also, the contact equations are only valid when the average gap heights estimated are less than 1.5 times the surface roughness parameter R_q.

From Lee and Ren (1996), the contact pressure is related to the average gap by the following relation:

$$\frac{h}{R_q} = \exp\left(\sum_{i=0}^{4} (\overrightarrow{\gamma_G}^T [G_i] \overrightarrow{H_Y}) \overline{P_c}^i\right) \tag{3.28}$$

Here, $\overline{P_c}$ is the non-dimensional contact pressure which is the only unknown in Equation (3.27), and is evaluated using the secant method for each cell.

For the above evaluated contact pressure, a corresponding real area of contact between the asperities can be solved from the following equation:

$$\frac{a_r}{a_{nom}} = \left(\sum_{i=0}^{4} (\overrightarrow{\gamma_A}^T [A_i] \overrightarrow{H_Y}) \overline{P_c}^i\right) \tag{3.29}$$

Here, a_r is the real area of contact between the asperities (by taking into account elastic-plastic deformations of the asperities) that is calculated for each cell where contact is predicted and a_{nom} is the nominal area of contact which is taken to be the total area of each cell without assuming any deformation effects. In Equations (3.28) and (3.29), $\overrightarrow{\gamma_A}^T = [1, \gamma, \gamma^2, \gamma^3]$, $\overrightarrow{\gamma_G}^T = [1, \gamma^{-1}, \gamma^{-2}, \gamma^{-3}]$, $\overrightarrow{H_Y}^T = \left[1, {H_Y}^{-1}, {H_Y}^{-2}, {H_Y}^{-3}\right]$, and $[A_i]$ and $[G_i]$ are parametric matrices given by Lee and Ren (1996).

Once the contact pressures have been evaluated, they must be incorporated in the force balance solver for the piston.

3.3.4 Force Balance Solver

The crucial aspect of modeling the mixed lubrication regime is that the asperities share the load support in regions where the fluid film begins to break down. As depicted in Figure 24, the contact force behaves in a similar manner to the correction force term used to ensure solver stability in the full film FSI model (Equations (3.18) and (3.19)). The equations for load balance in the y direction remain the same as Equations (3.18) and (3.19), except that the correction pressure term p_c is replaced by the asperity contact pressure term p_{asp}.

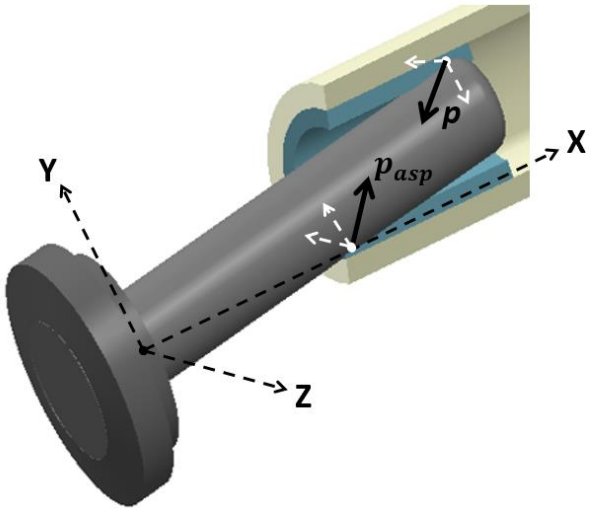

Figure 24: Illustration of the fluid and asperity contact forces involved in load support during mixed lubrication conditions.

Essentially,

$$W_y = W_f + W_{asp} \tag{3.30}$$

where, W_y is the total load acting on the piston in the y direction and W_f and W_{asp} are the loads shared by the fluid film and the asperities respectively.

3.3.5 Solution Algorithm

The solution algorithm for the mixed FSI-EHD model is described in Figure 25.

The solution begins much the same as the full film FSI model, where the initial piston position and squeeze velocities are guessed. The average gap heights across the interface are evaluated and the flow factor terms used in the average Reynolds equation are calculated. The average Reynolds equation for the fluid pressure is solved and these pressures are used to evaluate the elastic deformation of the piston and cylinder surfaces. Once the pressure-deformation loop reaches convergence, the asperity contact model for the contact pressure is solved if regions of very low gap heights are predicted. The contact pressure load and the fluid pressures are used in the force balance equations of the piston to evaluate the squeeze velocities of the piston at that particular time instant, until this outer loop achieves convergence. The converged value of the squeeze velocity

is used calculate the eccentric position of the piston for the next time instant through a numerical integration of the squeeze velocity over a time step by using the Euler-explicit method.

$$\boldsymbol{e}^{(n+1)} = \boldsymbol{e}^{(n)} + \dot{e}^{n}(t^{n+1} - t^{n}) \tag{3.31}$$

When the calculated positions of the piston at the beginning and end of one shaft revolution are the same, a steady state solution is said to be achieved.

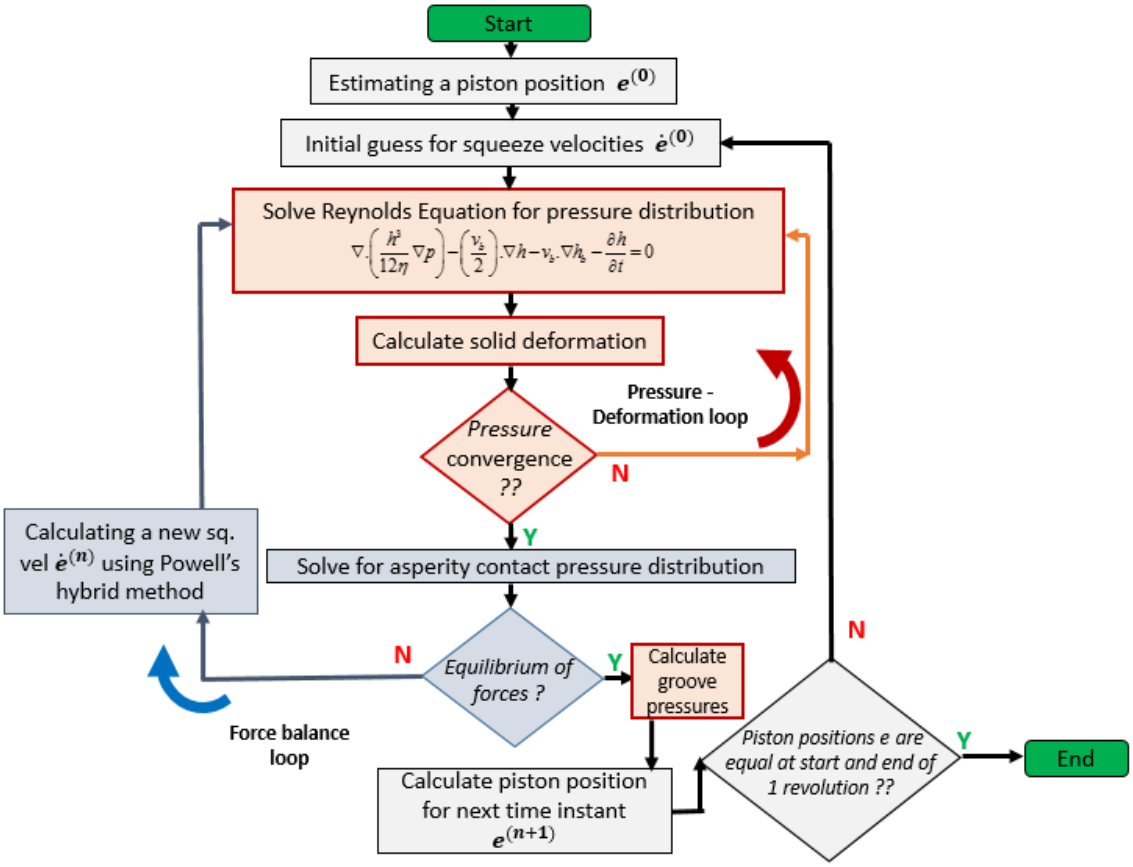

Figure 25: Numerical solution algorithm for the Mixed FSI-EHD model for the piston/cylinder interface.

3.4 Line EHL Numerical Model for Friction Evaluation at the Cam/Piston Interface

This section details the features of the numerical model developed in [6] used to evaluate the friction coefficient at each time step present at the cam/piston interface. A significant addition to the model's capabilities introduced in this work includes the ability to

evaluate the power losses due to viscous friction occurring at the cam/piston interface. Additionally, this model has been applied in conjunction with the experimental technique developed (presented later in Chapter 4) to evaluate the variation of the friction coefficient at the cam/piston interface for the reference machine.

As mentioned in Section 3.2.5, the friction force exerted on the pistons at the cam/piston contact interface is the only side force acting on the piston. This force, along with the moment generated due to the contact load from the cam cause the piston to tilt within the cylinder, ultimately resulting in a radial micro-motion with the associated hydrodynamic effects. This is illustrated through Figure 26.

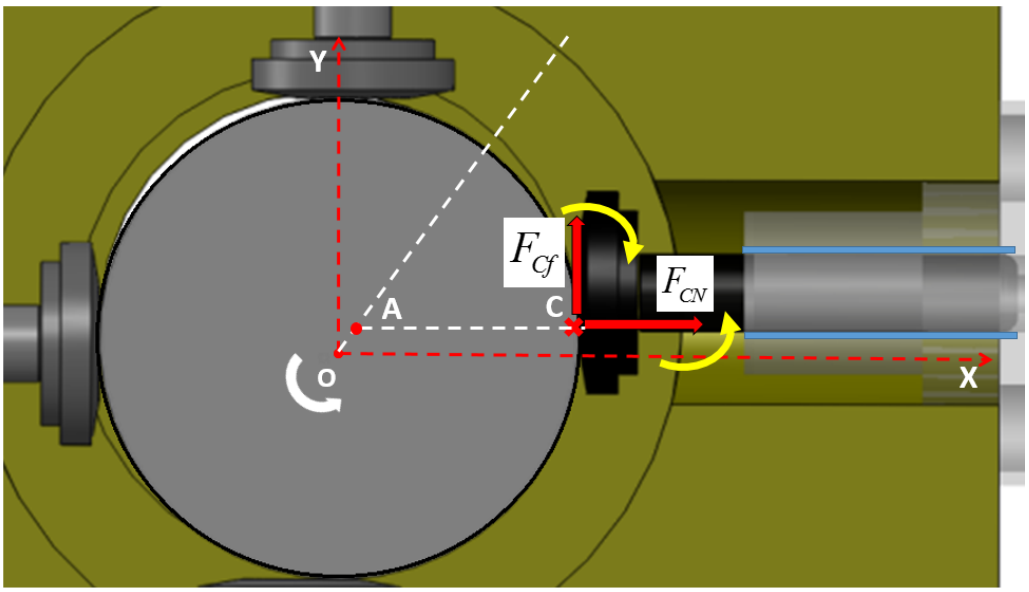

Figure 26: The two causes of piston tilt: friction between the cam and piston; and the moment from the normal reaction of the cam on the piston.

3.4.1 Motivation for the Study of the Cam/Piston Interface

There are many compelling reasons that motivate the need for an in-depth analysis of the cam-piston interface. An efficient design of this interface requires the friction between each cam and piston to be minimized, so that there is reduced wear at the contacting surfaces during pump operation. Also, the lubricant present between the contact region of the cam and each piston shears as the shaft rotates. This results in some non-negligible viscous shear losses being present, which impacts the overall pump performance as well

as the efficiency of the unit. Another reason to study this interface, and perhaps the most important, is the variation of the friction force acting between the cam and each piston due to the dynamic loading present at this contact during each shaft revolution. Since this friction force is the only side load acting on the pistons, it is the key component in causing each piston's radial micro-motion within its displacement chamber during pump operation.

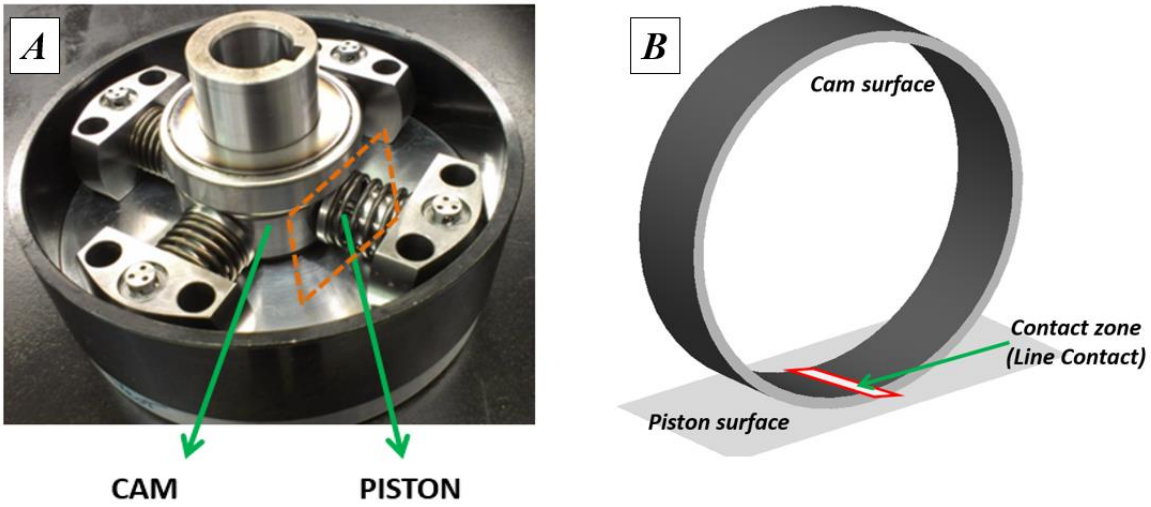

Figure 27: (A) Cam/Piston interface on the reference pump and (B) Illustration of the cam and piston surfaces causing a line contact.

During actual pump operation, the friction coefficient is strongly dependent on the lubricant flow conditions in the cam/piston interface and on the relative velocities between the contact surfaces. A dominating sliding friction component of the friction between the cam and piston would mean continuous wear of the mating surfaces. By calculating the instantaneous magnitude of the friction coefficient and the direction of the friction force acting on each piston, it is expected to achieve a physically accurate prediction of the piston micro-motion, and consequently, a more precise evaluation of the piston/cylinder gap flow. Hence, a careful analysis of the cam/piston interface permits the study of the dynamic piston motion and leads to more accurate predictions of the leakages and power losses through the piston/cylinder gap.

The geometry of the contact region between the cam and piston is equivalent to a line contact between a cylinder and a plane as shown in Figure 27. The following sub-sections detail out the complete procedure used in the numerical model for the prediction of the friction coefficient at the cam/piston interface under full film lubricating conditions.

3.4.2 Governing Equations

The lubricant flow through the line contact described by the cam/piston interface is governed by the 1-D Reynolds equation [60] stated as follows:

$$\frac{d}{dx}\left(\frac{\rho h^3}{12\eta}\frac{dp}{dx}\right) = u_e \frac{d(\rho h)}{dx} \tag{3.32}$$

where, the coordinate x is defined in Figure 28, h is the film thickness, μ is the fluid viscosity, ρ is the fluid density and u_e is the entrainment velocity of the fluid into the contact region. Isothermal conditions are assumed throughout this study. The variation of the film thickness existing in the 1-D lubricating domain can be defined as:

$$h(x) = h_0 + S(x) + \delta(x) \tag{3.33}$$

where, h_0 = constant, $S(x)$ = separation due to the geometry of undeformed solids, $\delta(x)$ = elastic deformation of both the solids (cam and piston).

The geometric separation (assuming a parabolic approximation of the cylinder-plane contact) is given by $S(x) = \frac{x^2}{2R_x}$.

Since the contact region between the cam and piston is small, and the fact that very high loads exist at this interface, there is a significant amount of elastic deformation of the two bodies comprising this contact interface. This deformation can be evaluated as follows:

$$\delta = -\frac{2}{\pi E'}\int_{x_{min}}^{x_{max}} p \cdot ln(x - x')^2 dx \tag{3.34}$$

where, x is the point on the 1-D grid where the deformation is being evaluated, and p is a function of x'varying from x_{min} to x_{max}.

At steady state (assuming that the load is supported completely by the fluid film), the pressure generated within the fluid film is sufficient to bear the contact load at the interface, thus providing the following force-balance condition:

$$w' = \int p dx \tag{3.35}$$

The dependence of density on pressure is modeled using the Dowson and Higginson relation [61]. The Barus viscosity expression [62] is used in order to model the variation of the viscosity with pressure in the fluid film at this interface. This is a crucial factor in modeling the line contact at this interface, since the viscosity of lubricant increases drastically while entering the contact zone.

$$\rho = \rho_0 (1 + \frac{0.6p}{1 + 1.7p}) \tag{3.36}$$

$$\eta = \eta_0 e^{\alpha_p p} \tag{3.37}$$

Using the non-dimensional parameters (defined in the nomenclature and in [6]), Equation (3.33) can be rewritten in the following form:

$$\frac{d}{dX}\left(\xi \frac{d\bar{P}}{dX}\right) - \frac{d(\bar{\rho}H)}{dX} = 0 \tag{3.38}$$

where, $\xi = \frac{\bar{\rho}H^3}{\bar{\eta}\lambda}$ and $\lambda = \frac{3U_e}{4}\left(\frac{\pi}{W'}\right)^2$.

The dimensionless film thickness equation can be written as:

$$H(X) = H_0 + \frac{X^2}{2} - \frac{1}{\pi}\int_{X_a}^{X_b} \bar{P}(X) ln\,|X - X'| dX \tag{3.39}$$

3.4.3 Discretization of the Lubricating Gap Domain

Equations (3.38) and (3.39) are discretized on a uniform 1D grid along the contact domain whose length ranges from X_{min} to X_{max} (Figure 28).

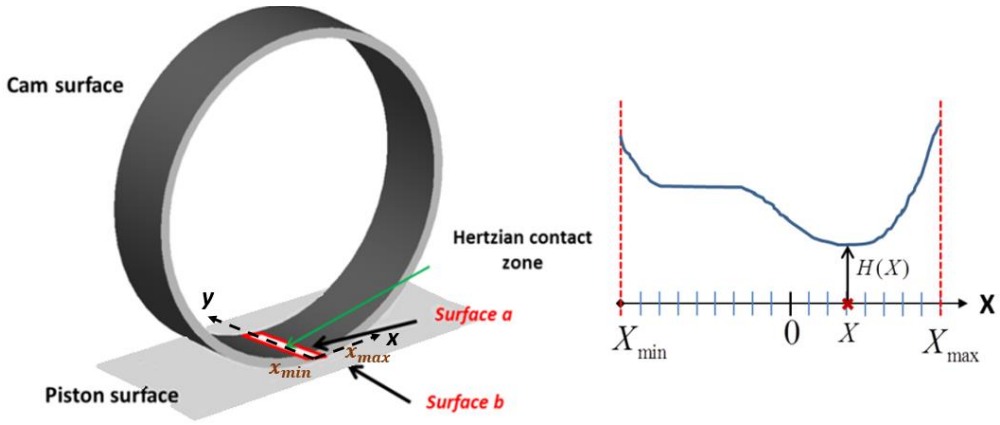

Figure 28: Lubricating gap domain discretized with respect to the non-dimensional x-coordinate in the line contact.

Using a second order central discretization for the Poiseuille term and a first order upstream discretization for the wedge term, the approximation of the Reynolds equation at node i can be written as:

$$\frac{(\xi_{i-\frac{1}{2}}\bar{P}_{i-1} - \left(\xi_{i-\frac{1}{2}} + \xi_{i+\frac{1}{2}}\right)\bar{P}_i + \xi_{i+\frac{1}{2}}\bar{P}_{i+1})}{(\Delta X)^2} - \frac{(\bar{\rho}_i H_i - \overline{\rho_{i-1}} H_{i-1})}{\Delta X} = 0 \tag{3.40}$$

The discretized film thickness equation reads as:

$$H_i = H_0 + \frac{{X_i}^2}{2} - \frac{1}{\pi}\sum_{j=1}^{n} K_{ij}\bar{P}_j \tag{3.41}$$

where K_{ij} are the associated influence coefficients used that are defined as follows:

$$\begin{aligned} K_{ij} = &\left(i - j + \frac{1}{2}\right)\Delta X\left(\ln(\left|i - j + \frac{1}{2}\right|\Delta X) - 1\right) \\ &- \left(i - j - \frac{1}{2}\right)\Delta X\left(\ln\left(\left|i - j - \frac{1}{2}\right|\Delta X\right) - 1\right) \end{aligned} \tag{3.42}$$

The dimensionless force balance equation reads after discretization:

$$\Delta X \sum_{j=1}^{n-1} \frac{\bar{P}_j + \bar{P}_{j+1}}{2} = \frac{\pi}{2} \tag{3.43}$$

3.4.4 Non-Newtonian Fluid Behavior

One of the primary factors influencing the behavior of the friction in the interface of a line contact is the sliding motion existing between the two surfaces. While in ideal cases, the two surfaces in contact exhibit a purely rolling motion at the interface, real-life scenarios can involve large sliding velocities associated with the fluid entering the contact zone. This can result in very high shear stresses being present, which ultimately requires the fluid to not be treated as Newtonian in nature. Since the radial piston pump can have large variations of rolling and sliding velocities at the cam/piston interface, a versatile line EHL capable of generating accurate solutions across all conditions is required. A simplified non-Newtonian model [63] has been incorporated in this study, wherein if the Newtonian shear stress exceeds a limiting shear stress, it is saturated [as shown in Figure 29]. This allows for the fluid to be considered as Newtonian except when the shear stress reaches the value of the shear strength, at which point slipping can occur, and so the shear stress is saturated. Details of the Non-Newtonian model used have been shown in Appendix C, for the sake of brevity and to preserve the flow of the content.

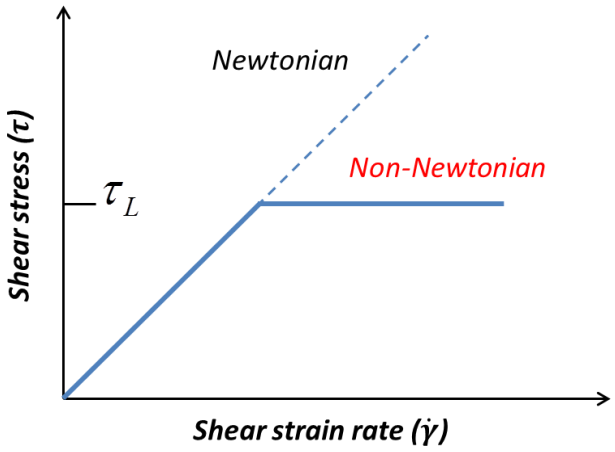

Figure 29: Non-Newtonian model used in Jacobson and Hamrock (1984) [63].

3.4.5 Numerical Solution Scheme

For the range of pump operating conditions tested (outlet pressures of 700-2500 bar, shaft speeds of 1200-1800 rpm, and contact loads of 0.1-0.6 GPa), the successive over-relaxation (SOR) scheme is stable to achieve a convergence of the pressure solution.

$$\bar{P}_i^{n+1} = \omega_{gs}\bar{\bar{P}}_i^{n+1} + \left(1 - \omega_{gs}\right)\bar{P}_i^{n} \tag{3.44}$$

The load balance condition is completed by converging the displacement coefficient H_0.

$$H_0^{n+1} = H_0^{n} + \omega_{H0}\left(\frac{\pi}{2} - \Delta X \sum_{i=1}^{n-1} \frac{\bar{P}_i + \bar{P}_{i+1}}{2}\right) \tag{3.45}$$

Here, ω_{gs}represents the under-relaxation parameter used while iterating for the pressure solution, whereas ω_{H0} represents the under-relaxation parameter used for H_0.

Figure 30 shows the flow of the solution algorithm employed to obtain a converged solution to both the gap height and the lubricant pressure at the cam/piston interface. Initial values for $\bar{P}(X)$ and H_0 are estimated, after which the Reynolds equation is solved for the pressure distribution using a Newtonian formulation as described in Equation (3.38). This intermediate pressure distribution is used to evaluate the shear stresses acting on both the surfaces comprising the line contact, and a non-Newtonian formulation is used to modify the pressure values. Based on the new pressure distributions calculated in each iteration, the elastic deformation of the two surfaces are found, post which the change in the surface gap heights can be calculated. The new film thickness values are used to update the pressure field in the pressure-deformation loop, until both the fluid pressure and film thickness values reach convergence. Next, a check is done to see if the load supported by the pressure field predicted within the fluid film is sufficient to bear the contact loads acting at the interface. H_0 is changed in order to ensure that this is possible in the force balance loop shown. The final solution to the problem is reached when the force-balance condition is satisfied.

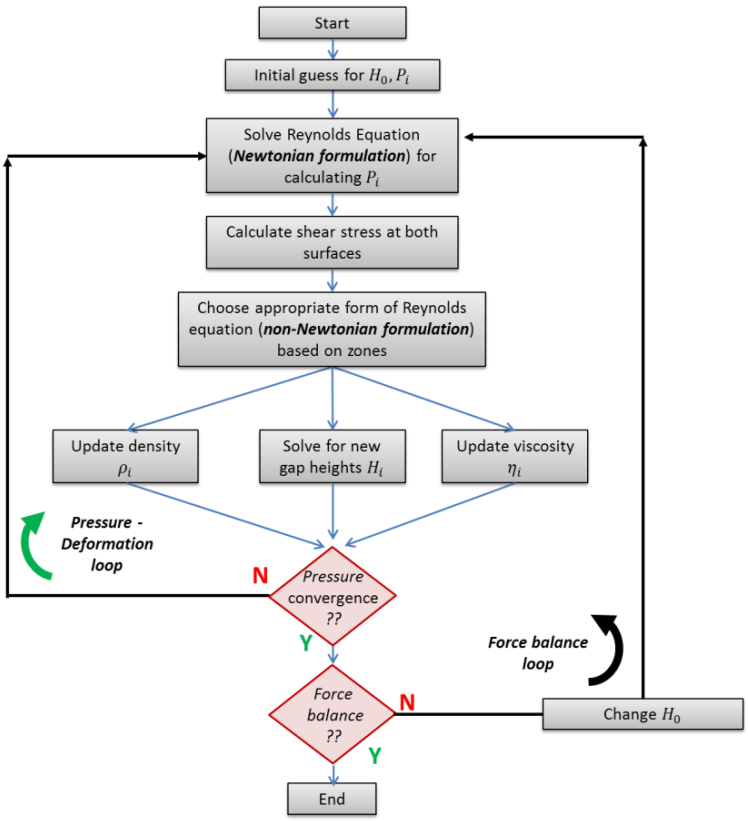

Figure 30: Solution algorithm flowchart for the EHL line contact problem.

3.4.6 Viscous Friction and Power Losses at the Interface

The solution algorithm described is capable of generating the pressure distribution and film thickness in the lubricating domain. Using these results, the traction/friction forces acting between the surfaces can be evaluated. The shear stress acting on the lower surface (representative of the piston) is defined as:

$$\tau(x) = -\underbrace{\frac{h(x)}{2}\frac{dp}{dx}}_{rolling} + \underbrace{\eta(x)\frac{(u_1 - u_2)}{h(x)}}_{sliding} \tag{3.46}$$

As depicted in the above equation, the first term represents the shear stress generated due to rolling component associated with surface velocities while the second term is representative of shear stress due to sliding velocities of the piston (u_1) and cylinder (u_2) surfaces (represented in Figure 32).

The net friction force can be obtained by integrating the shear stress along the length of contact region. Dividing this traction force by the normal contact load acting at the interface provides the friction coefficient:

$$\mu = \frac{\int_{x_{min}}^{x_{max}} \tau dx}{w_z'} \tag{3.47}$$

The power loss due to viscous friction in this interface is given by the sum of viscous friction power losses due to both the surfaces in contact.

$$P_{visc} = \int_{x_{min}}^{x_{max}} \tau_1 \frac{(u_1 - u_2)}{2} dx + \int_{x_{min}}^{x_{max}} \tau_2 \frac{(u_1 - u_2)}{2} dx \tag{3.48}$$

CHAPTER 4. INVESTIGATION OF THE CAM/PISTON INTERFACE

The previous chapter highlighted the importance of accurately modeling the variation of friction at the cam/piston interface in predicting the tilt behavior of the pistons and thereby, the power losses due to leakages and viscous friction occurring at the piston/cylinder gap. A numerical modeling methodology to estimate the friction coefficient at the cam/piston interface was described, and the resulting evaluations of the friction coefficient for a wide range of input parameters were shown. However, to model the friction at the cam/piston interface of an actual radial piston pump, it is necessary to provide suitably accurate inputs - i.e. the dynamic conditions of the contact load and cam and piston velocities - to the cam/piston numerical model.

Table 1: Input parameters for the cam/piston line EHL friction model.

Input Parameter	**Description**
W'	Dimensionless Load Parameter
U_e	Dimensionless Entrainment Velocity
SRR	Slide-to-Roll Ratio
G	Dimensionless Material Parameter

The input parameters that are required to model the friction at the cam/piston interface are shown in Table 1. While the load parameter W'can be calculated by analyzing the variation of the contact loads on the cam from each of the pistons, the determination of the velocity parameter U_e and the slide-to-roll ratio SRR are of a more challenging nature. The dimensionless material parameter G is the same throughout (steel).

4.1 Past Effort in Investigating the Friction at the Cam/Piston Lubricating Interface

In the past, two different cam/piston interface designs were analyzed using the line EHL numerical model developed [6]. These two configurations are shown in Figure 31.

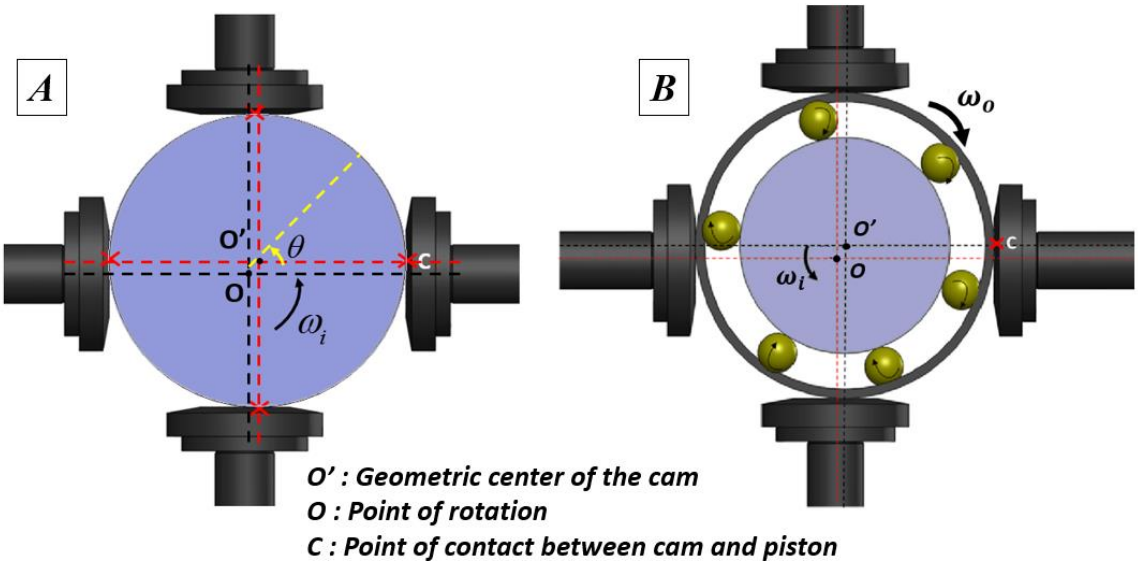

Figure 31: The two cam/piston geometrical configurations analyzed in the past [6].

In the first case, a direct contact between the eccentric cam and each piston was analyzed to study the variation of friction during an operational cycle for the reference radial piston pump. At operating conditions of 700 bar outlet pressure and a shaft speed of 1800 rpm, the results showed a significant variation in the friction coefficient (viscous friction in EHL) during the pump cycle. However, extremely low film thickness values ($< 0.05\ \mu m$) were observed indicating that there is a significant asperity contact between the cam and piston surfaces. This showed that direct cam/piston contact configuration would be insufficient to lubricate this interface and would thus, undergo wear in continued operation.

The second case analyzed was that of the reference geometry of the pump. In this design, rolling element bearings are present in between the inner eccentric shaft and a freely rotating outer race rests in contact with each of the pistons. Since the outer race is free to rotate about its center, its angular velocity is dependent on the friction forces acting between the rolling element bearings and the inner/outer races. This would require an

analysis of the bearing dynamics along with race and cage interactions which are out of the scope of this research. A simplified approach was followed in modeling this interface by assuming that the contact between the outer race and the piston with the highest instantaneous load will undergo pure rolling at each time instant. By adopting this strategy, it was observed that the entrainment speeds estimated were very low, resulting in the EHL model predicting an insufficient amount of pressure generation in the fluid film. Therefore, there is a need to evaluate the entrainment speeds present at this contact interface in order to accurately predict the friction behavior.

In this chapter, a novel experimental methodology is proposed to dynamically evaluate the surface velocities of the cam and piston at each time instant during the shaft's rotation. For this reason, a detailed analysis of the cam/piston kinematics is required to be performed.

4.2 Kinematic Analysis of the Outer Race

Before commencing on an analysis of the kinematics of the cam, it is important to define certain terminology that will be used in the subsequent stages.

Entrainment velocity (u_e): This represents the rate at which lubricant flows into the contact region between the outer race and each piston, at each instant during a single revolution of the shaft.

Sliding velocity (u_s): This represents the relative velocity between the two surfaces that are in contact, i.e. the outer race and each piston.

Slide-Roll Ratio (SRR): This is defined as the ratio of the sliding velocity to the entrainment speed.

These velocity parameters can be represented mathematically in terms of the surface velocities of the outer race and the piston as follows:

$$u_e = \frac{(u_1)_C + (u_2)_C}{2} \tag{4.1}$$

$$u_s = (u_1)_C - (u_2)_C \tag{4.2}$$

$$SRR = \frac{u_s}{2u_e} \tag{4.3}$$

where $(u_1)_C$ and $(u_2)_C$ are velocities of upper and lower surface respectively with respect to the contact point between the surfaces [64] as depicted in Figure 32.

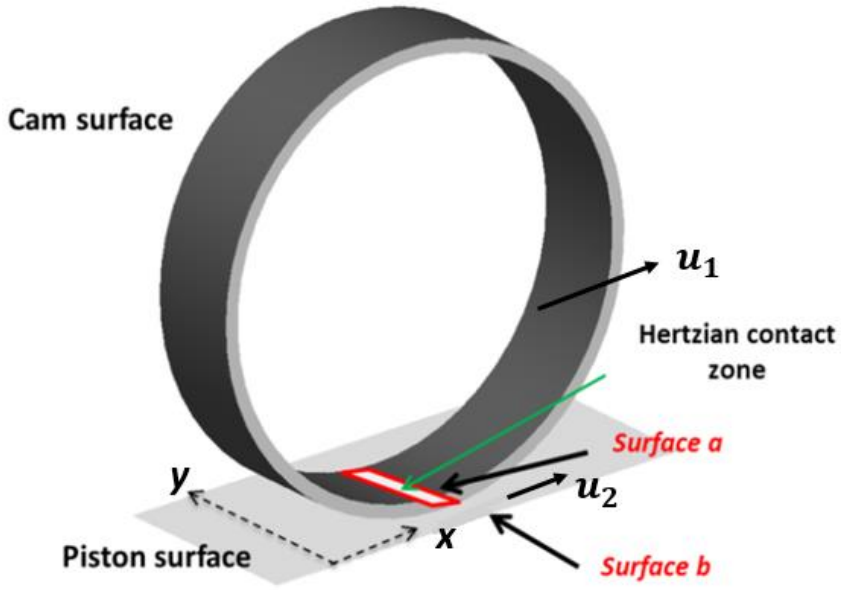

Figure 32: Illustration depicting the sliding velocities of the cam and piston surfaces.

Figure 33 (A) shows the configuration of the cam-piston contact being considered in this study, and the velocity diagram representing the motion of different components. Using these kinematic relations, the equations for the instantaneous surfaces velocities of the outer race (u_1) and piston (u_2) at the contact point C (depicted in Figure 33 (B)), when viewed from a stationary frame of reference, are defined as follows:

$$u_1 = v_y = e\omega_i cos\theta + r_o\omega_o \tag{4.4}$$

$$u_2 = 0 \tag{4.5}$$

From the definition of the entrainment and sliding velocities (u_e, u_s) as seen in Equations (4.1) and (4.2), u_1 and u_2 have to be converted to the reference frame of point C.

$$(u_1)_C = r_o\omega_o \tag{4.6}$$

$$(u_2)_C = u_C = \frac{dy_C}{dt} = -e\omega_i cos\theta \tag{4.7}$$

where, u_C is the velocity of the contact point as it changes with the shaft angle.

Substituting the above expressions in Equations (4.1), (4.2) and (4.3):

$$u_e = \frac{r_o\omega_o - e\omega_i cos\theta}{2} \tag{4.8}$$

$$u_s = |r_o\omega_o + e\omega_i cos\theta| \tag{4.9}$$

$$SRR = \frac{|r_o\omega_o + e\omega_i cos\theta|}{r_o\omega_o - e\omega_i cos\theta} \tag{4.10}$$

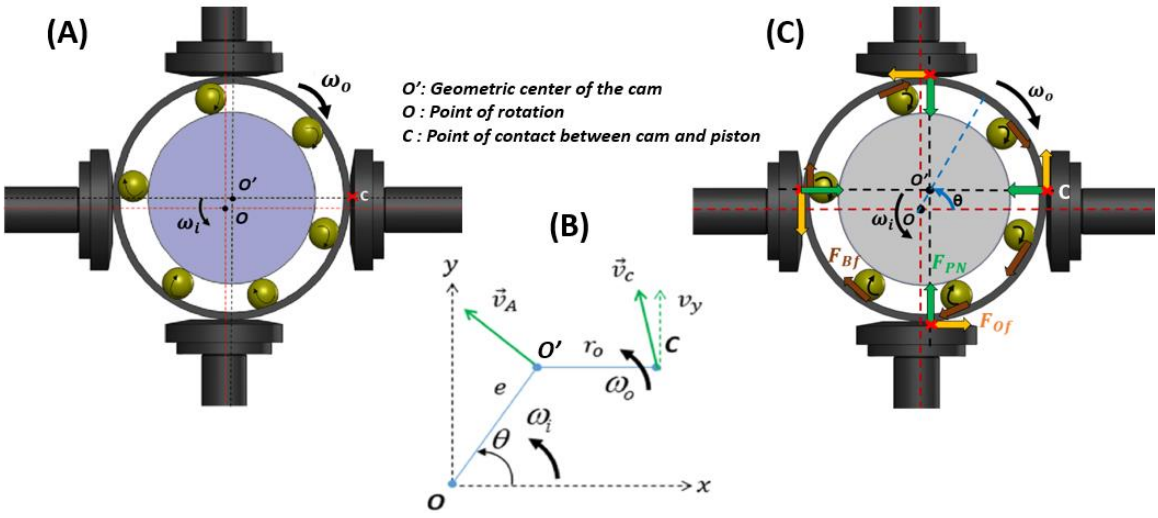

Figure 33: (A) Cam/piston interface with rolling element bearings and outer race, (B) Resolution of velocity at the contact point, (C) Force diagram of the outer race.

It can be seen from the above equations that the surface velocities are dependent on the angular velocity of the outer race (ω_o) which is an unknown. The equation of moment balance for the outer race can be written as:

$$\left\{\sum_{i=1}^{n} F_{Bf_i} + F_{Of_1} + F_{Of_2} + F_{Of_3} + F_{Of_4}\right\} x\, r = I\frac{d\omega_o}{dt} \tag{4.11}$$

where, n represents number of ball bearings, $F_{Of_{1-4}}$ are the friction forces between the outer race and each piston, r is the radius of the outer race and I is the moment of inertia of the outer race (ring) (seen in Figure 33 (C)).

The above relation shows that calculation of this angular velocity is dependent on the friction force exerted by each of the pistons that can vary with shaft rotation. Also, the complex interaction with each of the rolling element bearings would need to be determined. For this reason, an experimental measurement of the velocity of the outer race is deemed necessary to close the problem. Inferring these surface velocities from direct measurements would serve as the most accurate method of generating input parameters for the friction model. The details of the experiment conducted are described in the following section.

4.3 Experimental Study of the Instantaneous Velocity of the Outer Race

4.3.1 Experimental Setup

In this section, an experimental methodology is proposed to evaluate the surface velocities of the outer race and each piston for a single revolution of the shaft. These surface velocities are used in Equations (4.8), (4.9) and (4.10) to evaluate the input velocity parameter U_e and the slide-to-roll ratio SRR for the numerical model. Figure 34 (A) shows the test rig used to conduct this experiment. A fixed-speed electric motor (set at 1800 rpm) rotates the eccentric shaft that causes the pistons within the radial piston pump to translate within their respective displacement chambers. The reference radial piston pump itself is bolted onto the plate present above the reservoir containing the hydraulic oil. The same eccentric shaft passes through a gear pump which serves as a booster pump and supplies fluid to the radial piston pump at a higher pressure than ambient (about 15 bar). Since both pumps are encased within the reservoir, the ISO schematic representation of Figure 34 (B) illustrates how they are actually present in this test rig realized at the Maha Fluid Power Research Center of Purdue University (USA). A pressure relief valve is used to control the outlet pressure in the high pressure line.

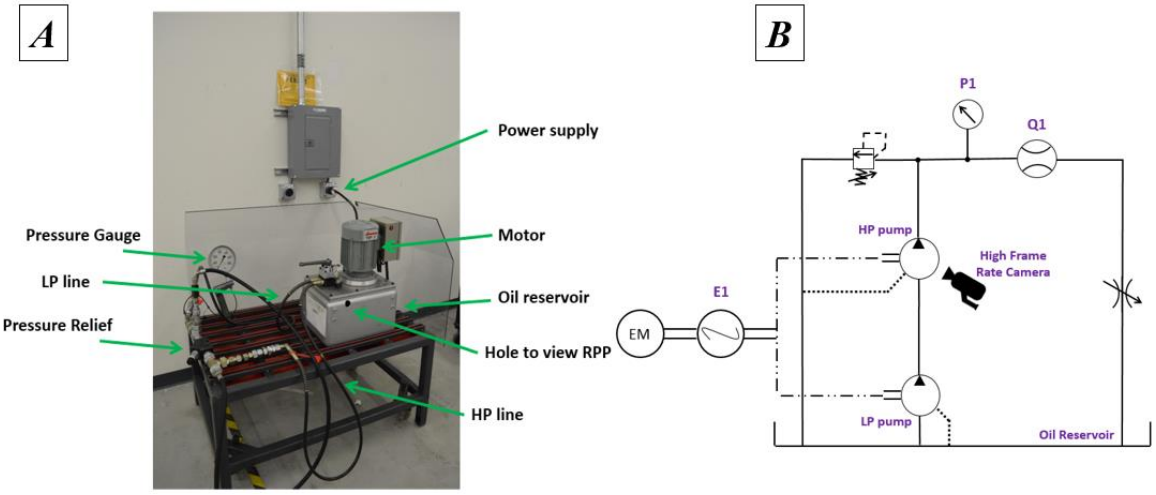

Figure 34: (A) Experimental test rig used to estimate the instantaneous angular velocity of the outer race, (B) Hydraulic circuit for the setup.

4.3.2 Proposed Methodology

In order to capture the instantaneous angular velocity of the outer race as a function of the shaft angle, an approach involving the use of a camera was tested. The outer race of the cam was painted in black throughout the circumference with equally-spaced thin white strips, as shown in Figure 35 (A). The motion of the thin white strips over one rotation of the shaft can be used to estimate the instantaneous angular velocity. To evaluate this during real time pump operation, two holes were required to be drilled – one onto the casing of the reservoir containing the hydraulic oil and the other onto the casing of the radial piston pump. A custom-made bracket attachment was fabricated in order to prevent hydraulic oil from flowing out of the hole created in the radial piston pump and obscuring the view of the paint marks from outside the test rig using the camera. This is shown in Figures 35 (B) and 35 (C), which also illustrate the viewing zone which the camera is focused on to capture the motion of the outer race.

Figure 35: (A) Painted outer race, (B) Custom bracket attachment used in the test rig setup, (C) Camera view during measurements.

Since the shaft rotates at a rate corresponding to 30 rev/s, a regular video camera which captures images at 30 frames per second (fps) is insufficient to capture the instantaneous velocity of the outer race. For this reason, a video camera was used which recorded images at the rate of 240 fps which corresponds to 8 frames being captured for a single rotation of the shaft. This allowed for 8 data points being available to analyze the instantaneous angular velocity of the outer race.

After the experiment was conducted, a post-processing methodology was used to analyze the velocity of the outer race by evaluating the position of each strip in every frame. A reference position was considered based on which the distance of each strip from this point was estimated as they entered the viewing area (seen in Figure 36 (A)). From the change in the displacements of each strip in a particular frame with respect to the previous frame, the instantaneous angular velocity could be found. The presence of multiple thin strips with known values of the distance intervals between them were helpful in judging the displacement variation of each strip in successive frames. Many such frames were analyzed and a typical set of data of the instantaneous angular velocity of the outer race starting from when the first strip entered the viewing area up to when the last strip exited the viewing area is shown in Figure 36 (A).

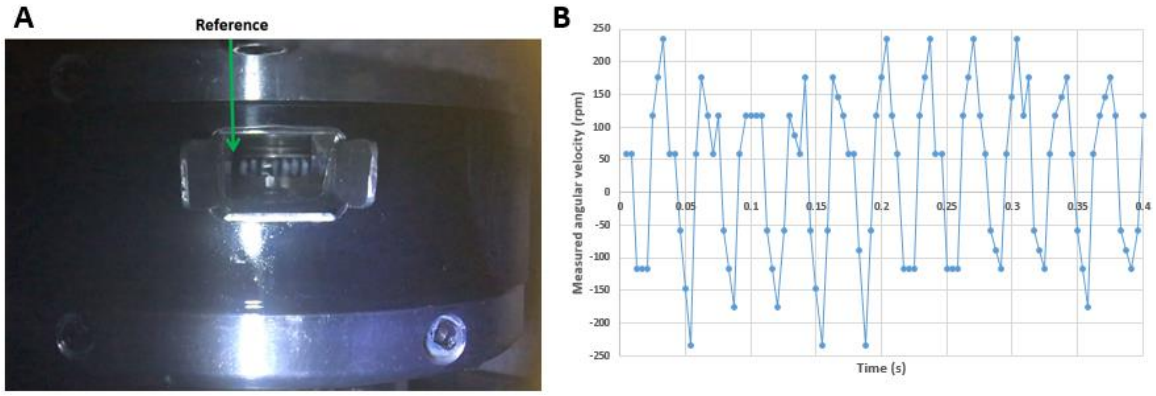

Figure 36: (A) Example of a single frame analyzed by estimating the distance of each strip from the reference location, (B) Typical set of measured data points of instantaneous angular velocities obtained over multiple shaft revolutions.

In order to obtain the instantaneous velocities of the outer race for one shaft revolution, an average of the velocities at data points separated by 8 frame intervals was taken. This allowed for evaluating the instantaneous motion of the outer race represented by 8 averaged data points for one revolution of the shaft under steady state pump operation. A cubic spline interpolation scheme was used to construct a smooth curve to obtain the instantaneous variation of the angular velocity of the outer race over one shaft revolution. Figure 37 shows the measured angular velocity of the outer race interpolated over 360^o of the shaft's rotation.

Tests were conducted for different pump operating pressures in order to understand the effect of the load present at the contact interface on the variation in angular velocity of the outer race. A sufficient range of operating pressures from 100 bar to 350 bar was considered for this study. It was found that this range of contact load did not have any perceivable effect on the average velocity of the outer race, and so, the results obtained from these experiments were used for the subsequent simulation study at any pump operating condition.

This interpolated data, however, does not take into consideration the fact that the shaft rotates eccentrically during each revolution. While evaluating the actual angular velocity of the outer race, this eccentric shift present throughout the shaft's revolution must be subtracted from the measured data in order to obtain an accurate behavior of the outer

race motion. This eccentric shift can be evaluated by considering a situation where the eccentric outer race revolves about the shaft center without any rotation about its own axis. This is illustrated in Figure 38 (A) through a representation of the motion of a circle at two instants (centers A and B), that revolves about a fixed location in space, O. The shift mentioned is the distance which is to be subtracted from the measured positional data.

Once this shift is accounted for, the actual angular velocity variation as a function of shaft angle can be plotted as shown in Figure 38 (B). This is an interpolated plot with four periods since the motion of the outer race is influenced by the four pistons present. It may be observed that the curve appears to pass through almost all 8 points obtained from the experiment.

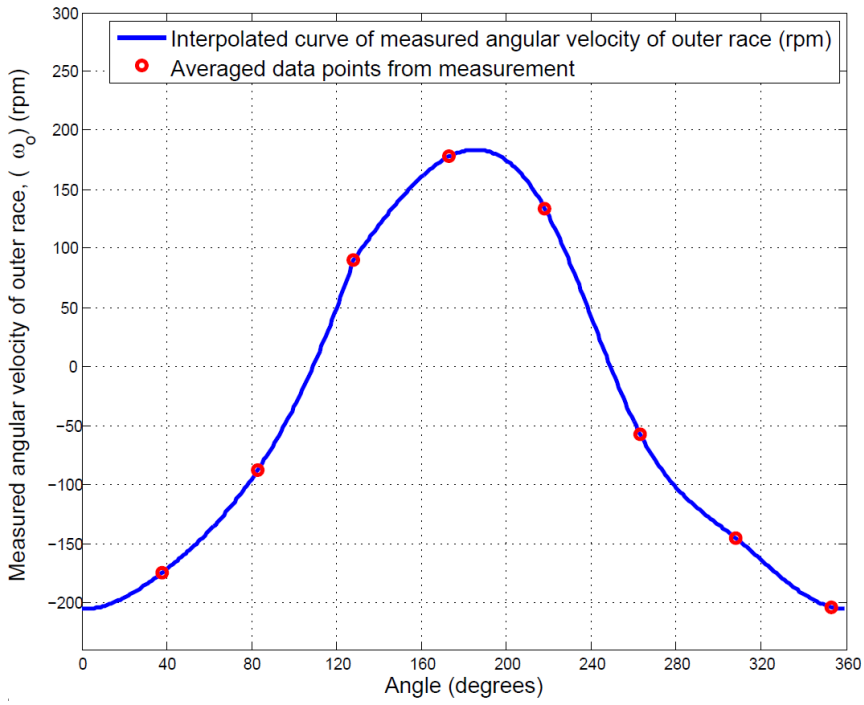

Figure 37: Curve generated from the measured velocity of the outer race through an interpolation of the measured data points over one shaft revolution.

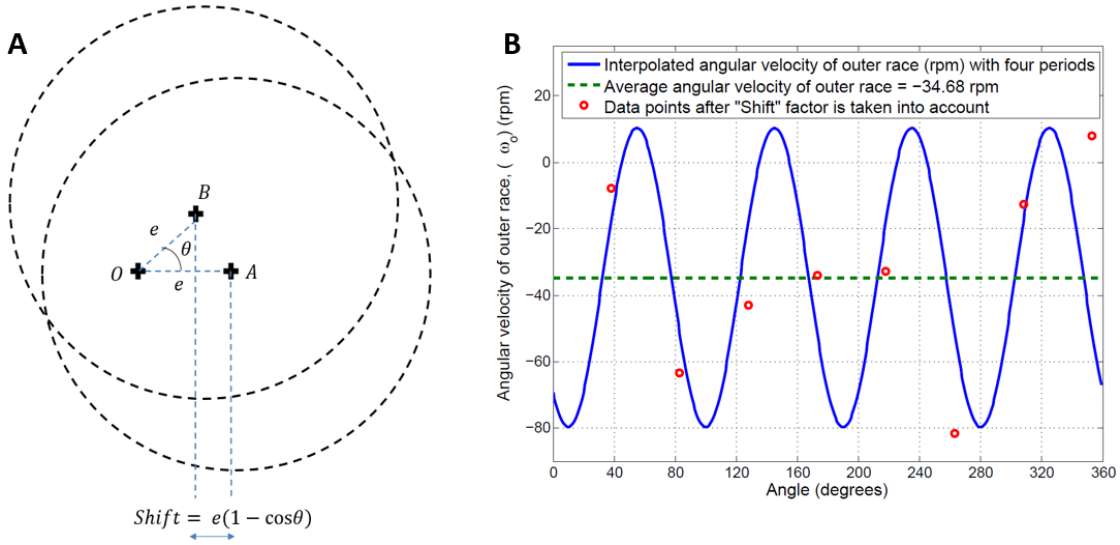

Figure 38: (A) Shift due to eccentricity which must be subtracted from the experimentally measured angular velocity, (B) Actual variation of the angular velocity of the outer race as a function of shaft angle.

In this manner, the variation of the angular velocity of the outer race can be calculated and used as the final input parameter for the friction model described in the previous chapter.

4.4 Numerical Evaluation of the Friction Coefficient at the Cam/Piston Interface

The input parameters to evaluate the friction coefficient at the cam-piston interface are shown in Figure 39. The angular velocity of the outer race was used to evaluate the entrainment velocity input parameter U_e from Equation (4.8). The variation of the friction coefficient as a function of the shaft angle is shown in Figure 40 (A).

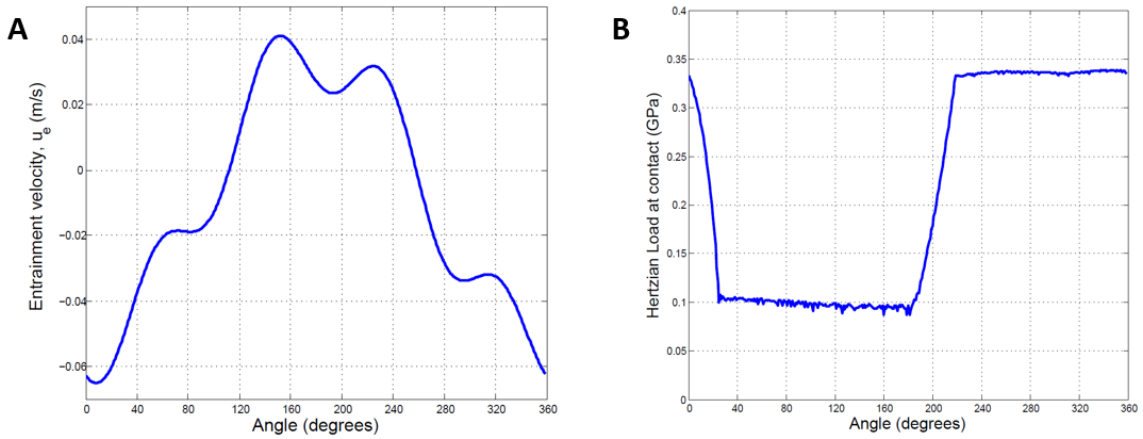

Figure 39: Input parameters for the EHL friction model for Pump outlet pressure: 700 bar, Shaft speed: 1800 rpm. (A) Entrainment velocity, (B) Hertzian load at the contact interface.

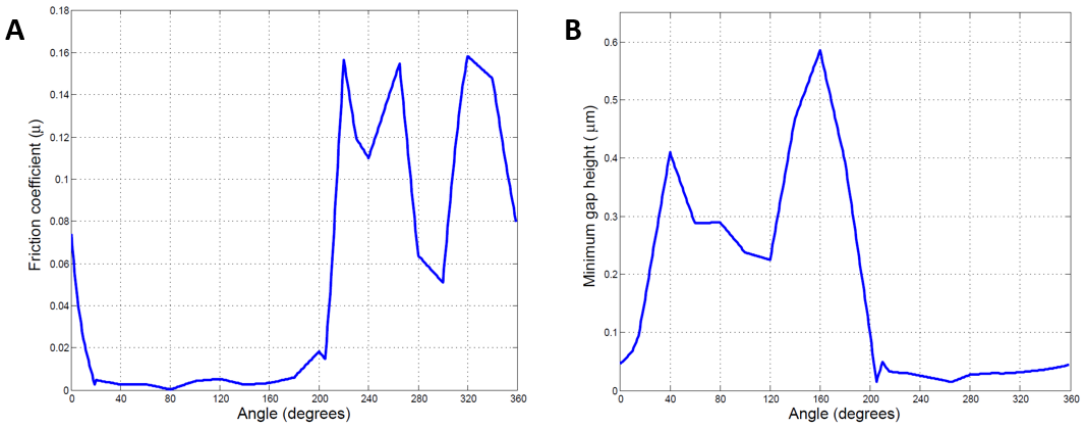

Figure 40: Outputs from the EHL friction model for Pump outlet pressure: 700 bar, Shaft speed: 1800 rpm. (A) Friction coefficient variation over one pumping cycle, (B) Minimum gap height variation at the interface over a pumping cycle.

From the point of view of the outer race, it can be deduced that the friction coefficient during the suction stroke (0^o to 180^o) of one pumping cycle is predicted to be of the order of 0.001, whereas it appears to be of the order of 0.1 during the discharge stroke (180^o to 360^o). The higher magnitude of the friction coefficient during the discharge stroke appears to suggest that the lubricating regime may not remain as full film lubrication. This is more so evident from Figure 40 (B) where the minimum gap height observed is predicted to be less than 1 μm throughout the pumping cycle at steady state.

This illustrates the need for the evaluation of the friction due to asperity contact interactions to be included along with the viscous friction that is being evaluated using the current line EHL numerical model.

4.5 Model Validation: An Indirect Empirical Approach

In order to validate the results of the friction coefficient variation between the outer race and each piston as a function of shaft angle, an indirect approach is formulated involving a force and moment analysis of the cam's outer race.

Figure 41 depicts the different forces acting on the outer race. Since, the frictional forces due to the ball bearings are not being modeled during the analysis, they are observed to be the only unknown present in Equation (4.11). By solving this equation, a comparison is made between the coefficients of frictional force due to the ball bearings obtained (from Figure 41) and practically observed values in real-life scenarios for ball bearing operation.

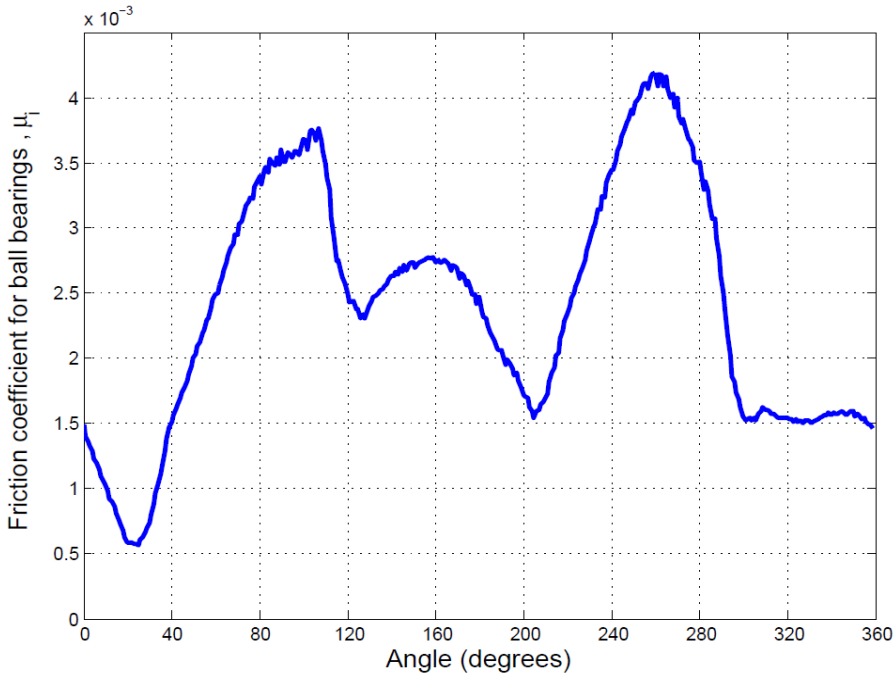

Figure 41: Variation of the friction coefficient with shaft angle as obtained from solving the moment-balance equation of the outer race.

As seen from the figure, the range of values obtained for the friction coefficient due to the ball bearings for one revolution of the shaft ($\approx 0.0005 - 0.0043$) appear to satisfy the physically realizable estimates for the same (typically of the order of ≈ 0.001) during efficient bearing operation, at steady state. Thus, this indirect approach to validate the comprehensive cam-piston interface model proves to be satisfactory.

4.6 Results from the Fully-Coupled FSI-EHD Pump Model

In this section, the results from the fully-coupled model are discussed. Here, the full film FSI-EHD model of the piston/cylinder interface is coupled with the EHL friction model for the cam/piston interface. The details of the design input parameters used to obtain all the simulation results represented in this section for the reference pump design are shown in Table 2.

Table 2: Design input parameters for the reference pump used in the simulation results.

Parameter	**Description / Value**
Displacement	1.0 cc/rev
Nominal clearance between piston and cylinder	8 μm
Working fluid	ISO VG 32 Hydraulic Oil
Density @ 15°C	869 kg/m^3
Viscosity @ 15°C	0.02 Pa-s
Piston & Cylinder Materials	Steel
Young's modulus	210 GPa
Poisson's ratio	0.29
Density	7850 kg/m^3

4.6.1 Pressure Profiles and Gap Height Distributions

Figures 42 and 43 illustrate the variations of the pressure field as well as the gap film thickness in the lubricating gap domain over one shaft revolution upon convergence of the described FSI solution algorithm at an operating condition of 700 bar pressure at the outlet and a shaft speed of 1800 rpm. The variation of the pressure within the

displacement chamber shown in Figure 12 is used as a boundary condition. The fields shown are for a single piston-cylinder pair. They are represented on an unwrapped configuration where ∅ represents the circumferential angle and ŷ is gap length along the axis of the cylinder. Also, θ represents the shaft angle which is the angle through which the eccentric cam rotates, and $\theta = 0^o$ is the position of the piston when it is at the BDC (start of the suction stroke). It is evident from these figures that lower pressures are present during the suction stroke ($\theta = 0^o - 180^o$), whereas during the delivery stroke ($\theta = 180^o - 360^o$), there is a pressure build up in the displacement chamber resulting in higher gap pressures. Also, depending upon the tilting position of the piston within the cylinder, there are pressure peaks or troughs present in the regions of low gap heights which are characteristic effects of the squeezing of the fluid film.

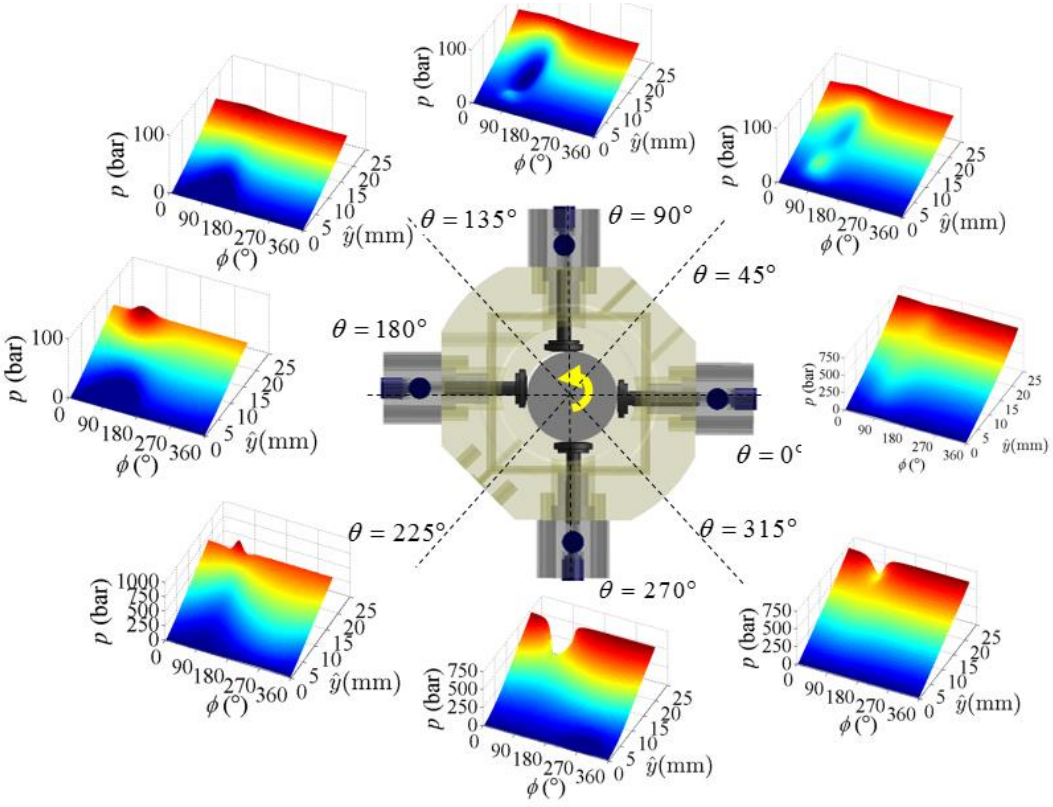

Figure 42: Unwrapped pressure field in the piston/cylinder gap domain over one shaft revolution for Pump outlet pressure: 700 bar, Shaft speed: 1800 rpm.

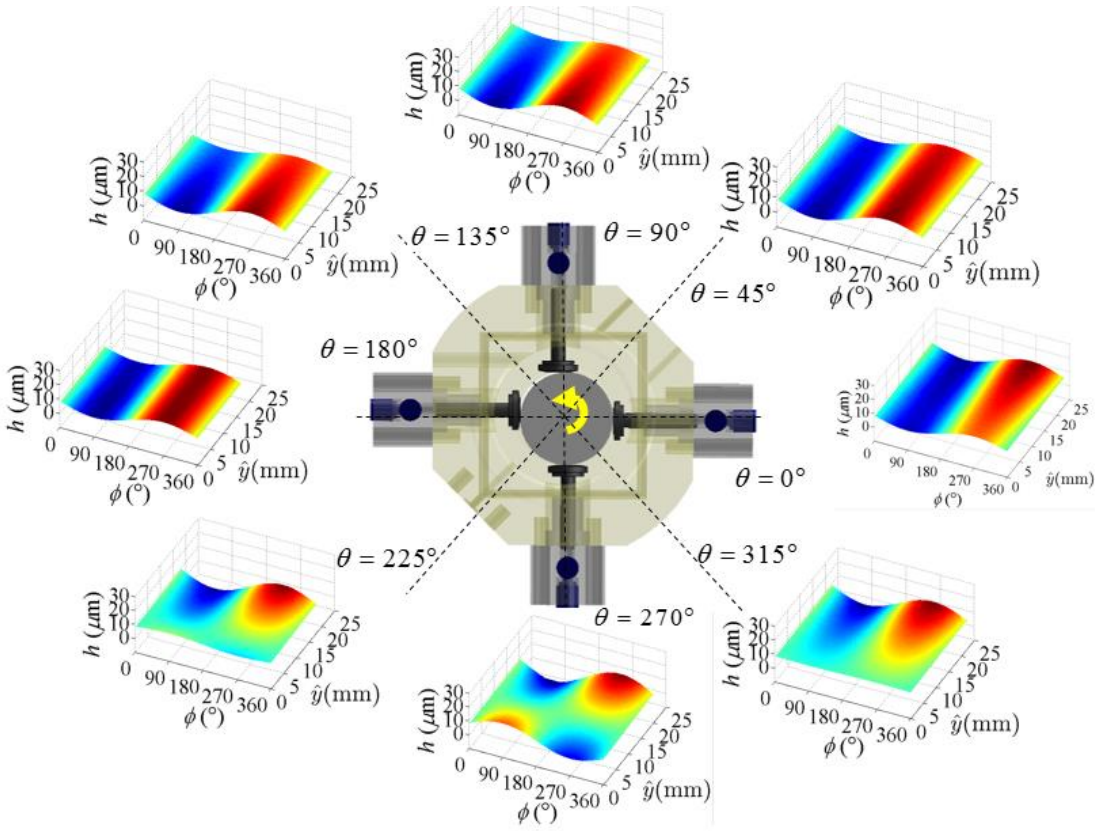

Figure 43: Unwrapped film thickness configuration in the piston/cylinder gap domain over one shaft revolution for Pump outlet pressure: 700 bar, Shaft speed: 1800 rpm.

4.6.2 Effect of Incorporating the Cam/Piston Friction Model on Piston Tilt

As mentioned earlier, the fully-coupled FSI-EHD pump model is an extension of the work presented in [6]. Due to the lack of a validated cam/piston model, an assumption was made for the friction coefficient between each piston and the outer race of the cam. A constant friction coefficient of $\mu = 0.1$ was assumed which is representative of a purely sliding contact condition between the two surfaces manufactured from steel (Figure 44 (A)). The outer race was also assumed to rotate in the same direction of the shaft at all instants during the pump cycle (Figure 44 (B)). Under these assumptions, it was found that the piston tilt being modeled was very different as compared to the present behavior observed from the fully-coupled algorithm (Figure 45).

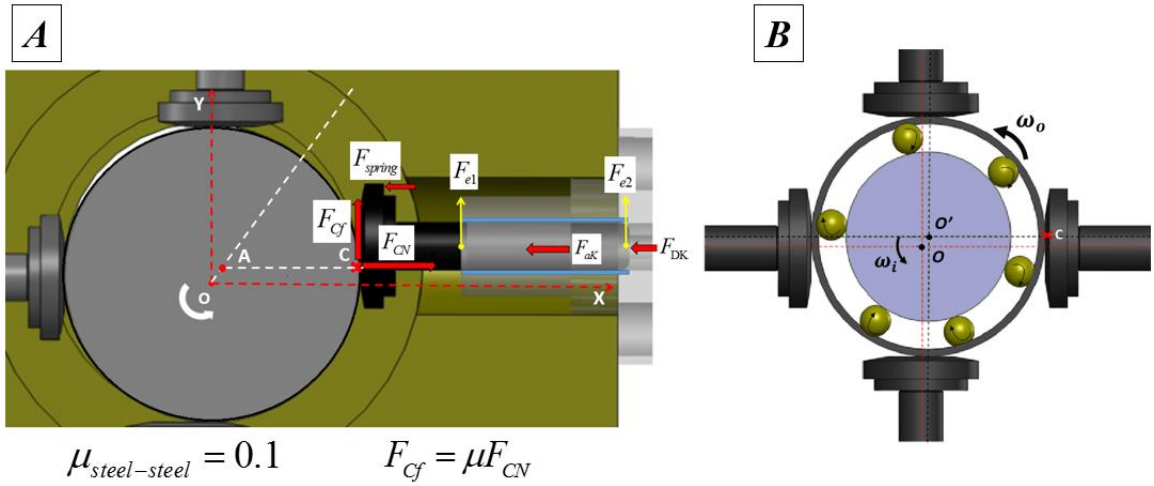

Figure 44: (A) Previously made assumption of the non-varying friction coefficient at the cam/piston interface, (B) Assumption for the rotational direction of the outer race (same as the direction of the shaft).

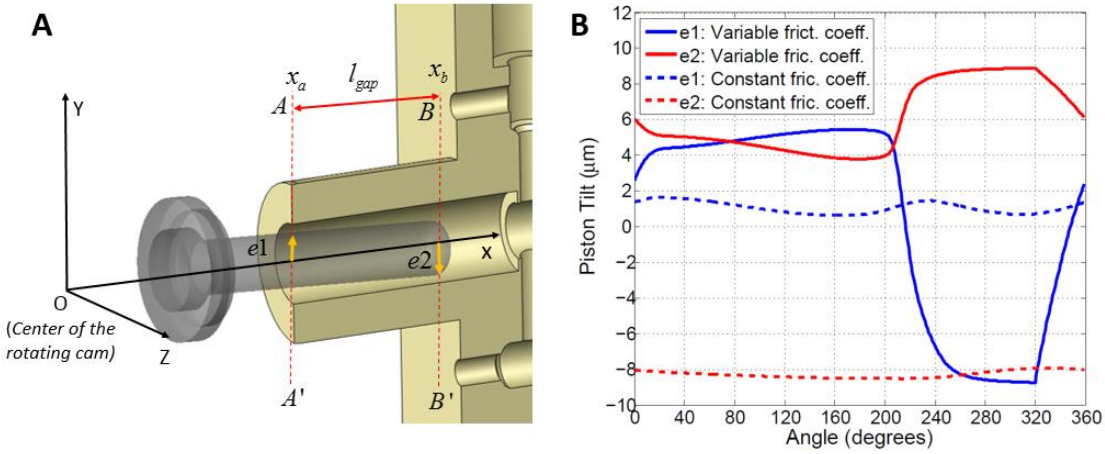

Figure 45: Comparison between the piston tilt behaviors of constant cam-piston friction coefficient assumption model and variable friction coefficient model over one shaft revolution for Pump outlet pressure: 700 bar, Shaft speed: 1800 rpm.

From observations made in Figure 45 (B), it may be concluded that the variation of the friction coefficient as well as the direction of rotation of the outer race during each shaft revolution at steady state are very important factors to be considered during the modeling of a rotating cam type radial piston machine. These considerations also play a major role in estimating the magnitude and location of possible solid contact that may be observed between each piston and cylinder during the pumping cycle.

4.6.3 Effect on Pump Performance

Figure 46 depicts the variation of the leakage in a single piston/cylinder gap over one shaft revolution. It can be seen clearly that high leakages through the gap exist during the delivery stroke ($\theta = 0^o - 180^o$) as there is a greater pressure difference between the displacement chamber end and the case of the pump. The mean leakage flow rate for the pump at each operating condition can be evaluated through a sum of all the leakages present in all four piston/cylinder interfaces and averaging over a pumping cycle. Figure 47 shows the variation of the viscous friction power loss at each piston/cylinder interface during one pumping cycle. By the same logic as before, a higher gradient in the pressures between the displacement chamber and the case results in higher values of the viscous friction forces present in the gap, thereby resulting in more viscous power losses across the gap. Overall viscous power losses are calculated in the same manner as done for the leakages evaluation.

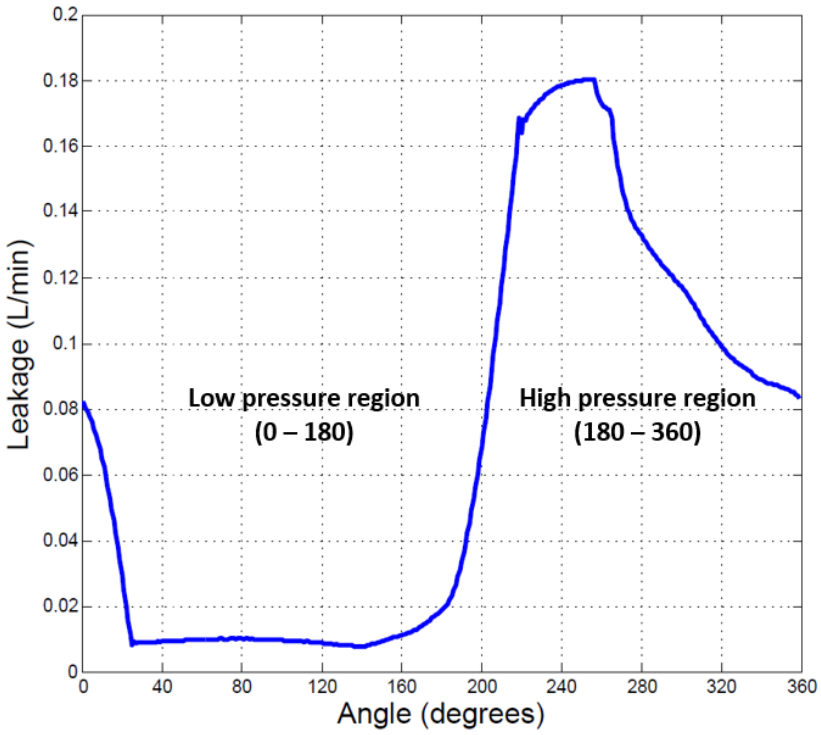

Figure 46: Variation of the leakage in the piston/cylinder interface as a function of the shaft angle for Pump outlet pressure: 700 bar, Shaft speed: 1800 rpm.

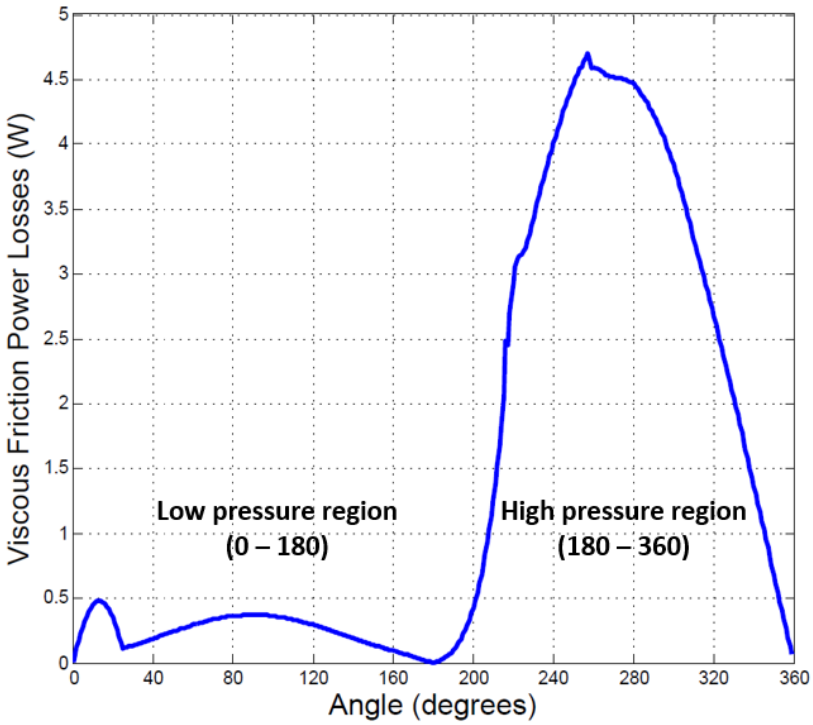

Figure 47: Variation of the viscous friction power losses in the piston/cylinder interface as a function of the shaft angle for Pump outlet pressure: 700 bar, Shaft speed: 1800 rpm.

The fully-coupled model was tested by simulating three operating conditions where the shaft speed was kept constant at 1800 rpm (which is the nominal speed at which the reference unit is operated at (using a fixed speed motor), for which measurements of the outer race velocity were available as previously described) and the outlet pressure was varied. Volumetric efficiency of the pump (considering leakage flow through the piston/cylinder gap) is compared in the two cases - when the cam/piston interface model is used, and when a constant friction assumption is made (Figure 48). Power losses due to viscous friction at both the piston/cylinder and cam/piston interfaces are plotted in Figure 49 for all the operating conditions shown. All four piston/cylinder interfaces present in the pump were considered for this analysis.

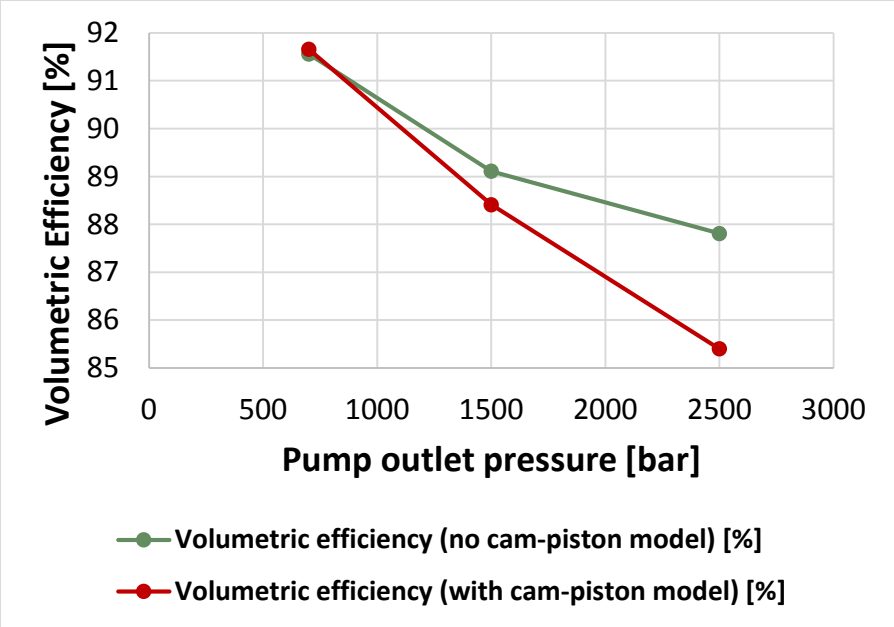

Figure 48: Comparison between the volumetric efficiencies evaluated with the constant cam/piston friction coefficient assumption model and the variable friction coefficient model for Pump outlet pressure: 700 bar, Shaft speed: 1800 rpm.

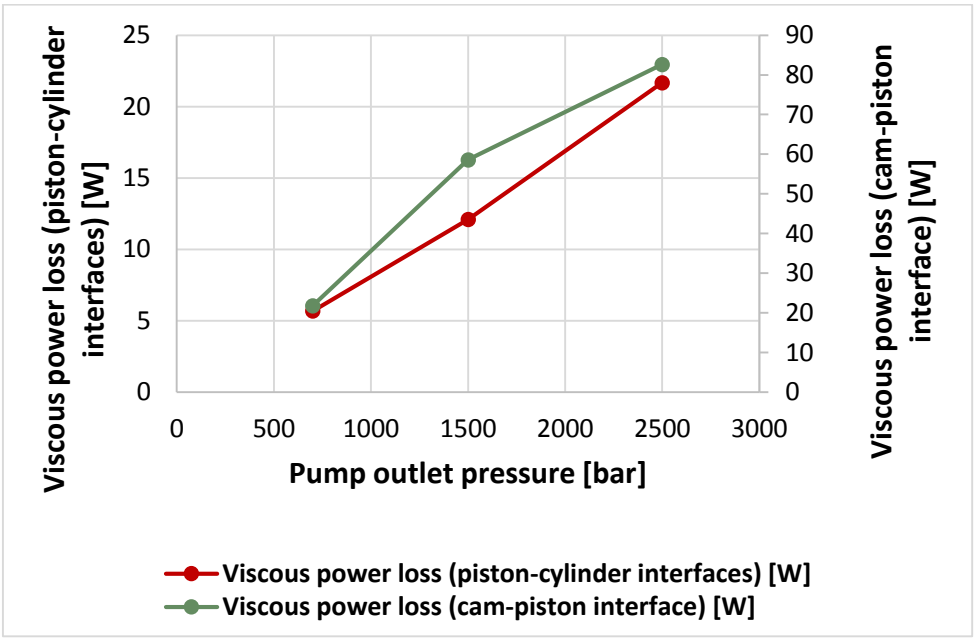

Figure 49: Comparison between the viscous power losses evaluated at the cam/piston and piston/cylinder interfaces with the constant cam/piston friction coefficient assumption model and the variable friction coefficient model for Pump outlet pressure: 700 bar, Shaft speed: 1800 rpm.

By considering the cam/piston interface, it is clear that the behavior of the piston tilt also influences the amount of leakage at the piston/cylinder interface, thereby affecting the accuracy of the volumetric efficiencies predicted for the machine at different operating conditions. This is evident from Figure 48 where a significant difference in volumetric efficiency is predicted especially at ultra-high pressures (2500 bar). It is also seen that the power losses due to viscous friction losses present at the cam/piston interface are very significant – even more so than the losses present at the piston/cylinder interface, for each revolution of the shaft (as observed from Figure 49).

The full film piston/cylinder gap assumption is used to make the comparisons shown in this section. This is done to demonstrate the importance of accurately evaluating the variation of the friction coefficient at the cam/piston interface on the piston tilt and gap performance. The importance of the mixed lubrication assumption at the piston/cylinder interface will be demonstrated using the results obtained from the variable friction model later.

CHAPTER 5. POTENTIAL OF THE FULLY-COUPLED FSI-EHD MODEL IN INVESTIGATING THE EFFECT OF CIRCUMFERENTIAL PISTON GROOVES ON LUBRICATING PERFORMANCE

This chapter presents the potential of the fully-coupled model developed in designing efficient and durable radial piston machines. With the two aspects of efficiency and durability serving as ultimate goals of this research, the effects of surface features – namely circumferential piston grooves – were analyzed towards aiding in achieving these goals.

Two major operating conditions were considered while conducting all the analyses presented in this chapter. They are shown in Table 3. The reason behind examining these two particular operating conditions is primarily to improve the design of the reference machine in order to reach extremely high operating pressures (>700 bar).

Table 3: Operating conditions at which the features of the reference design is examined.

Outlet Pressure [bar]	**Shaft Speed [rpm]**
700	1800
2500	1800

5.1 Investigating Grooved Piston Designs

The primary motivation behind introducing surface features such as circumferential grooves on the pistons is that the grooves can enable a region of constant lubricant pressure which may influence the tilting of the piston and finally, prevent wear due to metal-metal contact between the surfaces of the pistons and the cylinders. This technique of modeling the effect of grooves has been employed in different applications in the past [48-50]. In the following sections, the manner by which the location and number of the piston grooves affect the wear and performance of the pump are detailed.

To investigate the effect that circumferential piston grooves may have on the hydrodynamic effect as well as piston tilt (wear due to metal-metal contact) during operation, multiple case studies were conducted. The cases considered are shown in Figure 50. The unwrapped, 2D fluid meshes constructed for each of these cases are also shown.

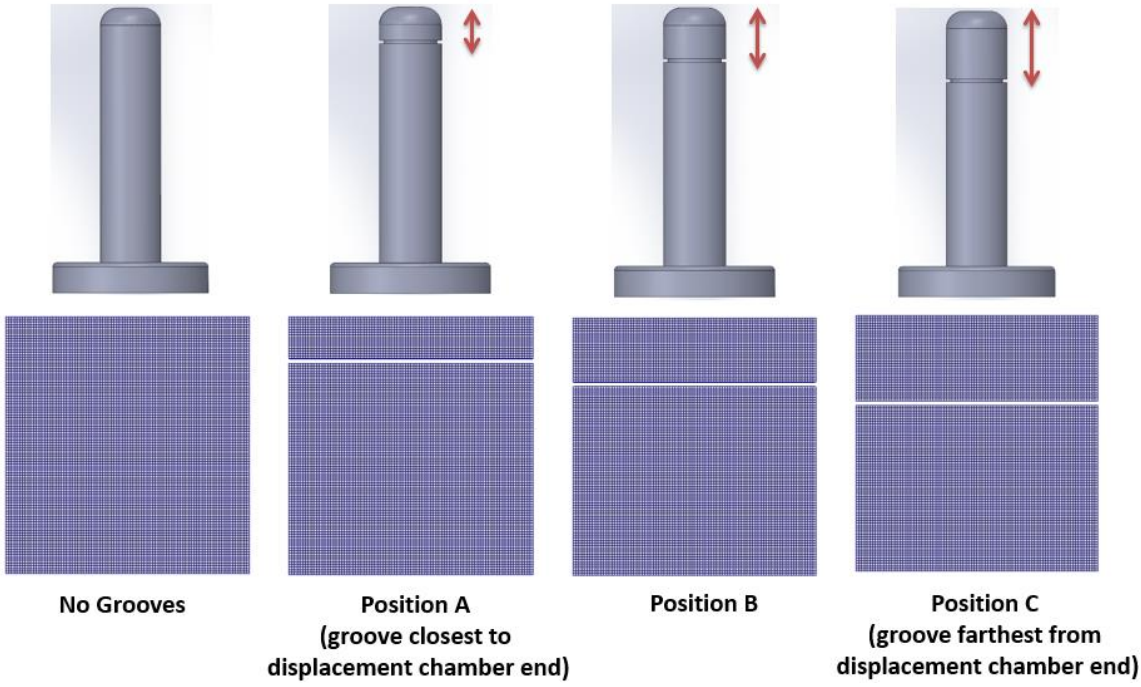

Figure 50: Groove configurations on the piston studied with respect to position.

The modeling approach adopted to calculate the pressure within these grooves has been shown in Section 3.2.2. By using the control volume approach described, the pressure within each groove is calculated to be the same along the particular groove surface. Figure 51 illustrates the variation of the pressure within the groove at Position ‘A’ over a single pumping cycle. The change in the flow rates entering this groove from its either side over the shaft revolution is also shown in Figure 52. As seen from the figure, the observed flow rates tend to equalize with each other in magnitude as they enter the groove from its either side.

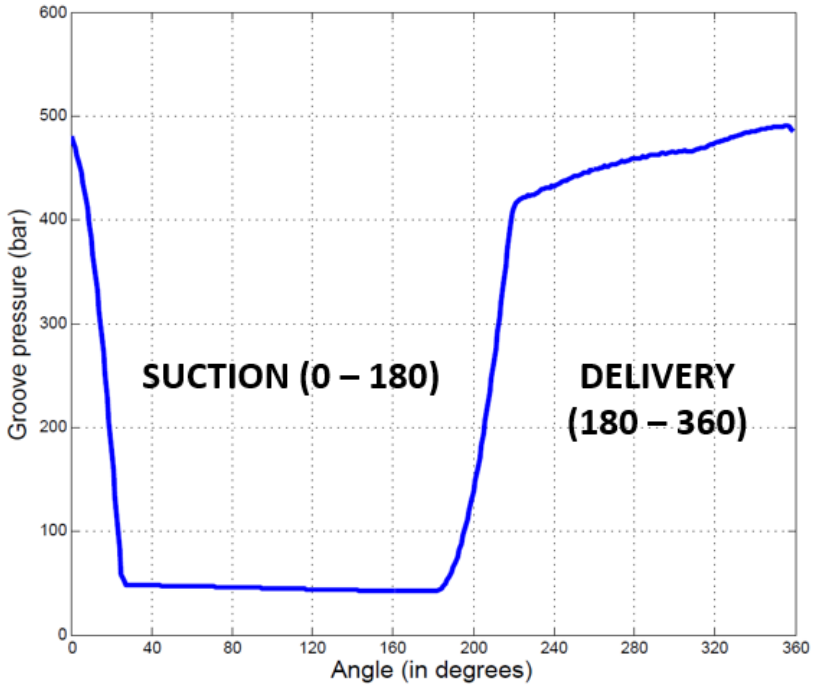

Figure 51: Variation in the groove (at Position 'A') pressures as a function of shaft angle for Pump outlet pressure: 700 bar, Shaft Speed: 1800 rpm.

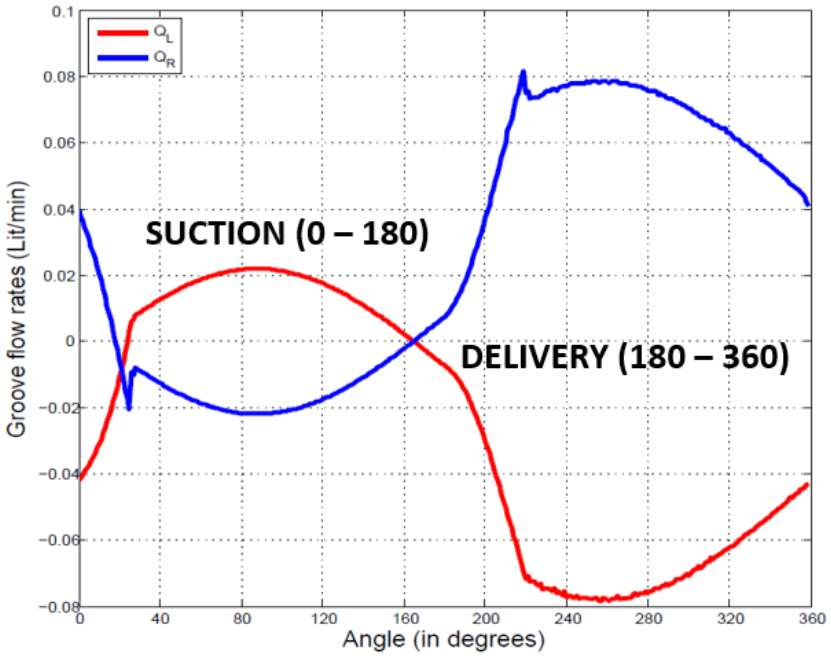

Figure 52: Variation in the flow rates entering the groove (at Position 'A') from its either side as a function of shaft angle for Pump outlet pressure: 700 bar, Shaft Speed: 1800 rpm.

In order to understand the effect that the position of a single groove can have on the piston tilt, comparisons are made between the reference employing grooved pistons with the groove position varied against the reference pump using pistons without any grooves. The results obtained through such comparisons are detailed in the following section.

5.2 Significant Results

5.2.1 Effect of Grooves on Piston Tilt and Hydrodynamic Effect

The first important effect to consider is whether or not the presence of a groove affects the hydrodynamic effect created during pump operation. This can be studied by a thorough analysis of the various terms present in the Reynolds equation used to solve for the pressure distribution within the fluid.

Each term in the Reynolds equation captures different effects, as described below:

$$\nabla.\left(\frac{\rho h^3}{12\eta}\nabla p\right) - \left(\frac{\rho \boldsymbol{V}_b}{2}\right).\nabla h - \rho \boldsymbol{V}_b.\nabla h_b - \rho\frac{\partial h}{\partial t} = 0 \qquad (5.1)$$

where:

$\nabla.\left(\frac{\rho h^3}{12\eta}\nabla p\right)$: The "Poiseuille" term which represents the diffusion of the pressure from the boundaries into the domain.

$\left(\frac{\rho \boldsymbol{V}_b}{2}\right).\nabla h$: The "Physical Wedge" term which represents pressure generation due to a variation in the gap height along the sliding length (inclined piston with respect to the cylinder).

$\boldsymbol{V}_b.\nabla h_b$: The Translational Squeeze" term which represents the pressure generation due to the translation of the inclined piston within the stationary cylinder.

$\rho\frac{\partial h}{\partial t}$: The "Normal Squeeze" term which represents the pressure generation due to a difference in the normal velocities generated by micro-motion of the piston during operation.

Two cases were examined in detail to study the hydrodynamic effect: the first case of pistons without grooves and the second case using a piston with one groove located at Position ‘A’ (Figure 50).

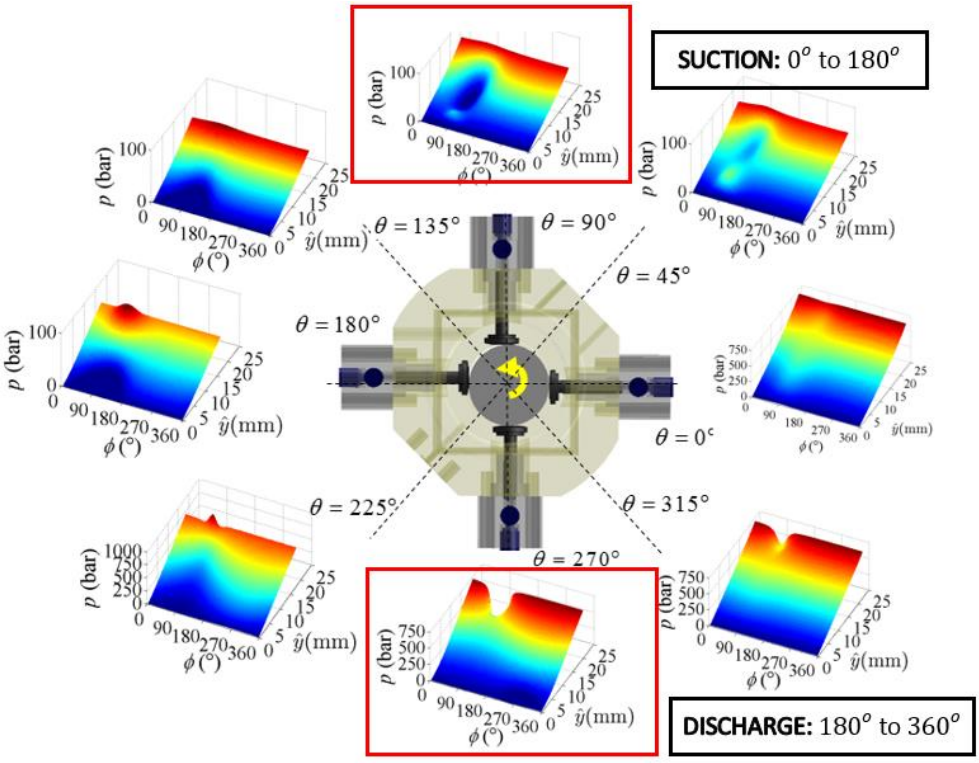

Figure 53: Instantaneous pressure field in the lubricating gap domain over one shaft revolution obtained using the piston/cylinder FSI-EHD model for Pump outlet pressure: 700 bar, Shaft speed: 1800 rpm.

A change in the balance is observed in the case of Groove Position ‘A’ as compared to the case without any piston grooves. This is better shown through an analysis of which term in the Reynolds equation is affected the most due to the presence and position of a groove, i.e. the terms in the Reynolds equation that contribute to an increase in the hydrodynamic pressure generation. For this, the terms in the Reynolds equation are analyzed for two positions – one during the suction stroke (0^o to 180^o) and one during the discharge stroke (180^o to 360^o) during a single revolution of the shaft. The two instants studied are shown in Figure 53 which depicts the instantaneous pressure profile

in the gap in an unwrapped configuration, for an operating condition where the pump outlet pressure is 700 bar and shaft speed of 1800 rpm.

For both the cases analyzed, the effects of each term are shown through observing the fluid domain in an unwrapped configuration (Figures 54-57). The magnitude of the pressures represented by each term in the figures have units of Pascals.

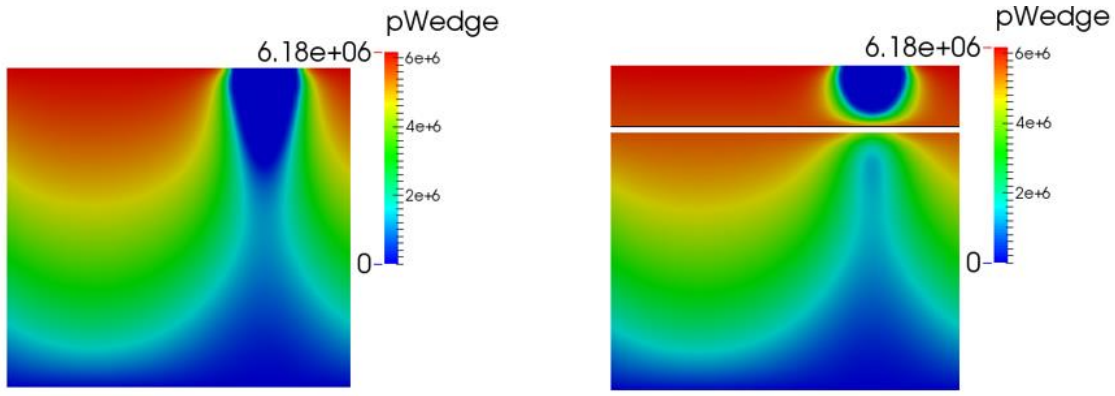

Figure 54: Comparison between the pressures generated from the wedge effect for the case of a piston with no grooves (left) and a piston with grooves at Position A (right) during one instant of the suction stroke.

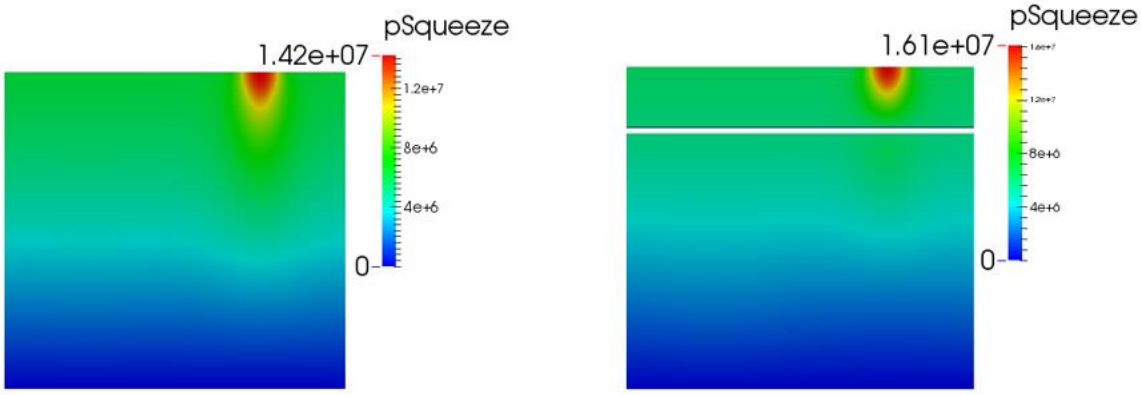

Figure 55: Comparison between the pressures generated from the normal squeeze effect for the case of a piston with no grooves (left) and a piston with grooves at Position A (right) during one instant of the suction stroke.

During the suction stroke of the piston, it is observed that the hydrodynamic pressure generation is enhanced through an increase in the pressure generated through the Normal Squeeze and Physical Wedge effects.

In Figure 54, it can be observed that the magnitude of pressure generated due to the wedge effects are higher especially in the area surrounding the groove. Regions of blue and green signifying lower pressure regions in the case of a piston with no grooves are replaced by regions of red which signify much higher pressures. The same effect of creating a region of constant pressure of higher magnitude around the groove can be observed through an analysis of the normal squeeze effect in Figure 55, for both piston cases.

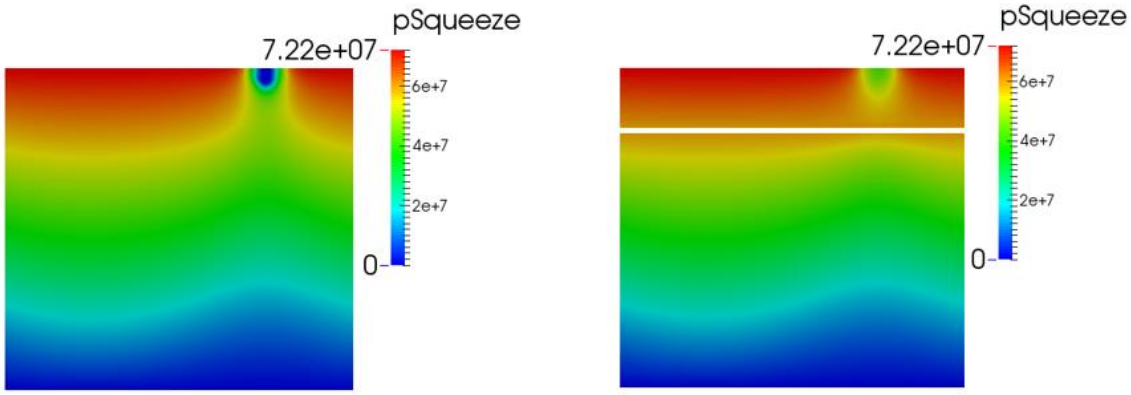

Figure 56: Comparison between the pressures generated from the normal squeeze effect for the case of a piston with no grooves (left) and a piston with grooves at Position A (right) during one instant of the discharge stroke.

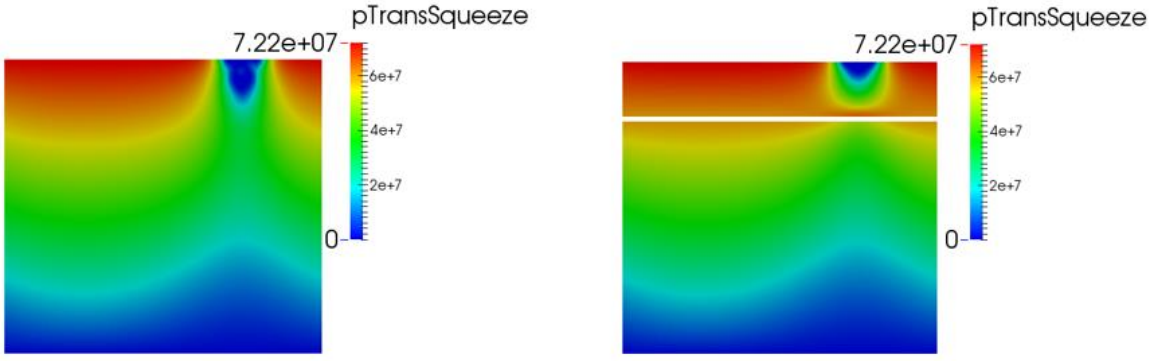

Figure 57: Comparison between the pressures generated from the translational squeeze effect for the case of a piston with no grooves (left) and a piston with grooves at Position A (right) during one instant of the discharge stroke.

A similar phenomenon is observed in the case of the discharge stroke of the piston during each shaft revolution. In this case, the terms which play an important role in increasing the overall hydrodynamic pressure generation in the gap are the Normal Squeeze term and the Translational Squeeze term in the Reynolds equation. Figure 56 shows the region of higher pressures (in red) due to the normal squeeze effect surrounding the groove as compared to the same instant of time for the case of a piston with no grooves (pressures in yellow and green in the same location). The same can be said of the pressure generation due to the translational squeeze effect for the two cases during the same instant of the discharge stroke which is analyzed in Figure 57.

Thus, for the particular case of Groove Position 'A', it is seen that change in the balance of the piston is possible due to the improved hydrodynamic effect caused by the position of the groove, as compared to the case where no grooves were present.

5.2.2 Piston Balance and Investigating Piston/Cylinder Contact

It has been shown that grooves affect the balance of the piston. However, the position of the grooves can influence whether or not the balance of the piston improves and whether the load is being completely supported by the fluid film. For this reason, the reference pump operated with pistons having different groove positions – namely Position 'A', 'B' and 'C' – are examined assuming full film lubrication conditions with EHD effects. The variation of the magnitude of the artificial contact load applied to maintain the stability of the numerical procedure is examined for each of the cases, over a single pumping cycle at a pump outlet pressure of 2500 bar and shaft speed of 1800 rpm as shown in Figure 58.

It can be observed that while there is contact occurring between the piston and cylinder for a large duration during the one cycle (20^o to 60^o and 180^o to 210^o) when no grooves are present, this contact is significantly reduced in the case of a single groove positioned closest to the displacement chamber end of the piston (Groove Position 'A' from Figure 50). Contact here seems to occur for only a short period (180^o to 210^o) and the magnitude of this contact appears to reduce as well. This has great significance in the fact

that wear that may be occurring due to this metal-metal contact is greatly reduced and the overall pump operational life can be improved.

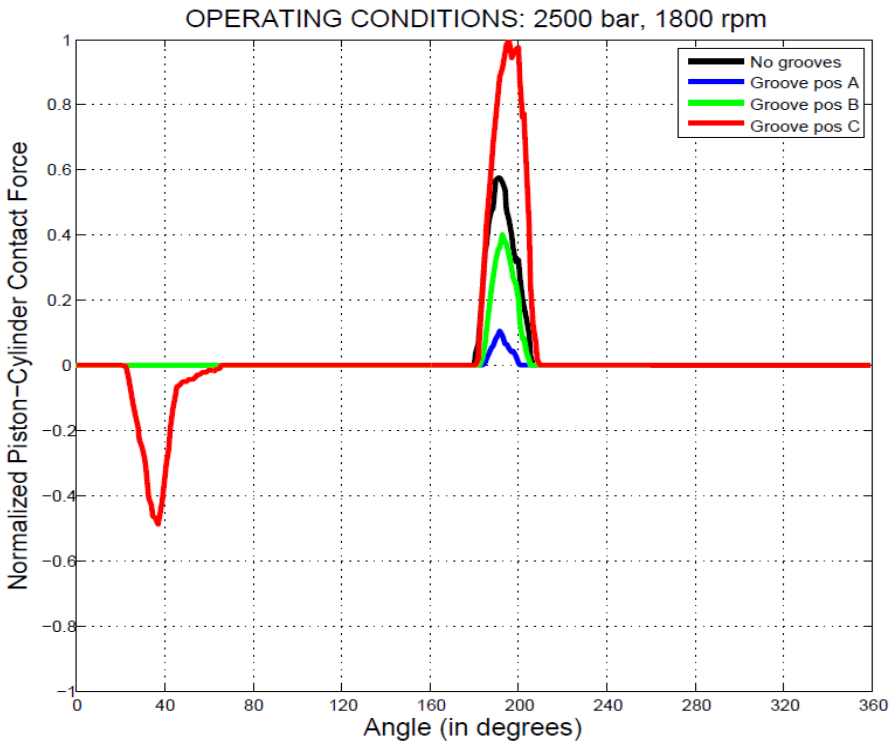

Figure 58: Regions of contact over one pumping cycle at Pump outlet pressure: 2500 bar, Shaft speed: 1800 rpm.

Another important fact to note is that, the farther the position of the groove from the displacement chamber end of the piston, the greater the contact force. Since a full film lubrication assumption is made, this trend in contact force observed could potentially give misguiding results with respect to pump performance, as seen in the next section.

A better balance is observed in the case of Groove Position ‘A’ as compared to the other cases (for both operating conditions) since the hydrodynamic force generated by the lubricant due to the squeeze effect is sufficient to balance the load causing the piston to tilt.

An illustration of the improvement in piston balance by appropriately positioning the groove is shown in Figure 59.

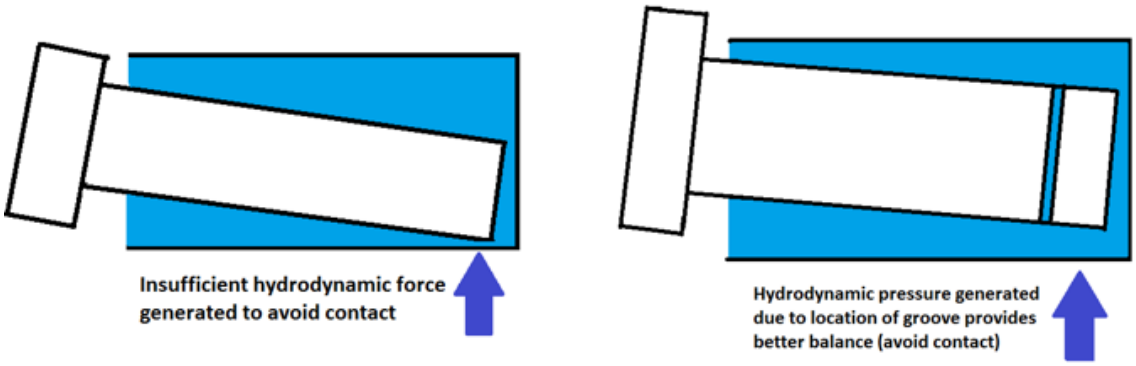

Figure 59: Illustration of the improvement in the piston balance due to additional hydrodynamic pressure generation enabled by the position of the groove on the piston.

At the same time, while observing the effect of changing groove positions, it can be seen that a small change in positioning the groove away from the displacement chamber end of the piston causes an increase in the metal-metal contact predicted, both in magnitude and in the duration of contact. Therefore, it is important to have an optimized location for the groove on each piston while designing them for lasting pump operation, especially at the ultra-high operating pressures under consideration.

One important point to mention here is that while an ‘optimal’ groove position such as Position ‘A’ can reduce the simulated metal-metal contact, it is seen that even in such cases, there is an unavoidable contact force present. This lends credibility to the conclusion that conditions of mixed lubrication may be present for particular durations of the pumping cycle. Hence, a modeling methodology based on mixed lubrication must be tested in order to design radial piston pumps that are durable. This is investigated in detail in the next chapter, based on the methodology proposed in Section 3.3 of Chapter 3.

5.2.3 Effect of Piston Grooves on the Lubricating Performance

The impact of a single groove on the balance of the piston has been studied. For an analysis of the pump performance, more configurations can be considered. The fluid meshes of all the groove configurations studied in this section have been shown in Figure 60. The pump performance was analyzed for both the operating conditions shown in Table 3.

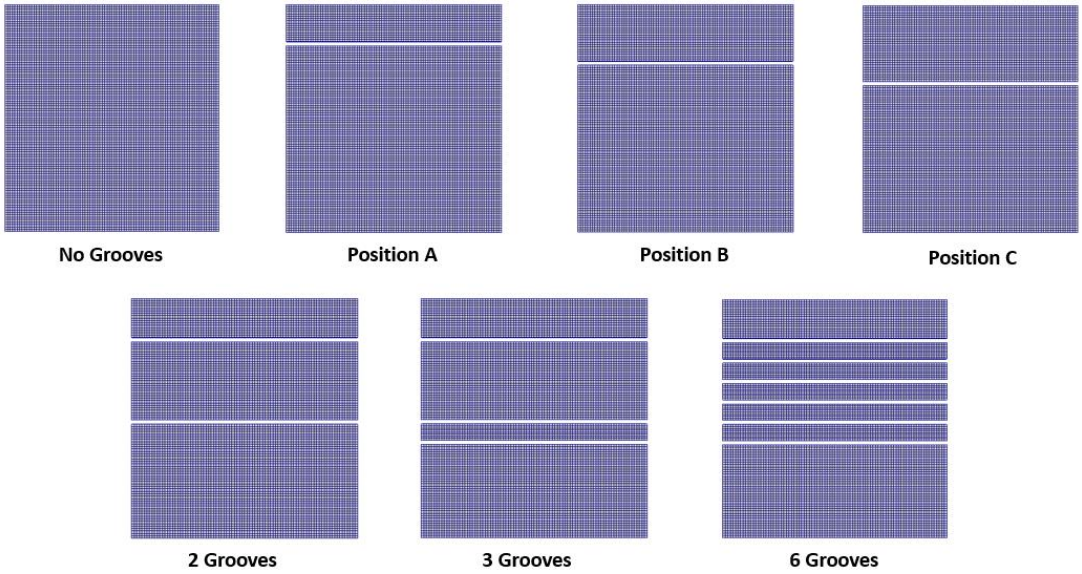

Figure 60: Computational grids generated for the fluid domains of multiple pistons with various groove configurations.

Table 4: Performance parameters observed per revolution of the shaft under steady state conditions at Pump outlet pressure: 700 bar, Shaft speed: 1800 rpm.

Piston Configuration	**Power loss due to Leakage [% of total losses]**	**Power loss due to Viscous friction [% of total losses]**	**Volumetric Efficiency [%]**
No Grooves	8.03	0.34	92.57
Position A	8.71	0.33	91.99
Position B	8.74	0.33	91.97
Position C	8.77	0.33	91.94
2 Grooves	8.22	0.34	92.41
3 Grooves	7.96	0.34	92.63
6 Grooves	7.45	0.37	93.07

Table 5: Performance parameters observed per revolution of the shaft under steady state conditions at Pump outlet pressure: 2500 bar, Shaft speed: 1800 rpm.

Piston Configuration	**Power loss due to Leakage [% of total losses]**	**Power loss due to Viscous friction [% of total losses]**	**Volumetric Efficiency [%]**
No Grooves	13.88	0.38	87.81
Position A	14.28	0.36	87.50
Position B	14.36	0.36	87.45
Position C	14.82	0.36	87.37
2 Grooves	12.95	0.37	88.53
3 Grooves	12.66	0.37	88.77
6 Grooves	12.07	0.38	89.23

From Tables 4 and 5, there are a few notable observations in the trend for the performance parameters of the pump:

- The position or the number of grooves do not appear to play a major role in influencing the viscous power losses in the piston/cylinder interface.
- When a single groove was introduced, the improvement in the piston balance led to a reduction in piston-cylinder contact, thereby increasing the leakages (reduction in volumetric efficiency). However, this increase in leakages is acceptable, especially since a better balance is predicted. This conclusion is verified by taking the surface features into account in the mixed lubrication model in Chapter 6.
- As the number of grooves increases, the power loss due to leakages was found to decrease (increase in volumetric efficiency). This could be attributed to the fact that as the number of grooves positioned away from the displacement chamber end increases, the balance of the piston worsens, thereby introducing more contact in the piston/cylinder interface. While this ‘contact’ tends to seal the interface better (assuming full film lubrication conditions), a larger magnitude of predicted contact only lends more credibility to the fact that a mixed lubrication regime could be present.

This could potentially lead to incorrect estimations of the leakages for a vast majority of grooved piston designs that could be tested in simulation.

Based on the above points of note, any optimization routine that could be tested for obtaining optimal groove parameters would provide incorrect results based on the full film assumption. Thus, it may be concluded that exploring optimal circumferential groove designs requires an evaluation of the mixed lubrication characteristics in high pressure radial piston machines.

CHAPTER 6. POTENTIALS OF THE MIXED FSI-EHD COUPLED MODEL IN STUDYING THE IMPACT OF SURFACE ROUGHNESS AND SOLID ASPERITY CONTACT ON PISTON BALANCE AND PUMP PERFORMANCE

6.1 Significant Features of the Model

In this chapter, the various features of the Mixed FSI-EHD fully-coupled model will be highlighted. As mentioned earlier, the primary motivation for developing this model is to observe the effect of extremely low gap heights ($< 2\,\mu m$) that occur – especially at extreme operating conditions of ultra-high pressures – on the lubricating performance.

As the gap heights reach these low values, the impact of the surface roughness in the solids – piston and cylinder – becomes quite important while modeling the flow in the piston/cylinder interface. As these surface asperities become relevant, care must be taken to accurately model the elastic-plastic deformation of these asperities as they interact with one another. This effect is basically characterized by a real area of contact between the surface asperities, as opposed to a nominal contact area given by the entire surface areas of the undeformed asperities. For this reason, the model proposed by Lee and Ren (1994) has been used to evaluate these effects and the resulting areas of contact observed are shown at a particular time step in Figure 61. The corresponding contact pressures generated are also shown. The operating condition chosen for the plots and comparisons depicted here are an outlet pressure of 700 bar, shaft speed of 1800 rpm.

Figure 62 provides an understanding of the distribution in the load support due to the fluid film and the contact area. As seen, a spike in the fluid pressure is observed in the region with low predicted gap heights as the fluid strives to support the load in those areas, with some portion of the load being shared by the asperities. However, a sharp

drop in fluid pressures are observed in the regions where higher surface asperity contact occurs, where the asperity contact pressure supports the bulk of the load.

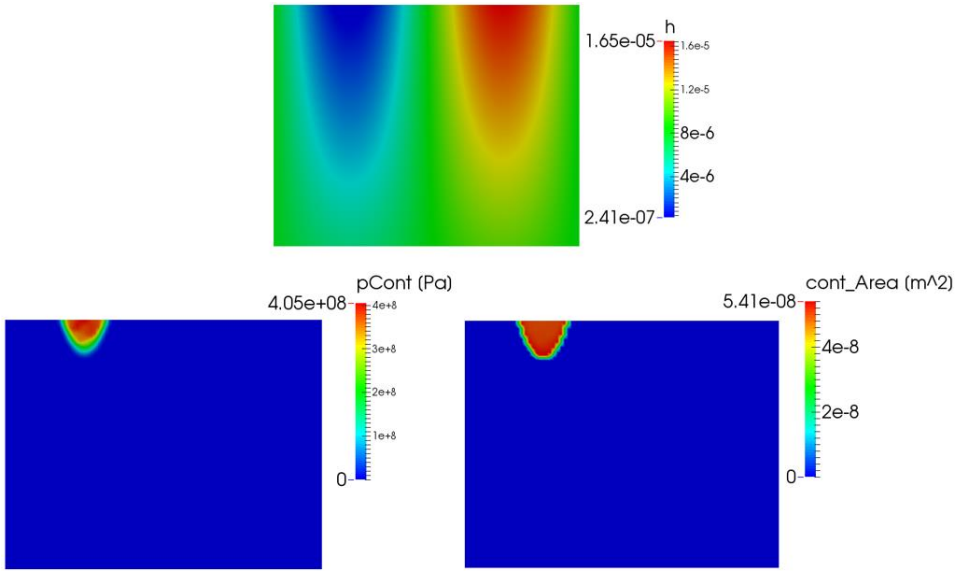

Figure 61: Contact pressures and the corresponding areas of contact observed at low gap heights during the shaft revolution for Pump outlet pressure: 700 bar, Shaft speed: 1800 rpm.

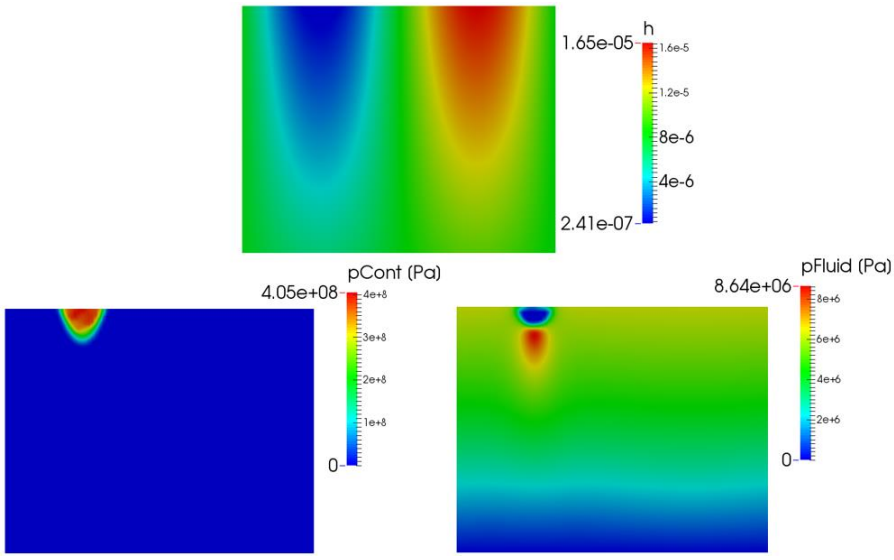

Figure 62: Load support shared between the contact pressures and the fluid pressures (red portions) in the region close to very low gap heights and the breakdown of the fluid at regions of very low gap heights (blue portions) where the load is mostly supported by the contact pressures for Pump outlet pressure: 700 bar, Shaft speed: 1800 rpm.

The effect of mixed lubrication is also observed in the case of the piston tilt as shown in Figure 63. The two ends of the gap length in the piston are given by the piston eccentricities e_1, e_2. As the piston eccentricities reach the order of the clearance between the piston and cylinder, low gap heights are observed in those regions. As seen in the figure, the piston tilt is observed to decrease at these instants ($180^o - 230^o$) of the shaft revolution when mixed lubrication is modeled, as compared to the case where full film lubrication is assumed.

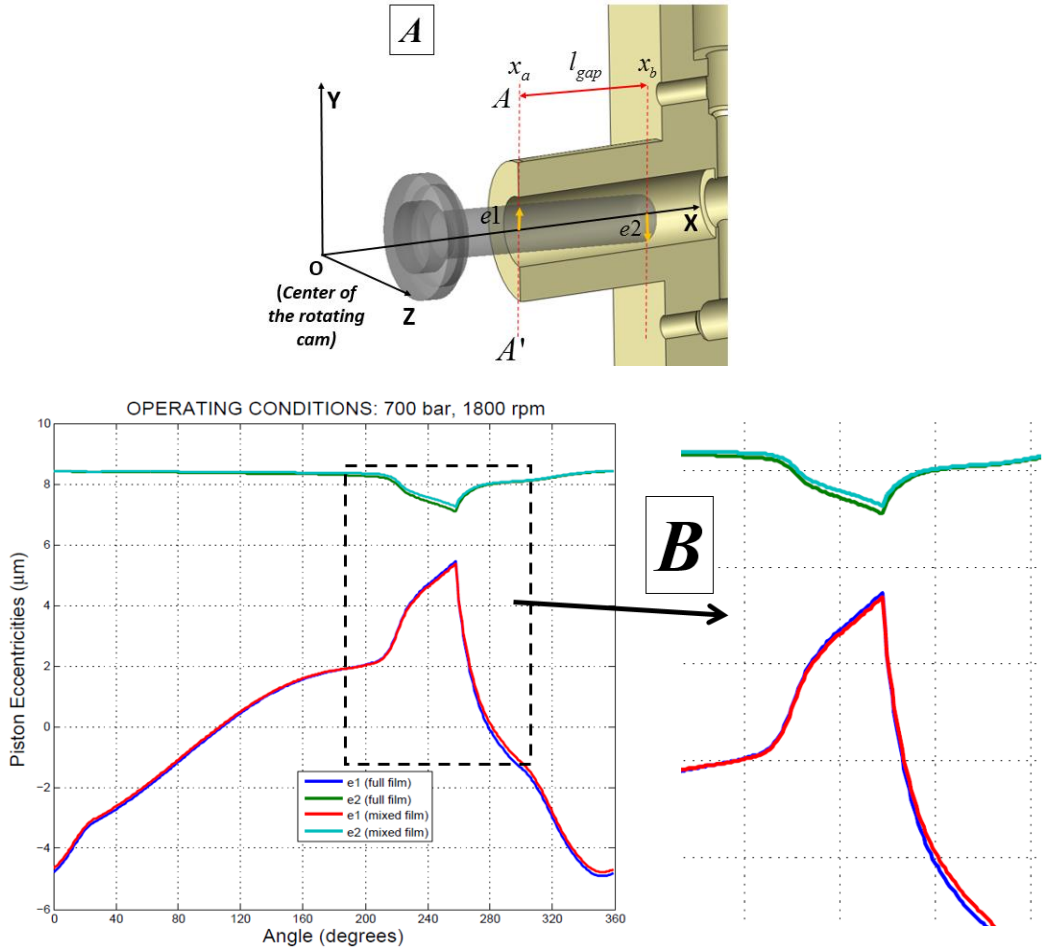

Figure 63: (A) Parameters describing the piston tilt, (B) Comparison between the variation in piston tilt observed between full film and mixed lubrication models over one shaft revolution for Pump outlet pressure: 700 bar, Shaft speed: 1800 rpm.

There is also an impact on the variation of the minimum film thicknesses observed over the pumping cycle (Figure 64). As the effects of mixed lubrication are taken into account, it is observed that the full film lubrication assumption slightly underestimates the film thickness during the suction stroke, while it overestimates it during the start of the delivery stroke. This can influence the performance parameters of the pump such as leakage and viscous friction losses.

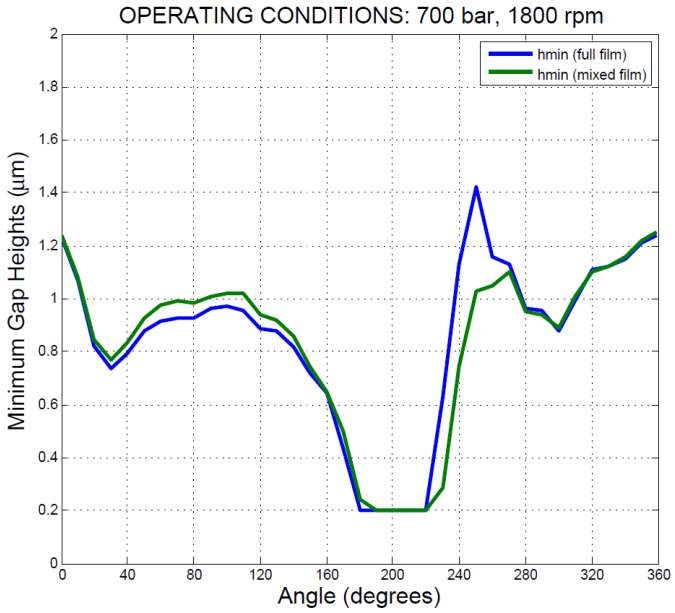

Figure 64: Difference in trends observed between full film and mixed lubrication models for the variation of the minimum gap height over one shaft revolution for Pump outlet pressure: 700 bar, Shaft speed: 1800 rpm.

The influence of surface roughness on the contact loads generated can also be observed using this model. The model has the flexibility to analyze Gaussian distributions of the surface roughness where the magnitude of the standard deviation roughness parameter R_q can be varied, depending on the finishing ability of the manufacturing process employed to obtain the pistons and cylinders. The variation of the contact load generated over the shaft angle is shown in Figure 65 for varying surface roughness values.

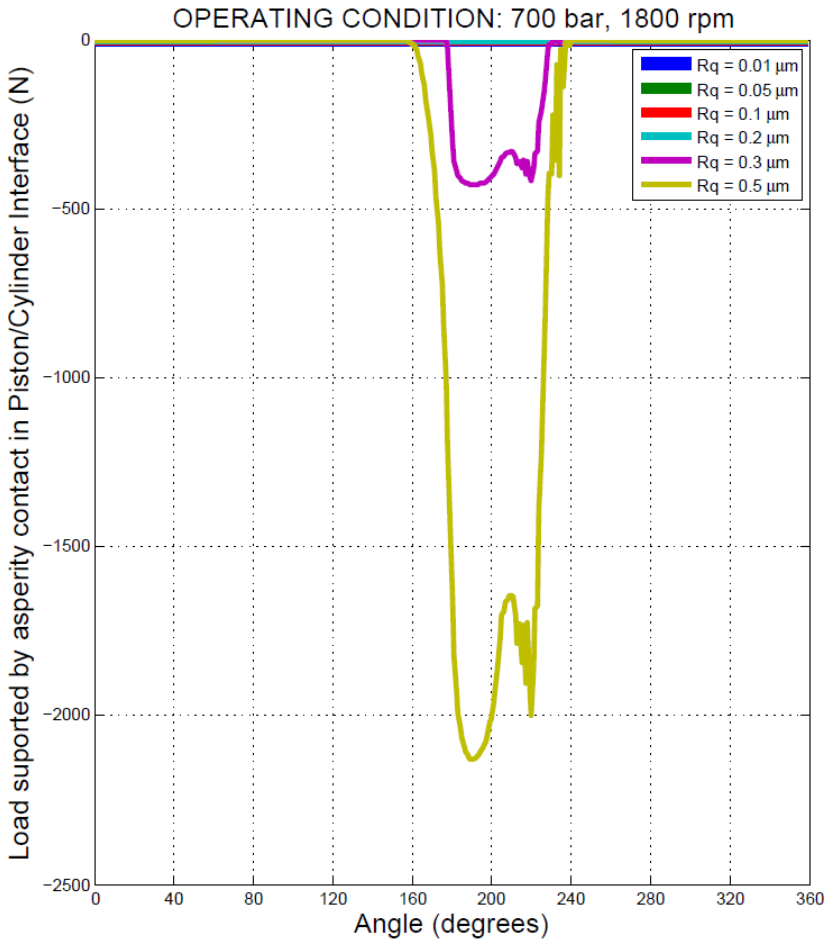

Figure 65: Load supported by asperities over a single pumping cycle as the surface roughness parameter is varied for Pump outlet pressure: 700 bar, Shaft speed: 1800 rpm.

It can be observed that as the surfaces become smoother ($R_q \leq 0.2\ \mu m$), the more stable the fluid film. There is no effect of surface roughness observed until R_q reaches 0.3 μm. As the asperities get larger, the interactions between the asperities increases, leading to larger values of loads supported by the asperities, instead of just the fluid. Therefore, it may be concluded that a smoother surface finish will aid in the balance of the piston, thus leading to full film lubrication in the piston/cylinder interface.

However, for the purposes of this study a surface finish of $R_q = 0.5\ \mu m$ is chosen, as this is the most commonly observed level of finish in most lubricated machinery. A similar

surface finish is observed and simulated in studies on journal bearings (also conformal contacts) [34, 35].

In order to study the effect on the pump performance, the following surface parameters shown in Table 6 were used for the mixed FSI-EHD model.

Table 6: Surface features and parameters used in the simulations performed.

Surface Parameter	**Description**	**Value [unit]**
C	Piston/Cylinder Clearance	8 μm
R_q	Standard Deviation of the combined surface roughness	0.5 μm
R_{q1}	Average piston asperity height	0.03 μm
R_{q2}	Average cylinder asperity height	0.03 μm
Material	Piston and Cylinder materials	Steel
E_Y	Young's modulus of piston and cylinder	210 GPa
ν_1	Poisson's ratio of piston material	0.3 (-)
ν_1	Poisson's ratio of cylinder material	0.3 (-)

6.2 Prediction of Piston Balance

Figure 66 shows the variation in load support due to asperity contact under two operating conditions: Pump outlet pressure of 700 bar and 2500 bar with the shaft speed at 1800 rpm. This was done for the case of pistons without any grooves.

It can be observed that the balance appears to worsen when the pressures are higher – at the 2500 bar operating condition, the piston appears to tilt more, thus leading to contact in the interval between $320^o - 20^o$, which is about an interval of 60^o of the shaft's revolution. Thus, there appears to be mixed lubrication for an extended period of the pumping cycle as compared to operating conditions which are relatively less harsh.

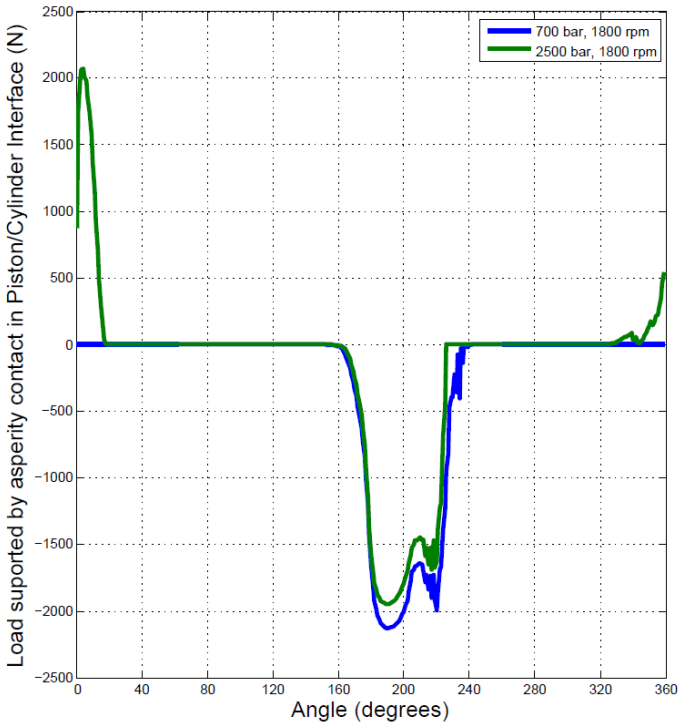

Figure 66: Variation of load supported by asperity contact in the piston/cylinder interface for two operating conditions: Pump outlet pressures: 700 bar and 2500 bar, Shaft speed: 1800 rpm.

In order to assess the effect of the positioning of a circumferential groove on piston balance, the four geometries namely 'No Groove', Positions 'A', 'Position B' and Position 'C' are compared in Figures 67 and 68 for the two operating conditions mentioned.

The trend observed in the contact loads appear to suggest that the pump incorporating pistons with grooves closer to the displacement chamber end (Position 'A') have the least amount of load being supported by asperities and thus, show the better hydrodynamic balance. As the grooves are moved away from the displacement chamber end, the balance starts to worsen.

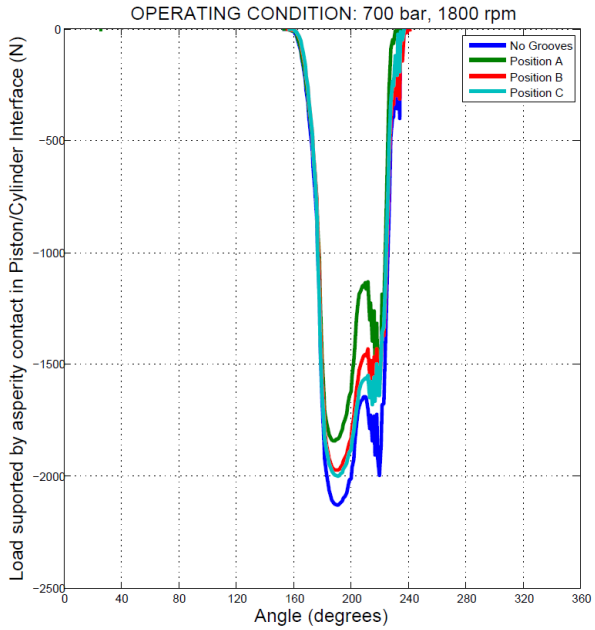

Figure 67: Effect of piston groove position on the load supported by asperity contact in the piston/cylinder interface for Pump outlet pressure: 700 bar, Shaft speed: 1800 rpm.

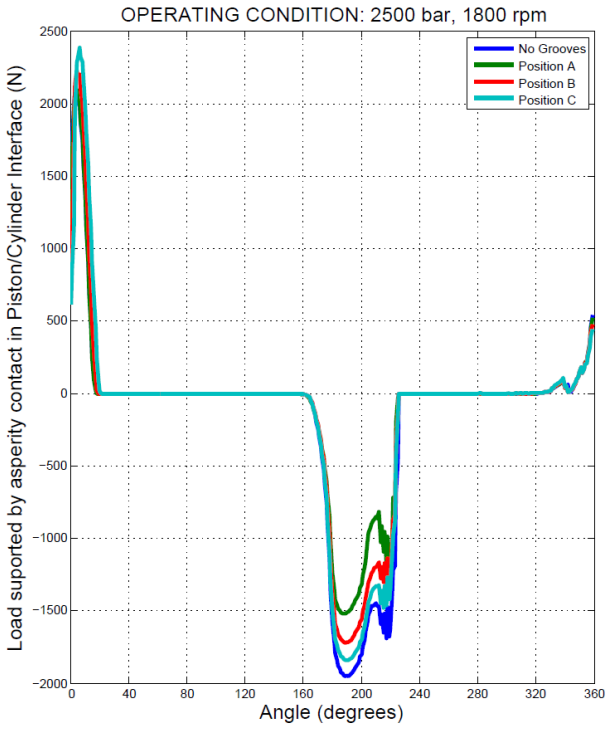

Figure 68: Effect of piston groove position on the load supported by asperity contact in the piston/cylinder interface for Pump outlet pressure: 2500 bar, Shaft speed: 1800 rpm.

6.3 Prediction of Pump Performance

Tables 7 and 8 show the estimated performance parameters for the two operating conditions with the 4 different piston configurations discussed. It may be seen that the trend is similar to what was observed with the full film lubrication assumption, i.e. the losses due to leakages appear to increase as the groove is positioned farther away from the displacement chamber end of the piston, while the viscous power losses remain similar in magnitude to each other.

Table 7: Performance parameters observed per revolution of the shaft under steady state conditions at Pump outlet pressure: 700 bar, Shaft speed: 1800 rpm under mixed lubrication.

Piston Configuration	**Power loss due to Leakage [% of total losses]**	**Power loss due to Viscous friction [% of total losses]**	**Volumetric Efficiency [%]**
No Grooves	8.72	0.32	91.98
Position A	8.74	0.33	91.96
Position B	8.75	0.33	91.96
Position C	8.78	0.32	91.93

Table 8: Performance parameters observed per revolution of the shaft under steady state conditions at Pump outlet pressure: 2500 bar, Shaft speed: 1800 rpm under mixed lubrication.

Piston Configuration	**Power loss due to Leakage [% of total losses]**	**Power loss due to Viscous friction [% of total losses]**	**Volumetric Efficiency [%]**
No Grooves	14.11	0.36	87.64
Position A	14.25	0.36	87.53
Position B	14.28	0.36	87.51
Position C	14.31	0.36	87.49

Figures 69 – 71 show the effect of incorporating mixed lubrication as compared to a full film assumption on the performance parameters estimated for the all the single groove position geometries compared against pistons with no grooves.

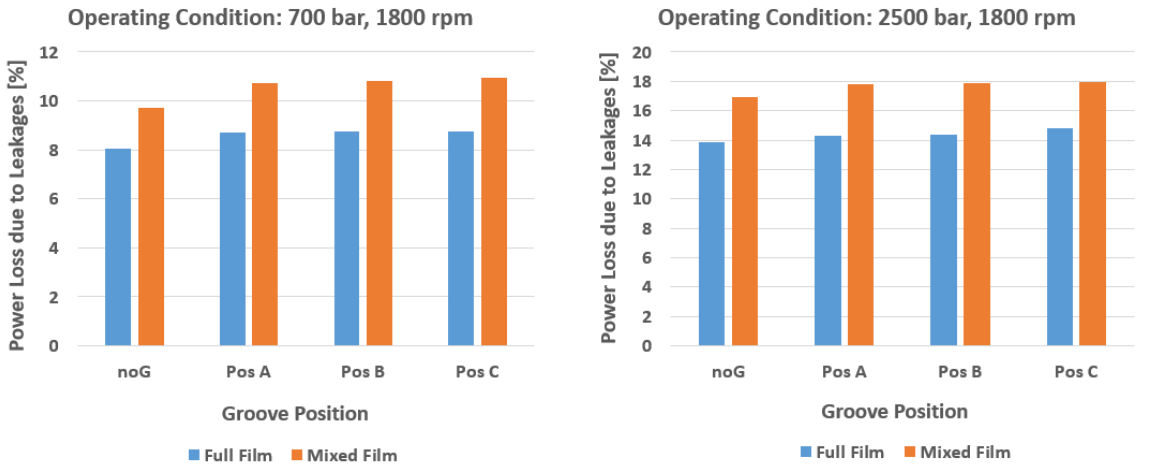

Figure 69: Comparison between Percentage Power Loss due to Leakages between all four piston geometries using full film and mixed lubrication models for (left) Pump outlet pressure: 700 bar, Shaft speed: 1800 rpm and (right) Pump outlet pressure: 700 bar, Shaft speed: 1800 rpm.

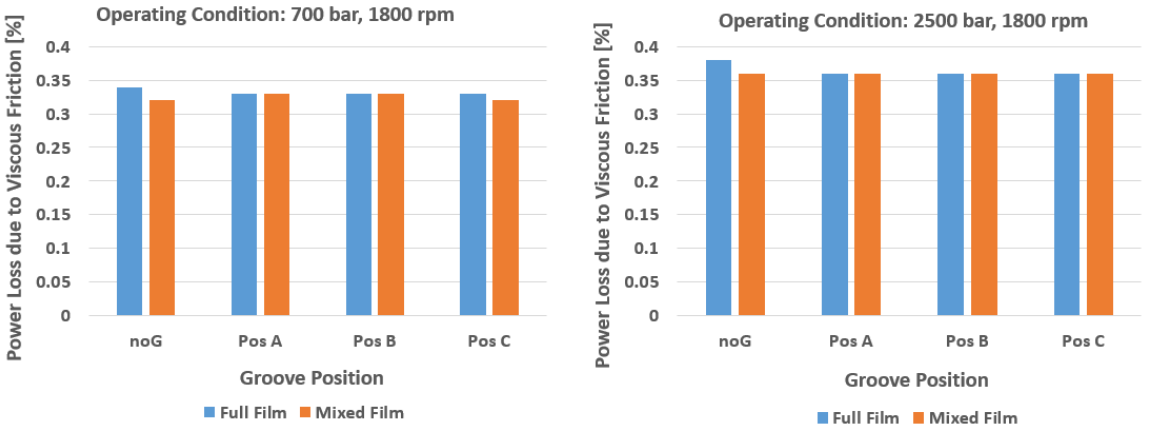

Figure 70: Comparison between Percentage Power Loss due to Viscous Friction between all four piston geometries using full film and mixed lubrication models for (left) Pump outlet pressure: 700 bar, Shaft speed: 1800 rpm and (right) Pump outlet pressure: 700 bar, Shaft speed: 1800 rpm.

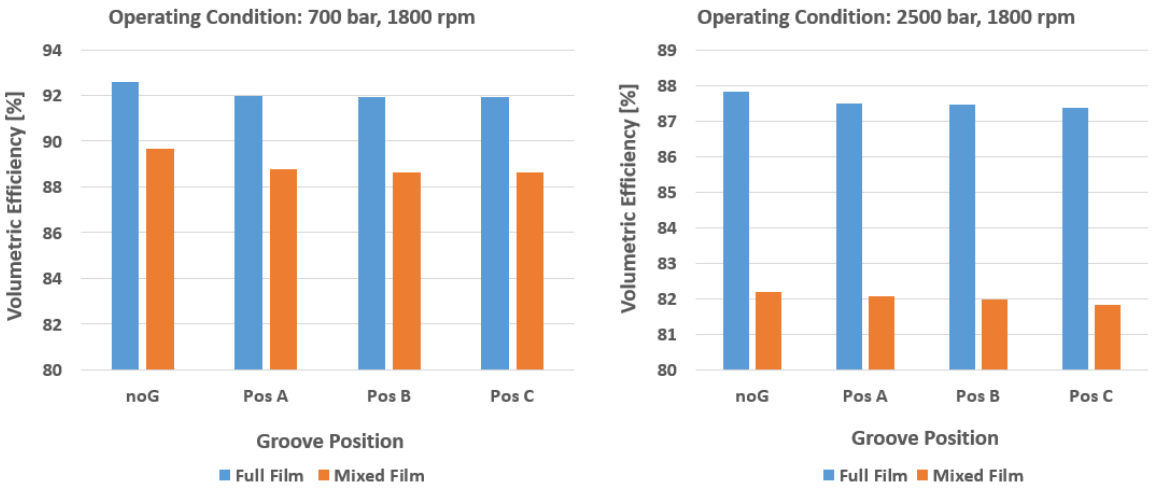

Figure 71: Comparison between Volumetric Efficiencies between all four piston geometries using full film and mixed lubrication models for (left) Pump outlet pressure: 700 bar, Shaft speed: 1800 rpm and (right) Pump outlet pressure: 700 bar, Shaft speed: 1800 rpm.

It can be clearly seen that the leakages have been underestimated in the full film model for all the geometries for both extreme operating conditions as compared to the mixed lubrication model. The power losses due to leakages have been overestimated by $2 - 4$ %. As a consequence, the mixed lubrication model also reports between $2 - 6$ % reductions in volumetric efficiencies.

However, the viscous friction losses have been predicted to be very close to those evaluated from the full film model. A better evaluation of the viscous friction losses can perhaps be found if the effects of thermal deformation of the surfaces and asperities due to viscous heating and heat transfer were taken into account. This could be a possible area of improvement for the current model in the future.

CHAPTER 7. SUMMARY AND CONCLUSIONS

This study presented two novel approaches to modeling the lubricating interfaces of ultra-high pressure radial piston machines: a Mixed Fluid Structure Interaction – Elastohydrodynamic model of the Piston/Cylinder interface and a combination of experimental and simulation based approaches to quantify the kinematics and friction at the Cam/Piston interface. These two lubricating interfaces are the primary sources of power losses in radial piston machines. The prediction of these power losses was done by developing separate modules for the modeling of each interface, while ensuring a close interaction with each other through the exchange of information between the two modules. A global fluid dynamic model developed in the past to characterize the flow through the radial piston machine was used to provide the pressure boundary conditions across the Piston/Cylinder lubricating gap in order to capture the flow variations within this gap. On the basis of a force balance of the piston, its micro-motion can be estimated, as a consequence of which there is a hydrodynamic effect created in the gap. An isothermal analysis of the fluid film was coupled with the evaluation of the elastic deformations of the solid bodies – the piston and the cylinder. This allows the fluid in the lubricating interface to support the loads generated by the piston, thus making an assumption of full film lubrication within the interface.

In the evaluation of the force balance of the piston, it was observed that the two forces influencing the overall micro-motion of the pistons were the friction forces from the eccentric cam and the moment caused due to the reaction force from the cam on to the pistons. Thus, it was deemed crucial that an accurate evaluation of the variation of the friction force must be provided as input to the Piston/Cylinder gap model in order to obtain a closer prediction of the pistons' micro-motions. For this reason, a numerical model to estimate the viscous friction at the Cam/Piston interface was created,

incorporating the effects of elastohydrodynamic lubrication and Non-Newtonian fluid behavior due to large sliding velocities occurring between the surfaces of the cam and each piston. However, due to the presence of rolling element bearings in between the eccentric cam and a free-to-rotate outer race whose behavior is influenced by the dynamics of the four pistons, the evaluation of the friction variation between the cam and each piston over a pumping cycle becomes more challenging. In order to provide accurate inputs of the kinematics of the outer race to the friction model, an experimental setup was created by which the instantaneous angular velocity of the outer race could be found through the use of a video camera. This method allowed for a more accurate evaluation of the friction coefficient as a function of shaft angle, thus enabling a more accurate prediction of the power losses due to leakages and viscous friction at the piston/cylinder interface. The development of the friction model also led to the prediction of the viscous power losses present at the cam/piston interface. Due to high sliding velocities being present, these losses were found to be larger than those evaluated at the piston/cylinder interface.

The evaluation of the friction coefficient at the cam/piston interface led to the possibility of exploring new design features that could potentially lead to a better lubricating performance for the machine. Circumferential piston grooves were modeled using a control volume approach wherein the variation of pressure within the groove is considered to be negligible. The effects of the groove on the piston tilt and overall balance, as well as on the performance parameters were evaluated. It was found that in all the cases and operating conditions examined, a correctional force called the contact force was required to stabilize the piston, thus ensuring numerical stability to the algorithm. This called for a novel strategy to evaluate the effects of surface roughness and asperity contact load sharing on the lubricating performance of the machine in question.

A Mixed Fluid Structure Interaction based EHD model was developed in order to account for the presence of asperities and the impact of surface roughness consideration on the fluid flow. This model took into account the physical effects of roughness orientation (with a Gaussian orientation of asperities being modeled), flow through a rough lubricating interface, elastic-plastic deformations of the asperities due to contact, and load

sharing between the fluid and the contact surfaces of the asperities at low film thicknesses. This enabled a more physics-based prediction of the piston balance and lubricating performance, and now, the effect of the grooves could be analyzed in a more accurate manner. It was observed that positioning a single groove close to the displacement chamber end of the piston provided the best piston balance in terms of the least asperity contact predicted. Also, the mixed lubrication model displayed a marked difference in the prediction of the performance parameters of the pump, by showing that the full film model underestimated the leakages occurring at the piston/cylinder interface. The various new features that could be evaluated due to the development of this mixed lubrication model were also highlighted.

The results from this research showed that the numerical modeling of radial piston machines could enable the virtual prototyping of such machines, thus saving a lot of time, money and infrastructure in terms of manual prototyping and testing. As a part of the further development of this model, thermal effects in both the lubricating gaps can be incorporated in studying the gap flow. Also, a mixed lubrication model for the cam/piston interface, along with the incorporation of squeeze effects could lead to even better predictions of the piston micro-motion. Finally, an optimization procedure could be developed to aid in finding the most efficient and durable grooved pistons designs for various applications of radial piston machines.

LIST OF REFERENCES

LIST OF REFERENCES

1. Chapple, P. J. (1992). Modelling of a radial-piston hydraulic motor. Proceedings of the Institution of Mechanical Engineers, Part I: Journal of Systems and Control Engineering, 206(3), 171-180.

2. Ivantysyn, J., & Ivantysynova, M. (2001). Hydrostatic pumps and motors. New Delhi: Academic Books International.

3. Kleist, A. (1997). Design of Hydrostatic Static Bearing and Sealing Gaps in Hydraulic Machines. In 5th Scandinavian International Conference on Fluid Power, Linköping, Sweden, May (pp. 28-30).

4. Kleist, A. (1995). Berechnung von hydrostatischen Dichtstellen in hydraulischen Maschinen. Olhydraulik und Pneumatik, 39(10), 767.

5. Mortensen, K. A., & Henriksen, K. H. (2011). Efficiency Analysis of a Radial Piston Pump Applied in a 5MW Wind Turbine with Hydraulic Transmission. Master Thesis, Aalborg University, Aalborg, Denmark.

6. Agarwal, P. (2014). Modeling of High Pressure Radial Piston Pumps. Master Thesis, Purdue University, Indiana, USA.

7. Fang, Y., & Shirakashi, M. (1995). Mixed Lubrication Characteristics between the Piston and Cylinder in Hydraulic Piston Pump-Motor. Trans. ASME, Journal of Tribology, 117.

8. Olems, L. (2000). Investigations of the temperature behaviour of the piston cylinder assembly in axial piston pumps. International Journal of Fluid Power, 1(1), 27-39.

9. Wieczorek, U., & Ivantysynova, M. (2002). Computer aided optimization of bearing and sealing gaps in hydrostatic machines—the simulation tool CASPAR. International Journal of Fluid Power, 3(1), 7-20.

10. Dhar, S. (2014). A Study of Fluid Structure and Thermal Interactions in the Lubricating Interface Between Gears and Lateral Bushes in External Gear Machines, Ph.D. Thesis, Purdue University, Indiana, USA.

11. Pelosi, M., & Ivantysynova, M. (2010). A fully coupled thermo-elastic model for the rotating kit of axial piston machines. In ASME/Bath Symposium on Fluid Power and Motion Control, Bath, UK, Sept (pp. 15-17).

12. Pelosi, M., & Ivantysynova, M. (2011). Surface Deformations Enable High Pressure Operation of Axial Piston Pumps. In ASME 2011 Dynamic Systems and Control Conference and Bath/ASME Symposium on Fluid Power and Motion Control (pp. 193-200). American Society of Mechanical Engineers.

13. Pelosi, M., & Ivantysynova, M. (2013). The Impact of Axial Piston Machines Mechanical Parts Constraint Conditions on the Thermo-Elastohydrodynamic Lubrication Analysis of the Fluid Film Interfaces. International Journal of Fluid Power, 14(3), 35-51.

14. Pelosi, M., & Ivantysynova, M. (2012). A geometric multigrid solver for the piston–cylinder interface of axial piston machines. Tribology Transactions, 55(2), 163-174.

15. Huang, C., & Ivantysynova, M. (2006). An advanced gap flow model considering piston micro motion and elastohydrodynamic effect. FPNI Ph.D. Symposium on Fluid Power.

16. Pelosi, M. (2012). An Investigation on the Fluid-Structure Interaction of Piston/Cylinder Interface, Ph.D. Thesis, Purdue University, Indiana, USA.

17. Schenk, A., & Ivantysynova, M. (2012). The influence of swashplate elastohydrodynamic deformation in the slipper-swashplate interface. FPNI Ph.D. Symposium on Fluid Power.

18. Schenk, A., Zecchi, M., & Ivantysynova, M. (2013). Accurate Prediction of Axial Piston Machine's Performance through a Thermo-Elastohydrodynamic Simulation Model. ASME/Bath Symposium on Fluid Power and Motion Control. Sarasota, FL.

19. Zecchi, M. (2013). A Novel Fluid Structure Interaction and Thermal Model to Predict the Cylinder Block/Valve Plate Interface Performance in Swash Plate Type Axial Piston Machines, Ph.D. Thesis, Purdue University, Indiana, USA.

20. Zecchi, M., & Ivantysynova, M. (2012). An investigation of the impact of micro surface shaping on the cylinder block/valve plate interface performance through a novel thermal-elastohydrodynamic model, FPNI Ph.D. Symposium on Fluid Power.

21. Zecchi, M., & Ivantysynova, M. (2012). Cylinder Block/Valve Plate Interface – A Novel Approach to Predict Thermal Surface Loads. International Fluid Power Conference (IFK).

22. Dhar S., & Vacca A. (2013). A Fluid Structure Interaction-EHD Model of the Lubricating Gaps in External Gear Machines: Formulation and Validation. Tribology International 62:78-90.

23. Wang, Q. J., Shi, F., & Lee, S. C. (1997). A mixed-lubrication study of journal bearing conformal contacts. Journal of Tribology, 119(3), 456-461.

24. Oh, K. P., & Goenka, P. K. (1985). The elastohydrodynamic solution of journal bearings under dynamic loading. Journal of Tribology, 107(3), 389-394.

25. Xiong, S., Lin, C., Wang, Y., Liu, W. K., & Wang, Q. J. (2010). An efficient elastic displacement analysis procedure for simulating transient conformal-contact elastohydrodynamic lubrication systems. Journal of Tribology, 132(2), 021502.

26. Stefani, F. A., & Rebora, A. U. (2002). Finite element analysis of dynamically loaded journal bearings: influence of the bolt preload. Journal of Tribology, 124(3), 486-493.

27. Piffeteau, S., Souchet, D., & Bonneau, D. (2000). Influence of thermal and elastic deformations on connecting-rod big end bearing lubrication under dynamic loading. Journal of Tribology, 122(1), 181-191.

28. Wu, S., & Cheng, H. S. (1991). A friction model of partial-EHL contacts and its application to power loss in spur gears. Tribology Transactions, 34(3), 398-407.

29. Patir, N., & Cheng, H. S. (1978). An Average Flow Model for Determine Effects of Three Dimensional Roughness on Partial Hydrodynamic Lubrication, ASME Journal of Lubrication Technology, Vol. 100, pp. 12-17.

30. Lee, S. C., & Ren, N. (1996). Behavior of Elastic-Plastic Rough Surface Contacts as Affected by the Surface Topography, Load and Materials, STLE Tribology Transactions, Vol. 39, pp. 67-74.

31. Meng, F, Wang, Q. J., Hua, D., & Liu, S. (2010). A Simple Method to Calculate Contact Factor Used in Average Flow Model, ASME Journal of Tribology, Vol. 132, pp. 024505-1 – 024505-4.

32. Chengwei, W., & Linqing, Z. (1989). An Average Reynolds Equation for Partial Film Lubrication with a Contact Factor, ASME Journal of Tribology, Vol. 111, pp. 188-191.

33. Harp, S. R., & Salant, R. F. (2000). An average flow model of rough surface lubrication with inter-asperity cavitation, ASME Journal of Tribology 123, pp. 134–143.

34. Shi, F., & Wang, Q. (1998). A Mixed-TEHD Study for Journal-Bearing Conformal Contacts, Part I: Model Formulation and Approximation of Heat Transfer Considering Asperity Contacts, ASME Journal of Tribology 120, pp. 198-205.

35. Wang, Q. J., Shi, F., & Lee, S. C. (1997). A Mixed-TEHD Study for Journal-Bearing Conformal Contacts – Part II: Contact, Film Thickness, and Performance Analyses, Journal of Tribology, pp. 206-213.

36. de Kraker, A., van Ostayen, R. A. J., & Rixen, D. J. (2007). Calculation of Stribeck curves for (water) lubricated journal bearings, Tribology International 40(3), pp. 459-469.

37. Yamaguchi, A., & Matsuoka, H. (1992). A mixed lubrication model applicable to bearing/seal parts of hydraulic equipment, Journal of tribology, 114(1), 116-121.

38. Kazama, T., & Yamaguchi, A. (1993). Application of a mixed lubrication model for hydrostatic thrust bearings of hydraulic equipment. Journal of Tribology 115(4), 686-691.

39. Kazama, T. (2005). Numerical simulation of a slipper model for water hydraulic pumps/motors in mixed lubrication. In Proceedings of the JFPS International Symposium on Fluid Power, Vol. 6, pp. 509-514.

40. Wegner, S., Loschner, F., Gels, S., & Murrenhoff, H. (2016) Validation of the physical effect implementation in a simulation model for the cylinder block/valve plate contact supported by experimental investigations, Proceedings of the 10th International Fluid Power Conference, pp. 269-282.

41. Lasaar, R. (2003). Eine Untersuchung zur mikro- und makrogeometrischen Gestaltung der Kolben-/Zylinderbaugruppe von Schraegscheibenmaschinen, VDI Verlag GmbH, Duesseldorf.

42. Hargreaves, D. J. (1991). Surface waviness effects on the load-carrying capacity of rectangular slider bearings, Wear 145, pp. 137-151.

43. Ivantysynova, M., Garret, R. A., & Frederickson, A. A. (2012). Positive displacement machine piston with wavy surface form, US 20120079936 A1.

44. Park, T. (2008). Lubrication analysis between piston and cylinder in high pressure piston pump considering circumferential grooves and viscosity variation with pressure, Proceedings of the 9th Biennial ASME Conference on Engineering Systems Design and Analysis, Haifa, Israel.

45. Berthold, H. (1999). Axial piston machine having a cooling circuit for the cylinders and pistons, US 5971717 A.

46. Majumdar, B. C., Pai, R., & Hargreaves, D. (2004). Analysis of water- lubricated journal bearings with multiple axial grooves, Available from: <http://pij.sagepub.com/content/218/2/135.full.pdf>. [25 April 2015].

47. Basu, P. (1992). Analysis of a radial groove gas face seal. STLE Tribology Transactions 35(1):11–20.

48. Razzaque, M. M., & Kato, T. (1999). Effects of groove orientation on hydrodynamic behavior of wet clutch coolant films, Transactions of ASME 121:6–61.

49. Kumar, S., Bergada, J. M., & Watton, J. (2009). Axial piston pump grooved slipper analysis by CFD simulation of three dimensional NVS equation in cylindrical coordinates, Computational Fluids 38:648–63.

50. Kumar, S., & Bergada, J. M. (2009). The effect of piston grooves performance in an axial piston pumps via CFD analysis, International Journal of Mechanical Sciences 66:168-179.

51. Agarwal, P., Vacca, A., Kim K., and Kim, T. (2014) A numerical model for the simulation of flow in radial piston machines, Proceedings of the International Exposition for Fluid Power, Las Vegas, USA.

52. Agarwal, P., Vacca, A., Wang, K., Kim, K. et al. (2014). An Analysis of Lubricating Gap Flow in Radial Piston Machines, SAE International Journal of Commercial Vehicles 7(2): 524 – 534.

53. Vacca, A., & Guidetti, M. (2011). Modelling and experimental validation of external spur gear machines for fluid power applications. Simulation Modelling Practice and Theory, 19(9), 2007-2031.

54. OpenFOAM: The Open Source CFD toolbox. Available at: www.openfoam.com. Accessed July 7, 2016.

55. GNU Scientific Library. Available at: http://www.gnu.org/software/gsl/. Accessed July 7, 2016.

56. ANSYS, Inc. Available at: http://www.ansys.com/. Accessed July 7, 2016.

57. Reynolds, O. (1886). On the Theory of Lubrication and Its Application to Mr. Beauchamp Tower's Experiments, Including an Experimental Determination of the Viscosity of Olive Oil. Proceedings of the Royal Society of London, 40(242-245), 191-203.

58. Jasak, H., & Weller, H. G. (2000). Application of the finite volume method and unstructured meshes to linear elasticity. International journal for numerical methods in engineering, 48(2), 267-287.

59. Booser, E. R. (1983) CRC handbook of lubrication (theory and practice of tribology) – Volume 1. Application and maintenance, CRC Press.

60. Hamrock, B. J., Schmid, S. R., and Jacobson, B. O. (2004). Fundamentals of fluid film lubrication, 2 ed. CRC press.

61. Dowson, D., and Higginson, G. R. (1966). Elasto-hydrodynamic lubrication: the fundamentals of roller and gear lubrication, 2 ed., Oxford: Pergamon Press.

62. Barus, C. (1893). Isothermals, isopiestics and isometrics relative to viscosity, American Journal of Science 266: 87 - 96.

63. Jacobson, B. O., and Hamrock, B. J. (1984). Non-Newtonian fluid model incorporated into elastohydrodynamic lubrication of rectangular contacts. Journal of Tribology 106(2): 275 - 282.

64. Wang, J., Venner, C. H., and Lubrecht, A. A. (2013). Influence of Surface Waviness on the Thermal Elastohydrodynamic Lubrication of an Eccentric-Tappet Pair. Journal of Tribology 135(2): 021101-1 - 021101-12.

65. Patir, N., & Cheng, H. S. (1979). Application of Average Flow Model to Lubrication Between Rough Surfaces, ASME Journal of Lubrication Technology, Vol. 101, pp. 220-229.

APPENDICES

Appendix A. Derivation of the Modified Form of the Average Flow Reynolds Equation

In this section, a derivation of the Average Flow Reynolds Equation used to model the flow in the piston/cylinder lubricating interface is presented (Equation (3.24)). This derivation will be performed with respect to Figure 72. The clearances represented between the top and bottom surfaces (displayed in dotted lines) is representative of the piston/cylinder lubricating gap. In order to include the effects of surface deformations for both the piston and cylinder, a reference plane (represented in blue) at an arbitrary orientation within the lubricating gap is considered in order to represent $z = 0$. This leads to the following definition of the gap height:

$$h = h_t - h_b \tag{A.1}$$

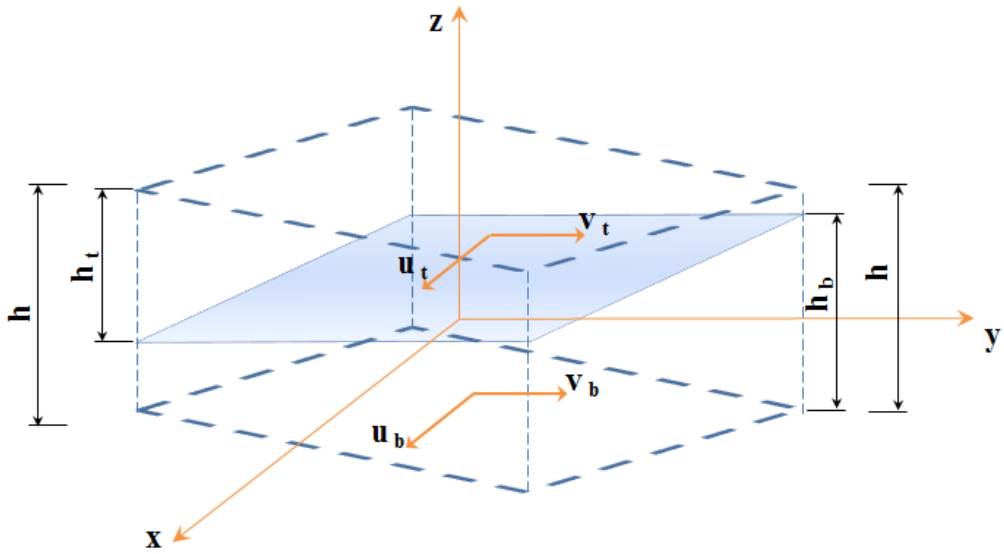

Figure 72: Parameters defining the gap height in the piston/cylinder interface with respect to each surface. Top and bottom surfaces are represented using dotted lines and the reference plane is represented in blue.

From [6, 52], it is seen that certain assumptions can be made to simplify the Navier-Stokes equations to obtain appropriate relations for the velocity vector represented in the Reynolds equation for flow in the piston/cylinder gap. These assumptions are not detailed

here for the sake of brevity, but are well-known in literature and can be found in [6] as applied to the piston/cylinder gap of radial piston machines.

By applying the afore-mentioned assumptions, the Navier-Stokes equations can be simplified to obtain the formulations for the velocity parameter shown as follows:

$$u = \frac{1}{2\mu}\frac{\partial p}{\partial x}(z^2 - z(h_t + h_b) + h_t h_b) - \frac{z u_g}{h_t - h_b} + \frac{h_t u_g}{h_t - h_b}, \tag{A.2}$$

$$v = \frac{1}{2\mu}\frac{\partial p}{\partial y}(z^2 - z(h_t + h_b) + h_t h_b) - \frac{z v_g}{h_t - h_b} + \frac{h_t v_g}{h_t - h_b}. \tag{A.3}$$

Now, consider the continuity equation which – along with the Navier-Stokes equation – defines the behavior of fluid flow:

$$\frac{\partial \rho}{\partial t} + \nabla.(\rho \mathbf{v}) = 0. \tag{A.4}$$

Assuming steady state conditions (to evaluate pump flow features at steady state):

$$\nabla.(\rho \mathbf{v}) = 0. \tag{A.5}$$

By integrating this continuity equation over the lubricating gap heights, the following equation is obtained:

$$\int_{h_b}^{h_t} \frac{\partial}{\partial x}\rho u \, dz + \int_{h_b}^{h_t} \frac{\partial}{\partial y}\rho v \, dz + \int_{h_b}^{h_t} \frac{\partial}{\partial z}\rho w \, dz = 0. \tag{A.6}$$

First, the integration of the first term in this equation is considered. By splitting this into two terms, from the reference plate to the top surface and from the reference plane to the bottom surface:

$$\int_{h_b}^{h_t} \frac{\partial}{\partial x}\rho u \, dz = \int_{h_b}^{0} \frac{\partial}{\partial x}\rho u \, dz + \int_{0}^{h_t} \frac{\partial}{\partial x}\rho u \, dz = -\int_{0}^{h_b} \frac{\partial}{\partial x}\rho u \, dz + \int_{0}^{h_t} \frac{\partial}{\partial x}\rho u \, dz. \tag{A.7}$$

Since u and v are functions of all three coordinates, Leibnitz's rule of integration can be applied as follows:

$$\int_0^h \frac{\partial}{\partial x} f(x,y,z) dz = -f(x,y,h)\frac{\partial h}{\partial x} + \frac{\partial}{\partial x}\int_0^h f(x,y,z) dz. \tag{A.8}$$

Using this relation, the first term in Equation (A.7) can be expanded as follows:

$$-\left(-\rho \phi_c u_b \frac{\partial h_b}{\partial x} + \frac{\partial}{\partial x}\rho \int_0^{h_b} u \, dz\right) + \left(-\rho \phi_c u_t \frac{\partial h_t}{\partial x} + \frac{\partial}{\partial x}\rho \int_0^{h_t} u \, dz\right) = 0. \tag{A.9}$$

A contact factor ϕ_c is defined so that the average gap height in a rough interface can be evaluated. The density ρ is assumed to be constant across the gap height (z), but can still vary in the x and y dimensions. Grouping terms, Equation (A.7) can be written as:

$$\rho u_b \frac{\partial h_b}{\partial x} - \rho u_t \frac{\partial h_b}{\partial x} + \frac{\partial}{\partial x}\rho \int_{h_b}^{h_t} u \, dz = 0. \tag{A.10}$$

For $\int_{h_b}^{h_t} \frac{\partial}{\partial x}\rho v \, dz$, a similar approach is applicable leading to:

$$\rho \phi_c v_b \frac{\partial h_b}{\partial y} - \rho \phi_c v_t \frac{\partial h_b}{\partial y} + \frac{\partial}{\partial y}\rho \int_{h_b}^{h_t} v \, dz = 0. \tag{A.11}$$

For the third term, the integration can be performed more directly. The top can the bottom surface can also exhibit normal squeeze micro-motion, which means that they can have velocities also in the z direction.

$$\int_{h_b}^{h_t} \frac{\partial}{\partial z}\rho w \, dz = \rho \phi_c (w_t - w_b). \tag{A.12}$$

Squeeze velocities are essentially the rate at which the gap height h is changing. Representing $w_t = \frac{\partial h_t}{\partial t}$ and $w_b = \frac{\partial h_b}{\partial t}$, we get:

$$\rho(w_t - w_b) = \rho \phi_c (\frac{\partial h_t}{\partial t} - \frac{\partial h_b}{\partial t}). \tag{A.13}$$

So, Equation (A.10) can finally can be written as:

$$\rho u_b \frac{\partial h_b}{\partial x} + \rho v_b \frac{\partial h_b}{\partial y} - \rho u_t \frac{\partial h_b}{\partial x} - \rho v_t \frac{\partial h_b}{\partial y} + \rho \left(\frac{\partial h_t}{\partial t} - \frac{\partial h_b}{\partial t}\right) + \frac{\partial}{\partial x}\rho \int_{h_b}^{h_t} u \, dz +$$
$$\frac{\partial}{\partial y}\rho \int_{h_b}^{h_t} v \, dz = 0. \tag{A.14}$$

To complete the derivation of the Reynolds equation, the expressions for the velocity field shown in Equations (A.2) and (A.3) are to be substituted in the integral terms. Here, we define pressure flow factors ϕ_x, ϕ_y as the ratio of average pressure flow in a rough interface as compared to that of a smooth bearing, and also defining a shear flow factor ϕ_s.

Performing the integrations and regrouping the terms, we get:

$$\frac{\partial}{\partial x}\rho\int_{h_b}^{h_t} u\,dz + \frac{\partial}{\partial y}\rho\int_{h_b}^{h_t} v\,dz = -\frac{\partial}{\partial x}\left(\frac{\rho\phi_x(h_t-h_b)^3}{12\mu}\frac{dp}{dx}\right) - \frac{\partial}{\partial y}\left(\frac{\rho\phi_y(h_t-h_b)^3}{12\mu}\frac{dp}{dy}\right) + \rho\phi_c(h_t-h_b)\frac{\partial}{\partial x}\left(\frac{u_t+u_b}{2}\right) + \rho\phi_c(h_t-h_b)\frac{\partial}{\partial y}\left(\frac{v_t+v_b}{2}\right) + \rho\phi_c\left(\frac{u_t+u_b}{2}\right)\frac{\partial(h_t-h_b)}{\partial x} + \rho\phi_c\left(\frac{v_t+v_b}{2}\right)\frac{\partial(h_t-h_b)}{\partial y} + R_q\frac{v_b}{2}\frac{\partial\phi_s}{\partial x} \quad (A.15)$$

Using $h = h_t - h_b$, we finally have the most general form of the Average Reynolds equation which can account for features on both top and bottom surfaces by evaluating Equation (A.6):

$$-\frac{\partial}{\partial x}\left(\frac{\rho\phi_x h^3}{12\mu}\frac{dp}{dx}\right) - \frac{\partial}{\partial y}\left(\frac{\rho\phi_y h^3}{12\mu}\frac{dp}{dy}\right) + \rho\phi_c\left(\frac{u_b}{2}\right)\frac{\partial h}{\partial x} + \rho\phi_c\left(\frac{v_b}{2}\right)\frac{\partial h}{\partial y} + \rho\phi_c u_b\frac{\partial h_b}{\partial x} + \rho\phi_c v_b\frac{\partial h_b}{\partial y} + \rho\phi_c\left(\frac{\partial h_t}{\partial t} - \frac{\partial h_b}{\partial t}\right) - R_q\frac{v_b}{2}\frac{\partial\phi_s}{\partial x} = 0. \quad (A.16)$$

Assuming isotropic surfaces, $\phi_x = \phi_y$.

And writing this using differential operator notation, we have the form of the Average Reynolds equation seen in Equation (3.24), used in the present work:

$$\nabla.\left(\phi_x\frac{\rho h^3}{12\eta}\nabla p\right) - \phi_c\left(\frac{\rho\boldsymbol{V}_b}{2}\right).\nabla h - \phi_c\rho\boldsymbol{V}_b.\nabla h_b - \phi_c\rho\frac{\partial h}{\partial t} + R_q\frac{\boldsymbol{V}_b}{2}\frac{\partial\phi_s}{\partial x} = 0 \quad (A.17)$$

Appendix B. Flow Factors used in the Average Flow Reynolds Equation

The flow factors used in the evaluation of the pressure field using the Average Flow Reynolds Equation, and the performance parameters in Section 3.3.2, are given in the Table below. These flow factors are evaluated assuming a Gaussian distribution of the surface asperities on both the piston and the cylinder.

Table 9: Analytical expressions for all the factors used in the Mixed FSI-EHD model.

Factor	**Analytical Expression**	**Values for constants**	**References**
ϕ_x	$1 - Ce^{-rH}, \gamma \leq 1$ $1 + CH^{-r}, \gamma > 1$	$\gamma = 1, C = 0.90,$ $r = 0.56, H > 0.5$	[29]
ϕ_c	$e^{-0.6912+0.782H-0.304H^2+0.0401H^3},$ $0 \leq H < 3$ $1\ , H \geq 3$	-	[32]
ϕ_s	$A_1 H^{\alpha_1} e^{-\alpha_2 H + \alpha_3 H^2}\ , H \leq 5$ $A_2 e^{-0.25H}\ , H > 5$	For $\gamma = 1, A_1 = 1.899,$ $A_2 = 1.126, \alpha_1 =$ $0.98, \alpha_2 = 0.92, \alpha_3 =$ 0.05	[65]
ϕ_{fp}	$1 - De^{-sH}, H > 0.75$	For $\gamma = 1, D =$ $1.40, s = 0.66$	[65]
ϕ_{fs}	$A_3 H^{\alpha_4} e^{-\alpha_5 H + \alpha_6 H^2},$ $0.5 < H < 7$ $0\ , H > 7$	For $\gamma = 1, A_3 = 11.1,$ $\alpha_4 = 2.31, \alpha_5 =$ $2.38, \alpha_6 = 0.11$	[65]

Appendix C. Non-Newtonian Formulation in the Cam/Piston EHL Line Contact Model

The non-Newtonian model which was formulated for use in the cam/piston line EHL model in Section 3.4 is described here. The limiting value of the shear stress acting on both the surfaces in contact (piston and cam) is described in Equation (C.1)

$$\tau_L = \tau_0 + \gamma p \tag{C.1}$$

where, τ_0 represents the shear strength and γ is the limiting shear strength proportionality constant. After non-dimensionalization, it is observed that the value of $\bar{\tau_0}$ usually ranges from 10^{-5} to 10^{-4} while γ can vary from 0.04 and 0.1. For the simulation results shown in this study, $\bar{\tau_0} = 9 \times 10^{-5}$ and $\gamma = 0.07$.

Using such a non-Newtonian model, the fluid velocity can be described in terms of five distinct zones that might exist in the elastohydrodynamic conjunction as illustrated in [63]. In order to incorporate the effects of non-Newtonian fluid behavior in the numerical procedure, the pressure field is first generated by solving the Newtonian form of Reynolds equation. This pressure field is then used to evaluate the shear stresses acting on both surfaces ($\overline{\tau_a}$ and $\bar{\tau_b}$) at each point in the computational domain using:

$$\bar{\tau}_a = \frac{\pi}{4W'}\frac{U_e(SRR)\bar{\eta}}{H} + \frac{W'H}{\pi}\left(\frac{d\bar{P}}{dX}\right) \tag{C.2}$$

$$\bar{\tau}_b = \frac{\pi}{4W'}\frac{U_e(SRR)\bar{\eta}}{H} - \frac{W'H}{\pi}\left(\frac{d\bar{P}}{dX}\right) \tag{C.3}$$

The evaluated shear stresses are compared with conditional criteria shown in Table 1 to identify the corresponding zone for each point in the domain. Henceforth, an appropriate non-Newtonian formulation of Reynolds equation is chosen for the point. Derivation of each of these formulations can be found in [63]. Solving the corresponding equations for respective zones, each point in pressure field is updated to complete one sweep across the mesh.

Further details of this model can be found in [6].

Table 10: Non-Newtonian formulation of the Reynolds equation.

Zone no.	**Shear stress at both surfaces**	**Reynolds equation formulation using non-Newtonian model**
0 (Newtonian)	$\overline{\tau_a}<\overline{\tau_L}, \overline{\tau_b} < \overline{\tau_L}$	(*Newtonian*) Same as Eq. (7)
1 (non-Newtonian)	$\lvert\overline{\tau_a}\rvert>\overline{\tau_L}$, $\lvert\overline{\tau_b}\rvert < \overline{\tau_L}$	$\left(\frac{8W'}{\pi}\right)^2 \frac{d}{dX}\left[\frac{\overline{\rho}}{\overline{\eta}}H^3\frac{d\bar{P}}{dX}\right] = 6U_e\sqrt{\frac{2W'}{\pi}}\left[(1 - SRR)\frac{d(\overline{\rho}H)}{dX} + \frac{4W'}{\pi U_e}\frac{d}{dX}\left[\frac{\overline{\rho}}{\overline{\eta}}\bar{\tau}_L H^2\right]\right]$
2 (non-Newtonian)	$\overline{\tau_a}<\overline{\tau_L}$, $\overline{\tau_b}>\overline{\tau_L}$	$\left(\frac{8W'}{\pi}\right)^2 \frac{d}{dX}\left[\frac{\overline{\rho}}{\overline{\eta}}H^3\frac{d\bar{P}}{dX}\right] = 6U_e\sqrt{\frac{2W'}{\pi}}\left[(1 + SRR)\frac{d(\overline{\rho}H)}{dX} - \frac{4W'}{\pi U_e}\frac{d}{dX}\left[\frac{\overline{\rho}}{\overline{\eta}}\bar{\tau}_L H^2\right]\right]$
3 (non-Newtonian)	$\overline{\tau_a}>\overline{\tau_L}$, $\overline{\tau_b}<-\overline{\tau_L}$	$\frac{d\bar{P}}{dX} = 4\sqrt{\frac{2W'}{\pi}}\frac{\overline{\tau}_L}{H}$
4 (non-Newtonian)	$\overline{\tau_a} < -\overline{\tau_L}, \overline{\tau_b} > \overline{\tau_L}$	$\frac{d\bar{P}}{dX} = -4\sqrt{\frac{2W'}{\pi}}\frac{\overline{\tau}_L}{H}$